University of Southampton

Three-dimensional aspects of flapping foils

by

Andhini Novrita Zurman Nasution
ORCID ID 0000-0003-1924-3507

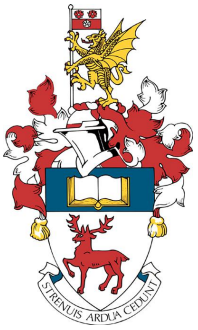

Thesis for the degree of Doctor of Philosophy

Faculty of Engineering and Physical Sciences
School of Engineering
Maritime Engineering Group

January 2021

University of Southampton

Abstract

Faculty of Engineering and Physical Sciences
School of Engineering
Maritime Engineering Group

Thesis for the degree of Doctor of Philosophy

Three-dimensional aspects of flapping foils

by Andhini Novrita Zurman Nasution

Propulsive flapping foils are widely studied in the development of animal-like autonomous systems, energy harvester and other engineering applications. The numerical studies of this topic are mainly two-dimensional (2D) using strip theory for quick and inexpensive results but excluding the three-dimensional (3D) evolution of both onboard and shed vortices. In this work, we are trying to clearly separate the applicability of 2D to 3D studies because of 3D effects. We simulate a NACA0016 foil both in 2D and 3D simulations at a Reynolds number of 5300 with prescribed kinematics based on heave and pitch in 2D motion frame. A general parameter used for flapping foil is the amplitude-based Strouhal number St_A representing the flow dynamics produced by the kinematics. St_A is constructed from two main components i.e. peak-to-peak amplitude $2A$ and frequency f normalised by the inflow U_∞.

Firstly, we study the infinite foil in comparison with 2D (strip) simulation and discovered an intermediate range of St_A where both 2D and 3D simulations are equal and the flow structures are uniform —allowing the strip theory application. The range is $St_A \approx 0.3$ for heaving but wider for pitching and coupled motion, whereas the 3D effects dominate outside of these ranges. The 2D range starts when the flapping motions overpower the 3D vortex shedding of a stationary foil with 10° angle of attack, and it ends with vortex spanwise perturbation because the strength of the shed vortices overwhelms the stabilizing influence of viscous dissipation. Secondly, we study the finite flapping foil where 3D effects dominate the flow but the average peak forces show the possibility to scale from 2D simulation (strip theory). A finite foil experiences 3D kinematics of roll and twist, a linearly increased 2D kinematics of heave and pitch towards the tip, in various $\mathcal{AR}$. The lowest $\mathcal{AR}$ is more affected by the pitch/heave derivative, whereas the highest $\mathcal{AR}$ is less affected thus exhibits similarity to infinite foil. An aspect-ratio correction for flapping foils is developed analogous to Prandtl finite wing theory, enabling future use of strip theory in finite flapping-foil design.

Lastly, we study the importance of the leading-edge sweep angle used by unsteady swimming and flying animals where mixed conclusions are shown in the results of biologists and fluid experimentalists. We provide extensive studies with careful control on variables using 3D simulations of a finite foil undergoing tail-like (pitch-heave) and flipper-like (twist-roll)

kinematics for a range of sweep angles. No significant change is observed in mean force, power, moment and efficiency for tail-like and flipper-like motions as the sweep angle increase. This leads to a conclusion that fish tails, flukes and flippers can have a large range of potential sweep angles without a negative impact on hydrodynamic performance, and a slight adjustment in kinematics to maintain high thrust and efficiency at the same time.

Table of Contents

Table of Tables

Table of Figures

Research Thesis: Declaration of Authorship

Print name: Andhini Novrita Zurman Nasution

Title of thesis: Three-dimensional aspects of flapping foils

I declare that this thesis and the work presented in it are my own and has been generated by me as the result of my own original research.

I confirm that:

1. This work was done wholly or mainly while in candidature for a research degree at this University;
2. Where any part of this thesis has previously been submitted for a degree or any other qualification at this University or any other institution, this has been clearly stated;
3. Where I have consulted the published work of others, this is always clearly attributed;
4. Where I have quoted from the work of others, the source is always given. With the exception of such quotations, this thesis is entirely my own work;
5. I have acknowledged all main sources of help;
6. Where the thesis is based on work done by myself jointly with others, I have made clear exactly what was done by others and what I have contributed myself;
7. Parts of this work have been published and under consideration as the following journal articles.
    - Zurman-Nasution, A. N., Ganapathisubramani, B. & Weymouth, G. D. 2021.*Fin sweep angle does not determine flapping propulsive performance.* J. R. Soc. Interface (in consideration). Preprint https://doi.org/10.1101/2020.11.03.366997.
    - Zurman-Nasution, A. N., Ganapathisubramani, B. & Weymouth, G. D. 2021.*Effects of Aspect Ratio on Rolling and Twisting Foils.* Physical Review Fluids (accepted). Preprint https://arxiv.org/abs/2010.07169.

- Zurman-Nasution, A. N., Ganapathisubramani, B. & Weymouth, G. D. 2020.*Influence of three-dimensionality on propulsive flapping.* Journal of Fluid Mechanics, 886, 1-14. https://doi.org/10.1017/jfm.2019.1078.

Signature:..... Date: January 2021

Acknowledgements

This thesis can be accomplished with a generous 4-year scholarship from Indonesia Endowment Fund for Education (LPDP) to fulfill the requirement of a Ph.D. degree at the University of Southampton. I would like to thank my supervisors Dr Gabriel Weymouth and Professor Bharathram Ganapathisubramani for the supervision, shared knowledge, and valuable guidance in journal writing, conferences and presentation. I also want to thank my friends and colleagues in the University especially in Maritime Engineering and AFM research groups for the support, friendship and a lot of laughs in fun and hard situations. This work can not be accomplished without the support from the Southampton Iridis HPC team and all collaborators and advisors working for publications Dr Kelli Hendrickson (MIT), Professor George Lauder (Harvard) and others. Lastly, I thank my parents and sister in Indonesia for supporting me to pursue the Ph.D.

Nomenclature

SYMBOLS :

A	Amplitude
A_D	Thickness-base amplitude
b, B	Length towards spanwise
C	Chord length
C_D	Drag coefficient
$\overline{C_D}$	Mean thrust coefficient
C_L	Lift Coefficient
$\overline{C_L}$	Mean lift coefficient
C_T	Thrust coefficient
$\overline{C_T}$	Mean thrust coefficient
C_{MZ}	Pitching moment coefficient along Z-Axis
D	Thickness of foil
f	Frequency
$\mathbf{f}$	Forcing
F_x, F_y, F_z	Streamwise, Lateral, Spanwise Force
$\overline{F_x}$	Time-Averaged Streamwise Force
h	Heaving Motion
k	Reduced frequency
l^*	Length extent
L	Length towards streamwise
Pow	Power
Q	Second invariant of the velocity gradient
Re	Reynolds Number
$\mathbf{S}$	rate-of-strain tensor
S_p	Surface Area
St	Strouhal number
St_A	Amplitude-based Strouhal number
St_D	Thickness-based Strouhal number
t	Time unit
U, U_∞	Freestream velocity or inflow
x, y, z	Streamwise, lateral, spanwise direction

α	Angle of attack
Γ	Flow circulation
$\Delta x, \Delta y, \Delta z$	Streamwise, lateral, spanwise grid cell unit
ϵ	Relative error
η	Efficiency
θ	Pitch angle
θ_0	Pitch angle amplitude
Λ	Sweep angle
λ	Eigenvalue of the velocity gradient tensor
ν	Kinematic viscosity
ρ	Density
σ	Standard deviation
ϕ	Phase angle
Ω	Vorticity tensor
ω_z	Streamwise vorticity

ABBREVIATIONS :

$\mathit{Æ}$	Aspect Ratio
AoA	Angle of attack
CFD	Computational Fluid Dynamics
HPC	High-Perfomance Computing
LEV	Leading-Edge Vortex
MPI	Message Passing Interface Standard
NACA	National Advisory Committee for Aeronautics
PSD	Power Spectral Density
RMS	Root Mean Square
TEV	Trailing-Edge Vortex
2D	Two dimension, two dimensional
3D	Three dimension, three dimensional

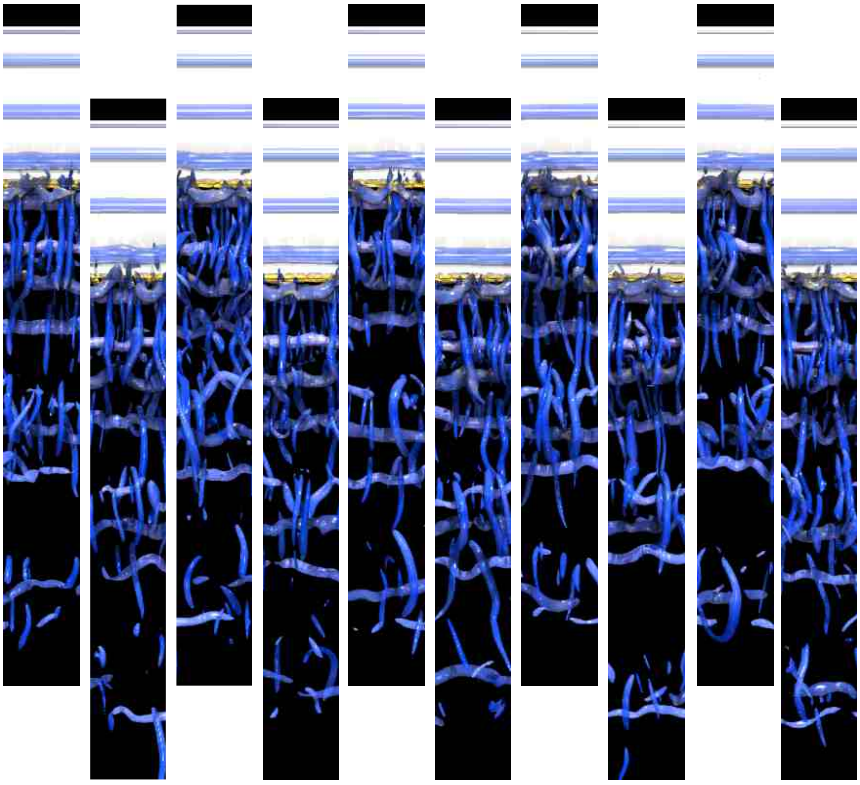

Chapter 1 Introduction to Propulsive Flapping

Biologists and engineers have long been interested in the locomotion of swimming and flying animals for the application of animal-like robots. Animals are widely studied because of their efficient self-propelled motions through intricate repetitive kinematics known as flapping, and the distinct planform shape of their limbs or wings. The current development of robots increases the need to imitate even on a deeper level such as maneuvering flexibility or sudden change of direction without huge momentum loss, operating-condition flexibility like ground effect and gust, and the capability of morphing planform for reducing drag and pitch/roll control. These types of capability are desirable for autonomous systems like micro air vehicles (MAVs), unmanned aerial vehicles (UAVs) and unmanned underwater vehicles (UUVs). Unlike animals, they are known to be less flexible and less efficient in terms of motions and structures, and we are slowly adding more natural features on them.

Besides its robotic purpose, the flapping mechanism is also found in energy harvesters and vehicle propulsion. The examples of energy harvester or energy generators are the wind and tidal turbines. Turbine blades experience unsteady dynamic loads, similar to the flapping wing. They are capable to generate higher efficiency in a certain way if the design is not stationary but flexible to rotate (pitching) adjusting to the incoming flow. Thus, they are more adaptive to a wider range of environmental conditions. Similar applications are found in air transport vehicles for generating efficient propulsion, higher lift and delaying stall such as the airplane wings with ailerons and helicopter rotor blades.

Animals' propulsion mechanisms in water and air are divided into four categories, i.e. oscillatory, undulatory, drag base and pulsating jet Smits (2019). The two last categories are not lift-based and will not be discussed in this work, i.e. pulsating jet (squids and jellyfishes) and drag base (land swimmers such as frogs, ducks, and human). The undulatory motion, seen in anguilliform such as eels, sea snakes, and several types of ray, belongs to animals that use traveling waves and high body-flexibility to propel the whole body against the fluid. The undulatory is also out of the scope of this thesis. Most efficient, fast and large animals in the sea and air are dominated by oscillatory propulsion or known as lift-based propulsion such as fishes, marine mammals and birds. Small bio-flyers like insects and sea creatures like sea-angel pteropods are also seen to oscillate for routine movement. In the next chapters,

(a) (b) (c) (d)

FIGURE 1.1: Lift-based animal propulsors are presented in colors for (a) mammal fluke, (b) fishtail (caudal fin), (c) flippers, and (d) wings.

the effect of twist on the foil span will also be studied as a controlled flexibility but the main function is not similar to the passive flexibility as in the undulatory propulsion, but rather a complementary effect to the oscillatory mechanism.

In this work, we are going to examine the flow over a rigid oscillating foil similar to fishtail (caudal fins), mammal flukes and flippers (see Figure 1.1), or generally known as the flapping foil. These propulsors provide the biggest forces to propel the animal's body against the fluid and are considered as the main source of forces. Whereas body thickness, for example in fast swimming fishes, contributes to secondary effect in oscillatory propulsion (Wu 2011). The relatively inactive body parts but sometimes flapping, like dorsal, pectoral, anal fins, finlets and rear flippers, mainly serve as stability and maneuver control. Despite that, some fishes like Mola mola sunfishes use their dorsal and anal fins called clavus as their lift-base propulsors similar to flippers.

1.1 Flow physics of oscillating bluff body and flapping foil

Characteristics of the flow over an oscillating bluff body such as a cylinder or a foil are related to the vortices generated in the wakes which can be expressed by the Strouhal number as a non-dimensional parameter reflecting their dynamics. The experiments of Koochesfahani (1989) prove that the axial flow of the wake vortices is highly affected by the amplitude and frequency of the oscillation. The maximum excursion of foil's trailing edge known as the double amplitude $2A$ and the frequency of oscillation f are the two major parameters defining the Strouhal number. The combination of f and A normalized with the free-stream velocity U_∞ is called the amplitude-based Strouhal number $St_A = 2Af/U_\infty$. The most effective flapping motions are found in the range of $St_A = [0.2, 0.4]$ for swimming animals as proven by (Triantafyllou et al. 1991, 1993). Most research is oriented in this range even though the natural range can be larger (Rohr & Fish 2004, Eloy 2012).

If both A and f or one of them is increased, the wake patterns show the transition from drag-producing to thrust-producing motion as shown in Andersen et al. (2016), Godoy-Diana et al. (2008), Schnipper et al. (2009). Certain wake types in flapping foil are known to either produce drag or thrust despite the controversy of their precise transition (Floryan et al. 2020).

The drag–thrust transition, shown by the blue line in Figure 1.2, is preceded by the change of vortex pattern from BvK (Bénard–von Kármán vortex) or other drag-producing types into rBvK (reverse Bénard–von Kármán) the thrust-producing. The transition is marked by the appearance of 2S wakes, or so-called the neutral wakes. They appear in both pure heaving (up and down movement) and pure pitching (rotating around its pivot point) following sinusoidal motions, although pure pitching needs to flap 75% faster than pure heaving to reach this transition (Zhang 2017). Complete samples for wake types are provided in Appendix A.

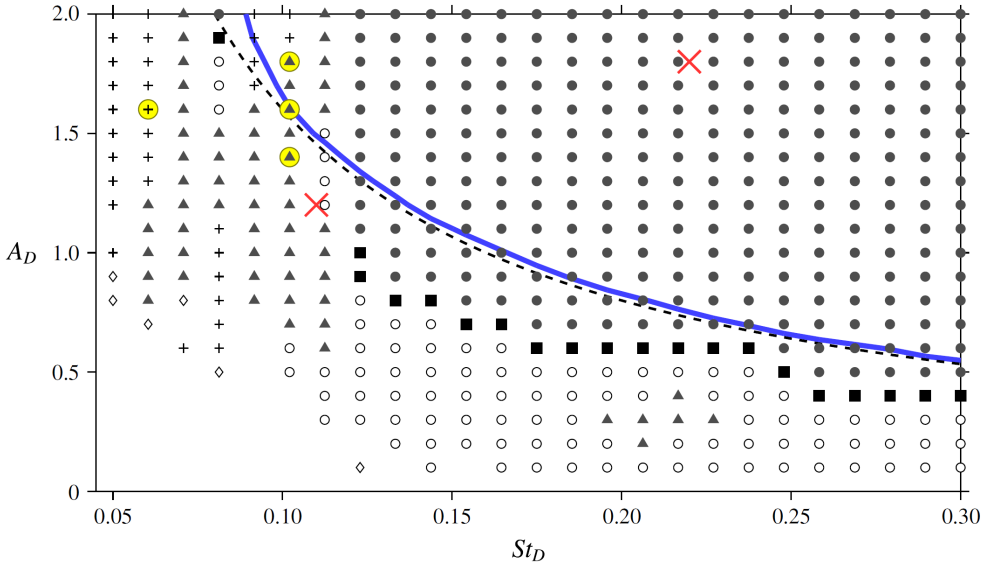

(*a*) Pure Heaving

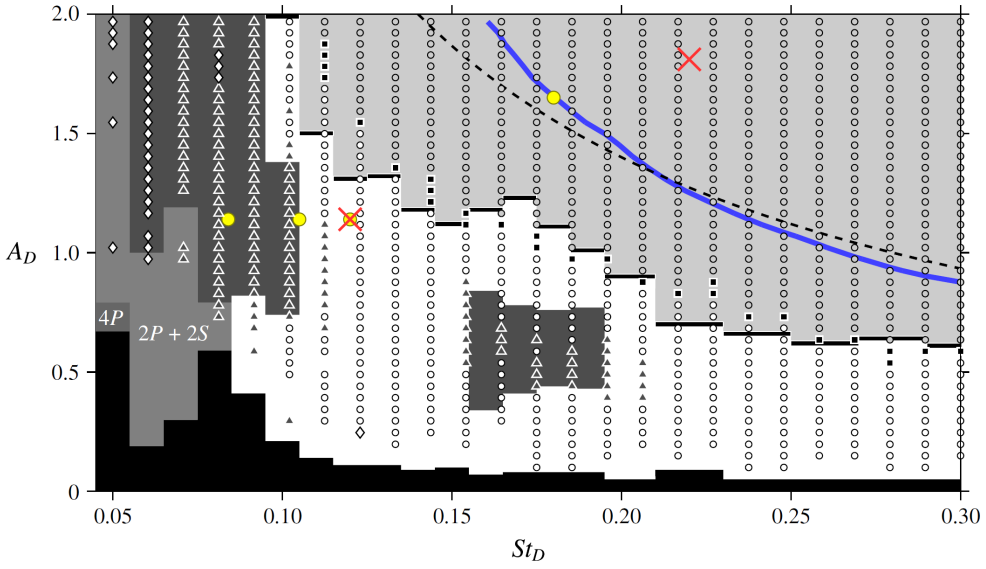

(*b*) Pure Pitching

FIGURE 1.2: Wake types by Andersen et al. (2016) with soap-film experiment for $A_D = 2A/D$ versus $St_D = fD/U_\infty$, where D is foil thickness. (○) BvK, (●) rBvK, (▲) 2P wakes, (■) 2S wakes, (+) 2P+2S and (◊) periodic vortex, blue line = drag–thrust transition, dashed black line = the nearest St_A line St_A=0.16 for heaving, St_A=0.28 for pitching)

A high-$\mathcal{AR}$ (aspect ratio) flapping foil has certain cross-sections experiencing two-dimensional (2D) kinematics, often considered as 2D foils for easier investigation, but they are not guaranteed to produce 2D flow. These sections are found along the tail and fluke which are relatively

unaffected by the tip. Similarly, the farthest cross-section from the root of a flipper or a wing experiences low rotational acceleration and more affected by the vertical translational acceleration. These sections can be analysed as a foil strip or an infinite foil experiencing a periodical vertical translation such as pure heaving, pitching and their combination. Even though both motion and geometry are two dimensional, foil's wakes are not always two dimensional as seen in the experiment of Koochesfahani (1989) where the axial flow parallel to span is discovered. A long and non-oscillating (stationary) cylinder is known to produce similar spanwise instabilities in the near wakes at certain Reynolds numbers. These instabilities are caused by the braid centrifugal effect or mode A (at $Re = 200$) and shear layer instability or mode B ($Re = 270$) (Williamson 1996, 2006). An oscillating infinite foil hypothetically should produce the same types of instability but probably at different Reynolds and Strouhal numbers.

Near-tip flow is highly affected by three-dimensional (3D) effects due to finiteness (tip effect), $\mathcal{AR}$ effect (ratio of the square of the foil span to planform area), and the ratio between motion amplitude and span. The three-dimensionality in finite foil is guaranteed not just for the flow over the tip, known as tip vortex, but it can be also on the vortices along the foil span if the $\mathcal{AR}$ relatively low. For the sinusoidal pitching plate, the tip and low-$\mathcal{AR}$ affect the dynamic of the leading-edge vortex (LEV) especially at higher frequency (Hartloper et al. 2012), or at higher amplitude (higher angle of attack) (Yilmaz & Rockwell 2011). Tip vortices of very low $\mathcal{AR}$ compress the LEV and induce spanwise vorticity transport inside the vortex core. This condition will affect the flow circulation and the force coefficients due to additional transient drag. In the case of translated plate, suppressing the tip flow is found to lower drag (Ringuette et al. 2007). Comparing the tip shape, the performance of the elliptical tip surpasses the rectangular tip, especially at high Strouhal case (Calderon et al. 2013). Besides foil $\mathcal{AR}$, the ratio between span and flapping amplitude is also important. Although the $\mathcal{AR}$ does not influence the efficiency except at $\mathcal{AR} < 0.83$ according to Buchholz & Smits (2008), the increase of amplitude to span ratio influence inversely to the efficiency. The behavior of tip-vortex interaction with onboard vortices in flipper-type flapping foil is rarely discussed compare to fishtail-type, and so is the $\mathcal{AR}$ effect.

The tip effect is closely linked to another 3D effect, i.e. the spanwise flow, a special feature of revolving (continuously rotating) and delta wings which can give hint to a flipper-type flapping foil. Along with the appearance tip vortices, the spanwise velocity and vorticity flux appear from root to tip on one side and opposite on the other side. Their influence on the stability of leading-edge vortex (LEV) is greater when $\mathcal{AR}$ decreases (Carr et al. 2013). The spanwise velocity in the revolving plate is induced by centrifugal and pressure gradient forces similar to the delta wing which are suspected to prevent separation of tip vortex and prolong the attachment of LEV (Garmann & Visbal 2014). Unlike revolving, the vortices on periodical flapping foil might not reach a fully formed state before they start another phase. Thus, the vortex-shedding pattern of the flipper-type flapping foil and its spanwise flow can be the combination between the initial stage of revolving and whole-span flapping such as pitching-up or heaving motions.

A subject of interest in flapping compared to stationary foil is the formation of strong LEV known to produce high lift force, its attachment duration, and how it can be affected by foil flexibility. The experiments of Ellington et al. (1996) postulate that an intense LEV is found to remain attached producing high lift on insect's flapping wings. Its mechanism is still debated between the stabilization caused by the spanwise flow (Ellington et al. 1996) and the vorticity attenuation due to downwash induced by previously shed wake vorticity (Birch & Dickinson 2001, Eldredge & Jones 2019). Lentink & Dickinson (2009) found that LEV remains attached in low Rossby number (ratio between inertia to rotational acceleration or Coriolis effect), whereas Reynolds number only affects the bursting of LEV. Slight foil flexibility is seemingly beneficial in the evolution of LEV but high flexibility can be detrimental. Passive spanwise flexibility in a pure heaving plate is found to increase lift (Barnes et al. 2013, Cleaver et al. 2016), whereas chord flexibility is more favorable to thrust (Cleaver et al. 2014, Van Buren et al. 2018). This suggests that span twist, a more controlled and combination of both chordwise and spanwise flexibility, can be beneficial for flapping foil.

1.2 A perspective of sweptback planform in bio propulsors

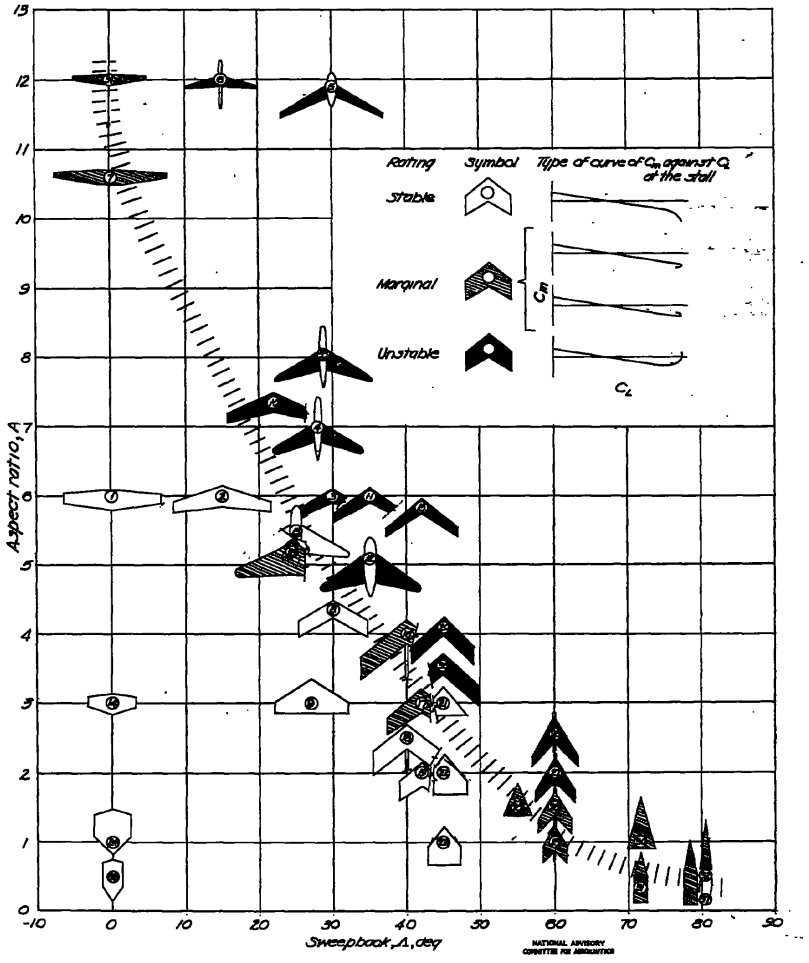

FIGURE 1.3: Longitudinal stability limit on swept wings by Shortal & Maggin (1946) showing $\mathcal{AR}$ is inversely proportional to the sweep angle.

An implication of having three-dimensionality effects such as spanwise flow and others is closely linked to a specific feature in animal's propulsors, i.e. the sweptback planform. A delta-wing planform has been a long interest to reduce drag. A study indicates that a certain combination of aspect ratio and sweep angles can produce stability for the near-stall flow (Shortal & Maggin 1946) as shown in Figure 1.3. All shapes above the stability-margin line in that figure correspond to unstable flight, and vice versa. If the flapping foil is similar to the steady delta wing, there will be a similar margin on both aspect ratio and sweep angle on which animals prefer. (Thomas & Taylor 2001) postulate that birds need to sweep their wing backward to counteract pitching-up moments for stability in an unstable and slow forward flight. The sweptback planform is also a common feature seen in fish caudal fins, the flukes of marine mammals, pectoral and dorsal fins (Fish & J. 1999, Fish & Battle 1995, Magnuson 1978, Gurdek Bas et al. 2015). Klaassen van Oorschot et al. (2016) run experiments using bird wing specimens proving an increase of 30% in vertical to horizontal force ratio during flapping motion. Despite their capability to sweep forward and backward —known as dynamic sweep or inline motion, swimming animals with flippers like turtle and penguin are found to have less forward sweep during vigorous swimming but high roll and twist angles as depicted by Davenport et al. (1997), Clark & Bemis (1979). It sparks a hypothesis that perhaps the sweptback feature has a benefit on the aero- or hydro-dynamics of animal propulsors.

Several analytical studies declare the benefit of sweptback planform, while there are several contradictory results from experiments. The potential-flow-based analysis shows that having a sweptback angle in propulsor is beneficial in flapping foils for reducing drags by Chopra & Kambe (2006), Liu & Bose (1993), van Dam (1987). However, current experimental results are showing that forces are not significantly changed between non-swept and sweptback features for foils or plates experiencing pure heaving (Beem et al. 2011), rotating (Lentink & Dickinson 2009), and even for a full body of manta ray robot (Arastehfar et al. 2019). Despite the insignificant force change, sweptback planform is reported to delay the formation and breakdown of LEV in a plate undergoing pitching (Onoue & Breuer 2017) and rolling but not heaving (Wong et al. 2013). Because of these uncertainties, the sweptback feature in flapping foils is an interesting subject and an important part in the study of nature-like flapping foils.

Numerical simulation is more suitable for isolating the pure effect of the sweep angle and to avoid more complex mechanical set up in the experiment. We can easily modify the sweep angle and still be able to combine it with other single or mixed parameters with simulation. This gives a freedom to match the sweptback planform to any kinematics giving the highest propulsion and efficiency provided by biologist data.

Studying flapping foils using the analytical method of classic potential flow shows dissimilar results with experiments due to the 3D effects. Calderon et al. (2013) compare the results of flapping foil experiment with the linear potential flow analysis showing that the potential flow contributes to the over-prediction of thrust force because of tip effects. For 3D effects, adjustments on analytical methods of unsteady potential flow based on Garrick's or Theodorsen's theories (Garrick 1936, Theodorsen 1935) must be added such as the contribution of large

amplitude separation shear layer and vortex proximity (Moored & Quinn 2019, Ayancik et al. 2019). This brings an interesting discussion in the next section about the importance of 3D numerical simulation for flapping foil.

1.3 Dimensionality effect and challenges in flapping foil computational method

Computational fluid dynamic (CFD) approach to solve Navier-Stokes equations (NS) surpasses other methods for flapping foil analysis but also has a drawback. It surpasses the experimental method for its flexibility on the number of modified kinematic parameters, non-repetitiveness, thin strip effect and infinite/no-end effect. It also surpasses the analytical method on detailed flow field data that can be extracted and analysis especially the turbulent breakdown and dissipation. However, when the Reynolds number increases, CFD has a disadvantage of being very expensive especially for 3D simulation. In order to overcome this problem, several comprehensive two-dimensional (2D) NS simulations are more preferable than a full 3D NS simulation. Strip theory is based on this approach and widely used with the assumption of no interaction between each strip so that their integration outcome is expected to be the same as running a full 3D simulation. This approach has some consequences.

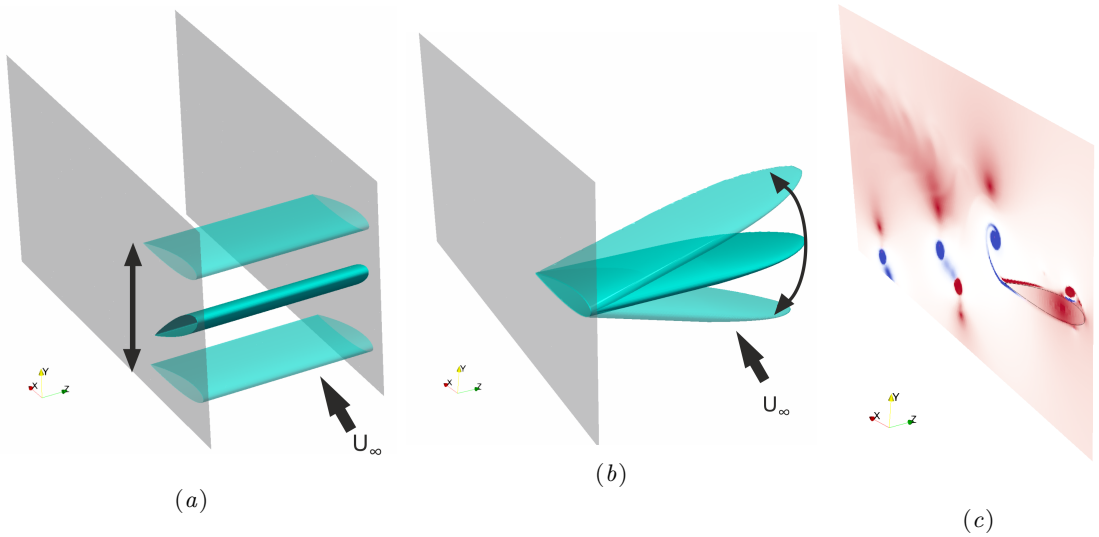

FIGURE 1.4: (a) An infinite foil experiences a fishtail-like motion, (b) a finite foil experiences flipper-like motion, and (c) a strip or 2D foil simulation.

The 2D simulations for stationary body are reported to produce incorrect flow fields even with sufficient grid refinement and the absence of 3D effects. A comparison of lift and drag coefficients between 3D and 2D simulations for steady foil at deep stall shows high fluctuation and irregularity in the 2D simulation that do not appear in 3D simulation (Taira & Colonius 2009). The force coefficient values are shown exaggeratedly higher in 2D simulation especially for a higher angle of attack. The difference between 2D and 3D simulation is presented for the flow over a stationary cylinder by Lei et al. (2001) for $Re = 1000$. At a given Reynolds

number, inaccurate prediction of global parameters and local flow fields are found in 2D simulation. The 2D flow separation is delayed and the recirculation area is shorter causing very low base pressure reading and over-predicted mean drag and lift-coefficient RMS. Mittal & Balachandar (1995) found similar results for circular and elliptic cylinders reporting higher Reynolds stresses in the 2D simulation that affects the mean pressure distribution. In the absence of 3D effects, the efficiency of 2D-strip simulation is found 10% higher than 3D infinite simulation (Bansmer & Radespiel 2012).

There has not been a comprehensive study about the comparison of 2D and 3D simulations for infinite oscillating foils, although several studies have reported the 3D effects on higher Strouhal numbers. On finding the similarity with Williamson (1996) for oscillating cylinder, Deng & Caulfield (2015) have reported the appearance of 3D spanwise instability behind the simulation of an oscillating foil with a cylindrical leading edge. In other publications, Deng et al. (2016, 2015) located the transitions region from 2D to 3D above the transition line of deflected or jet-like wake for both heaving and pitching motion for $Re = 1500$ inflow but without known Re transition location and clear cause of transition. Moriche et al. (2016) reported the same finding using NACA12 and $Re = 1000$ with an interesting conclusion. Despite the spanwise instability in the flow structures, the aerodynamic forces of 3D DNS are very close to its 2D simulation. This poses a question of whether running a 2D simulation for infinite oscillating foil is sufficient unlike for stationary bodies.

Numerical simulation is an appropriate tool to study the $\mathcal{AR}$ variation and tip vortex dynamic in flapping foil, but most studies are dedicated only for fishtail-type of kinematics and revolving wings. These studies are already conclusive, for instance, Drofelnik & Campobasso (2015) compare an $\mathcal{AR}$-10 foil experiencing heave and pitch and find that tip vortices reduce the power coefficient by 6% than the infinite foil. The same conclusion is found by Dong et al. (2005) for efficiency of very low $\mathcal{AR}$ in Reynolds number 100 to 400. Varying $\mathcal{AR}$ for revolving/rotating wings has been observed by Harbig et al. (2013), Jardin (2017). A rotating wing undergoes a similar effect as flapping but the unsteady effect from kinematics is only limited at the beginning of the rotation. Despite several finite cases for heave-pitch, there have not been conclusive 3D flapping simulations for flipper-like or wing-like motion with various $\mathcal{AR}$ especially for the comparison with 2D strip simulation.

Studying the flipper-type flapping kinematics requires special set-ups due to complex interaction between the fluid and solid parts. It is also important that the grid set-up to be consistent between 2D and 3D simulations. A simulation type of immersed boundary is suitable for this study. The following chapter is presented to explain briefly about the numerical tool used for all the studies in this work, the Boundary Data immersion Method.

1.4 Boundary data immersion method

This research is based on the computational method using a CFD package Lotus. A computational method is more suitable for studying the comparison between 3D and 2D flow

because of its integrity to maintain the same configuration such as grid density and domain, whereas general experiments (3D based) require different set-ups than the 2D-based method such as the soap film. The computational package —Lotus —is Boundary Data Immersion Method (BDIM) which was firstly introduced by Weymouth & Yue (2011) containing implicit LES solver and Cartesian grid. The set-ups for 3D and 2D simulation grids in Lotus can be made consistent to focus on the difference between the flow physics of 2D and 3D simulations. The following discussion will talk further about the difference between BDIM and former immersed boundary (IB) method or other IB derivative methods.

Immersed Boundary (IB) method was introduced by Peskin (2003) to study the fluid-structure interaction of biological movement and heart simulation. Peskin (2003) uses Dirac delta function as a kernel to switch between the Lagrangian part (the elasticity material equation) and the Eulerian part (the incompressible viscous fluid) in the boundary domain. The disadvantage of IB is the imposed boundary condition which is not trivial to resolve. Some parts of fluid, which are inside the solid and should not be resolved, are counted.

One of the earlier works of IB was also done by Fadlun et al. (2000). They explain that the solid part from NS equations in the conservation of momentum equation has been used in this initial research as the direct forcing method. Direct forcing is named based on the usage of forcing $\mathbf{f}$ discretized in time. The forcing is then related to the velocity imposed on the boundary without dynamical process (Fadlun et al. 2000) as one of the advantages of IB. The limitation comes from the boundary itself when the first grid points in the boundary don't resolve the NS. Instead, it enforces the velocity to the boundary from the linearization process. Further work for IB was also applied for solid particle flow by Uhlmann (2005). Uhlmann (2005) found undesired force oscillation for the particulate flow simulation from the method proposed by Fadlun et al. (2000). Thus, he proposed a smoother transfer between the Lagrangian and Eulerian locations as offered by Peskin (2003), viz. using regularized delta function for more stable force.

New research emerges to develop IB from the initial standard method to a more applicative one. Some modifications of Peskin (2003) Dirac delta kernel are offered using a 6-point kernel for force spreading and velocity interpolation for IB (Bao et al. 2016). Goza & Colonius (2016) used IB to simulate flow around the thin deforming body using linearization and block LU factorization to handle the non-linearity of the system. Nevertheless, this research has not solved the drawbacks of IB near the boundary domain.

BDIM, meanwhile, uses a robust and efficient Cartesian grid. BDIM itself is an analytic meta-equations for an immersed body in multi-phase flow with a smoothed interface domain using an integral kernel. Unlike the direct forcing method, BDIM modifies analytically the pressure term in the equation of motion. It also uses distance function to represent boundary instead of Lagrangian points as in other former IB. Those differences make BDIM have a smoother pressure field around the boundary. Later on, Maertens & Weymouth (2015) improved BDIM by adding higher-order term formula in the boundary interaction domain. This higher-order term even improves the accuracy of high Reynolds-number flow to reduce high-pressure

fluctuation because of the thin boundary layer. Despite the need for improvement on the skin friction prediction, BDIM is capable of resolving the flow up to Re 10^5 for moving bodies such as flapping foils. Hence, BDIM is suitable as the computational analysis tool for this research.

1.5 Goal of thesis, aims and objectives

The ultimate goal of this research is to characterize the 3D flow features on the flapping foil. This research aims to find the most crucial aspects of flapping foil undergoing propulsor locomotion of swimming and flying animals with the purpose of the advancement or the development of novel robotic and other related engineering applications. This research will only use the computational approach using Boundary Data Immersion Method (BDIM). The following points describe the objectives of the thesis per chapter.

1. Proving that the difference between 2D and 3D simulation for infinite foil is substantial (Chapter 3).
2. Finding the range where 3D simulation is more beneficial than 2D, or vice versa (Chapter 3).
3. Analysing the parameters affected by the appearance of spanwise structures on the flow (Chapter 3).
4. Analysing the most crucial 3D effects in finite foil in comparison with 2D strip or infinite foils (Chapter 4).
5. Characterizing the impact of 3D effects on forces, vortex structures and spanwise flow (Chapter 4).
6. Finding a possibility to scale 3D from 2D simulations (Chapter 4).
7. Quantifying the evolution of forces and efficiencies on sweeptback foils (Chapter 5).
8. Concluding hydrodynamic advantage/disadvantage of sweptback angle in comparison with biologist data (Chapter 5).

1.6 Structures of the thesis

This thesis is divided into 6 chapters with three of them are the main research projects. Chapter 1 consists of the introduction, literature review, research statement, objective and goals. In Chapter 2, the main methodology of this work will be explained generally including the setups of the simulation, the convergence studies and the validation in comparison with

experimental research from others. The specific setups or methods for each of the main projects will require separate explanations and will be placed in each of main-project chapters.

The first main project starts in Chapter 3 where the 3D flow features will be analysed for infinite flapping foil cases and compared with 2D strip cases. In most literature, the infinite foil is considered similar to the 2D case due to the absence of tip, periodic boundary conditions, and kinematics involving only the two-dimensional axis. In this chapter, we will discuss that this is not always true. Certain parameters define the transition between 2D and 3D features where the spanwise dimension is indeed crucial.

The fully 3D behavior of flapping foil is discussed in Chapter 4, where 3D effects are explored more extensively. In this chapter, the foil planform comprises a root and a tip while the kinematics are set to move in a three-dimensional axis. Each cross-section of finite foil is set to have identical kinematic with 2D strip or infinite foil comparable to Chapter 3 so that we can relate the flow directly to 2D strip cases. In this chapter, we also see that the forces of finite foil relate unexpectedly with the 2D strip cases which makes the 3D finite foil scaling from 2D strips possible.

The 3D simulation set-ups in the finite flapping from Chapter 4 will be extended with additional feature i.e. the variation of sweep angle in Chapter 5. In this way, we will see how the sweep angle seen in animal propulsors affects the flow. This chapter concludes the influence of sweptback planform in flapping propulsors and how this will be used to interpret biologist data collected from other publications.

The three main projects in this thesis have been and are under preparation for publications with the same title as the chapter names. They are located from Chapter 3 to Chapter 5.

1. Chapter 3: Zurman-Nasution, A. N., Ganapathisubramani, B. & Weymouth, G. D., *Influence of three-dimensionality on propulsive flapping.* J. Fluid Mech. 886 (2020). https://doi.org/10.1017/jfm.2019.1078.

2. Chapter 3: Hendrickson, K. , Zurman-Nasution, A. N. , Weymouth, G. D. , *Debunking the two-dimensional assumption on infinitely long wings.* APS Gallery of Fluid Motion (2018). https://doi.org/10.1103/APS.DFD.2018.GFM.V0103.

3. Chapter 4: Zurman-Nasution, A. N., Ganapathisubramani, B. & Weymouth, G. D., *Effects of aspect ratio on rolling and twisting foils.* Physical Review Fluids (accepted).

4. Chapter 5: Zurman-Nasution, A. N., Ganapathisubramani, B. & Weymouth, G. D., *Fin sweep angle does not determine flapping propulsive performance.* The Journal of Royal Society Interface (under consideration).

In addition, these works were presented by the Author in the following conference and symposium.

1. ECCM & ECFD Glasgow 2018. Minisymposia of the unsteady aerodynamics of small wings at moderate Reynolds numbers I: *3D influence on propulsive flapping at low Reynolds number.*

2. UK Fluids Manchester 2018. Session aerodynamics 2: *3D influence on propulsive flapping foil.*

3. 71st Annual Meeting of the APS Division of Fluid Dynamics Atlanta 2018. Session biological fluid dynamics, locomotion flapping: *3D influence on propulsive flapping at low Reynolds number.*

4. 72nd Annual Meeting of the APS Division of Fluid Dynamics Seattle 2019. Session tandem and flapping wings: *rolling and twisting of finite foil.*

5. 73rd Annual Meeting of the APS Division of Fluid Dynamics Chicago 2020 (virtual conference). Session biological fluid dynamics - locomotion and high Reynolds number swimming: *Sweep angle is negligible for propulsive flapping.*

Chapter 2 Methodology

The chapter explains the parameters used generally in the main projects from Chapter 3 to Chapter 5, while the specific parameters used for those projects will be explained in the designated methodology section in each chapter. This chapter also provides the studies for grid convergence and the validation with experiments.

2.1 General parameters

General parameters will be used in all simulations of the main project chapters. The foil uses a NACA0016 profile with chord length C and a foil thickness $D = 0.16C$ for main simulations, except in the validation with the experiment of stationary foil using NACA0012. There is no specific reason for thickness choice although large swimming-animals tend to have relatively thick foil-section for their propulsors. The flow separation is delayed at higher angle-of-attacks for thick airfoils (Uddin et al. 2017), giving benefit for flapping foils. An elliptic tip is chosen as a gradual transition of the tip to reduce the tip effect for the finite foil case Chapter 4. The Reynolds number of the inflow U_∞ is kept at $Re = 5300$ with viscosity $\nu = CU_\infty/Re$. This Reynolds number is in the range of shear-layer transition regime $Re \approx 1e3 - 1e6$ (Schlichting & Kestin 1979). In this regime, the same Strouhal number of flapping foil affects less on power and thrust coefficients except on bluff body drag (Senturk & Smits 2019). Different bluff body types like cylinder will shift the effective Reynolds number. This regime covers propulsor-size ranges from dragonflies to dolphins. Above the critical Re, the effect on Strouhal number is unknown. Whereas, small animals (low Re) use a different mechanism such as a clap-and-fling motion to generate high lift.

The flapping kinematics are characterized by the amplitude-base Strouhal number or $St_A = 2Af/U_\infty$. Both the amplitude and frequency part can be separated as $St_A = St_{l^*} \cdot A_{l^*}$ into

$$St_{l^*} = \frac{fl^*}{U_\infty} \qquad A_{l^*} = \frac{2A}{l^*} \tag{2.1}$$

where l^* can be defined from any length parameter such as D, C, or other lengths, adjusting the context of the kinematics and planform shapes. The foil will have an offset angle-of-attack

(AoA) called the bias angle θ_{bias} either at 10° or 0° (no bias angle). Bias angle 10° is used to sufficiently perturb the flow at stationary motion to create 3D structures along the span.

The results will be presented in the coefficients of lift force C_L, thrust force C_T, drag force C_D (or $-C_T$), pitching moment C_{Mz} and power C_{pow}, which can be defined as

$$C_T = -\frac{F_x}{0.5\rho S_p U_\infty^2}, \qquad C_L = \frac{F_y}{0.5\rho S_p U_\infty^2}, \tag{2.2}$$

$$C_{Mz} = -\frac{M_z}{0.5\rho S_p U_\infty^2 C}, \qquad C_{Pow} = \frac{P}{0.5\rho S_p U_\infty^3}, \tag{2.3}$$

where measured thrust force $(-F_x)$, lift force (F_y), pitching moment $(-M_z)$, and power (P) are calculated from the integration of pressure and viscous forces over the foil. S_p is the foil planform area and overline signifies cycle averaging.

The efficiency is defined based on the ratio of mean thrust and mean power $\eta = \overline{C_T}/\overline{C_{pow}}$. The unsteadiness is presented using standard deviation σ (RMS is zero-mean σ), variance σ^2 and fast Fourier transform or FFT of the force coefficient data.

All vortex-structure visualizations are constructed using Paraview which will be presented in spanwise vorticity $\omega_z C/U_\infty$, λ_2-, and $Q-$ criterions. Q is defined as $Q = \frac{1}{2}(\|\boldsymbol{\Omega}\|^2 - \|\boldsymbol{S}\|^2)$, where $\boldsymbol{\Omega}$ is vorticity and $\boldsymbol{S}$ rate-of-strain tensors. Q presents a vortex as a connected fluid region with a positive second invariant of velocity gradient tensor $Q > 0$, while λ_2 the second eigenvalue of $(\boldsymbol{\Omega}^2 + \boldsymbol{S}^2)$ is presented as $\lambda_2 < 0$. The iso-contour of 1% maximum value is deemed sufficient for clarity in $Q-$criterion (King et al. 2018), and similarly to 1% of minimum value for λ_2-criterion.

2.2 Convergence

Lotus arranges grids as depicted in Figure 2.1. A foil is placed in the uniform Cartesian grids with cell size Δx, Δy, Δz consecutively in streamwise, lateralwise, and spanwise. Outside of the uniform zone, the grids are stretched with a maximum growth rate maintained below 8%. The spanwise grid is either totally uniform with $\Delta z/\Delta x = 3$ (explained further in Section 2.2.2) in the infinite case or stretched in the finite case. All 3D simulations are run in HPC Iridis 4 Southampton to speed up a simulation using MPI for parallel computating.

2.2.1 Streamwise and lateralwise grid convergence

The graphs in Figure 2.2 present the study of grid convergence study for $C/\Delta x$ (streamwise) and $C/\Delta y$ (lateral direction). The parameters for this study are NACA16, $Re = 5300$, coupled motion, $2A/D = 1$, $fD/U_\infty = 0.3$, and bias angle 10°. As the grid increased, the implicit LES solver presents more small structures. On the contrary, coarsening the grids will smoothen the small structures and incorrectly predict mean force coefficients.

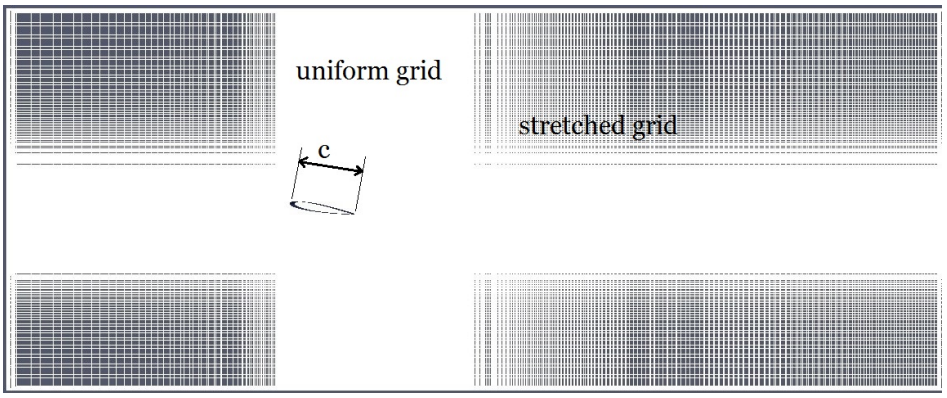

FIGURE 2.1: Lotus grid arrangement

The relative error ε is calculated to the maximum refined grid $C/\Delta x = 256$ as $(n-n_{max})/n_{max}$, where n is the reviewed value. The convergence study presents zero-mean standard deviation σ_0 or RMS values for lift C_L and thrust C_T coefficients. The RMS is more suitable to represent flapping foils (unsteady simulations) than the mean values of force coefficients which tend to oscillate around zero. The simulation relative error $\varepsilon \leq 3.3\%$ for 2D and 3D are deemed sufficient to capture the 3D effects. This error value is equivalent to 3.7% off to the grid-independent solution based on Richarson extrapolation.

2.2.2 Spanwise grid convergence for stationary foil

The spanwise grid (z direction) is coarsened and presented in Figure 2.3. This study is obtained using stationary foil NACA0012, $C/\Delta x = 150$, $AoA = 10°$ and at $Re = 5300$. For $\Delta z/\Delta x = 3$, the relative error for C_L and C_D are below 2%. At $\Delta z/\Delta x \geqslant 4$, there is an increase in relative error. The grids become very coarse and the convergence is no longer monotonic. At a low value of $\Delta z/\Delta x$, the computation cost is more expensive. Thus, it is more advantageous to use $\Delta z/\Delta x = 3$ for further simulation. This coarsening study was repeated with $Re = 5.1e^4$ and produced the same tendency. The same results for NACA0016 are expected at the same angle of attack and Reynolds number.

2.3 Validation with experiment

2.3.1 Infinite stationary foil

Lotus is validated using the experimental results using NACA0012 from Alam et al. (2009), Zhou et al. (2011), Wang et al. (2014) for stationary foil. The simulation domain sizes replicate the ones in the experiment. Both Alam et al. (2009), Zhou et al. (2011) state that they have used a blockage corrector for C_D and C_L. Their blockage corrector methodology refer to Maskell (1965), which is modified by Hackett & Cooper (2016) for the calculation of

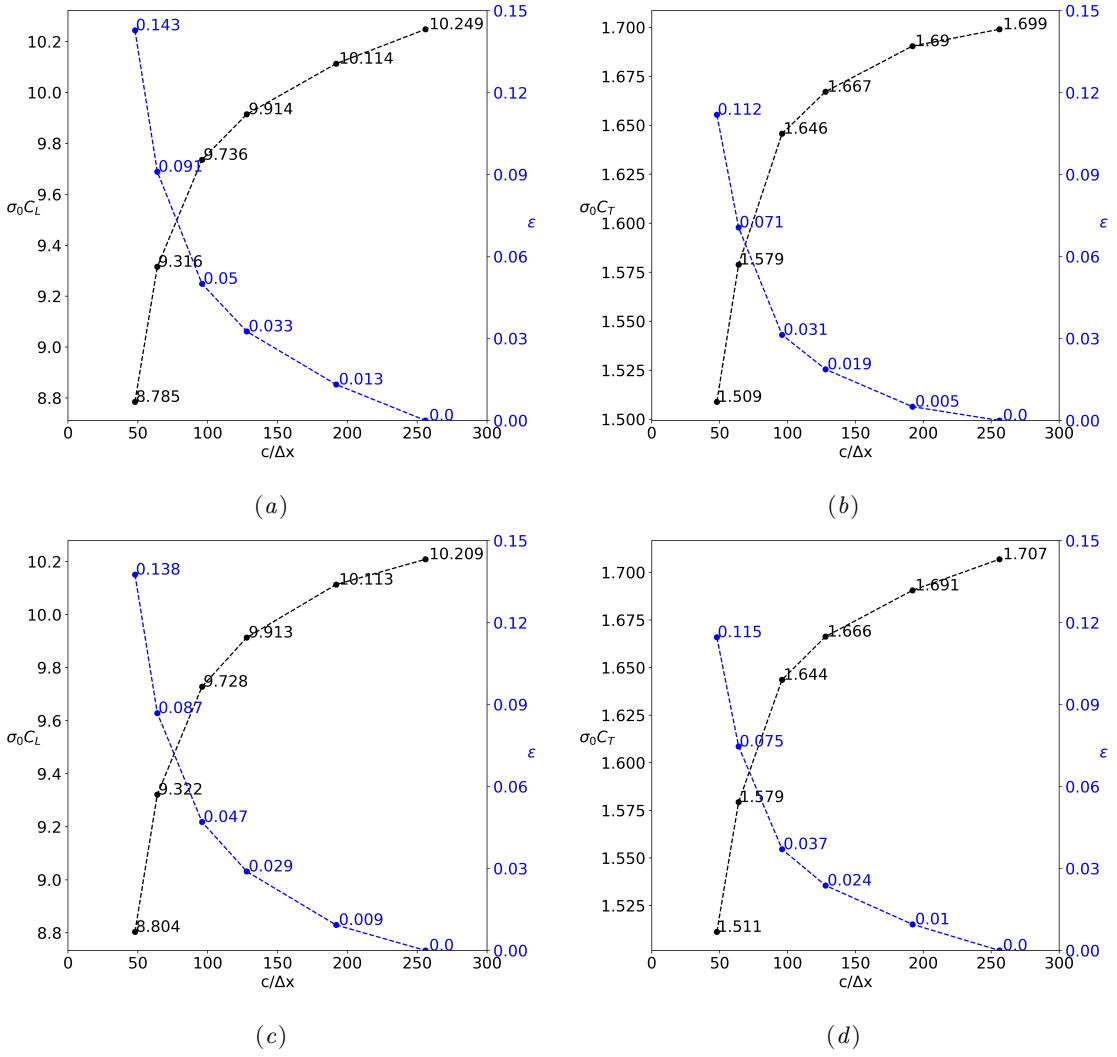

FIGURE 2.2: Convergence studies are presented in zero-mean standard deviation σ_0 (RMS) of force coefficicents. Black lines are the nominal value for σ_0 at $C/\Delta x = 48, 64, 96, 128, 192, 256$, while blue lines are the relative errors to the highest nominal grid $C/\Delta x = 256$ for (a, b) 2D and (c, d) 3D simulations.

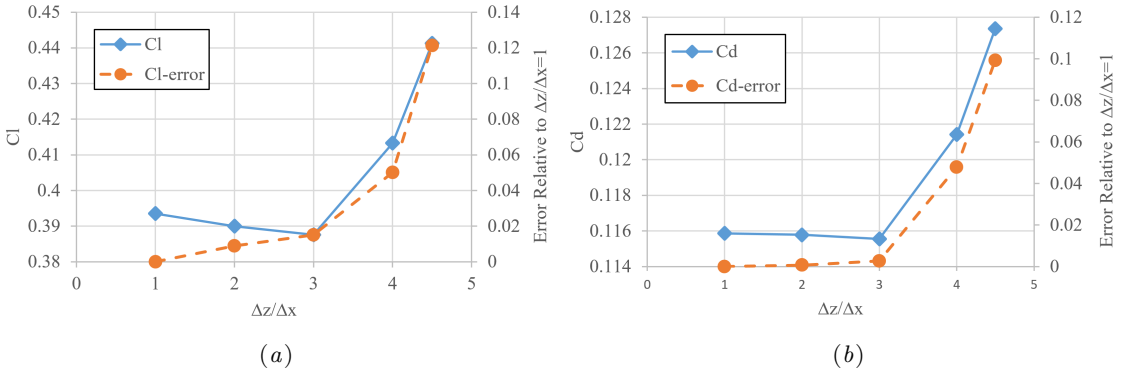

FIGURE 2.3: Spanwise coarsening study, (A) C_L, (B) C_D. Error presented is relative to the lowest dz/dx

Source	Re	AoA (°)	$\overline{C_L}$	$\overline{C_D}$	fC/U_∞
Alam et al. (2009), Zhou et al. (2011) (corrected)	5.3e3	10	0.39	0.14	1.3
Alam et al. (2009), Zhou et al. (2011) (uncorrected)	5.3e3	10	0.45	0.15	-
Wang et al. (2014)	5.3e3	10	0.47	0.14	-
Lotus	5.3e3	10	0.44	0.13	1.35
Alam et al. (2009), Zhou et al. (2011) (corrected)	5.3e3	40	0.84	0.90	0.23
Alam et al. (2009), Zhou et al. (2011) (uncorrected)	5.3e3	40	1.12	1.22	-
Lotus	5.3e3	40	1.24	1.14	0.31

TABLE 2.1: Experimental results are compared with Lotus at $Re = 5300$ for stationary NACA0012. Uncorrected values are calculated based on Maskell III method. The values of fC/U_∞ are the frequency of vortex shedding measured as the PSD peak of C_D signals.

C_D and C_L (Maskell III method). For this validation, Lotus results are obtained using 3D simulations with parameters $C/\Delta x = 150$, $\Delta z/\Delta x = 3$ and span length$/C = 1$.

The results in Table 2.1 present the value of C_D and C_L corrected for $Re = 5300$ at two AoA at 10° and 40°. To get uncorrected results, the blockage corrector method from Maskell III is used. For a fair comparison, Lotus results in Table 2.1 should be compared with uncorrected experimental C_D and C_L. Table 2.1 shows comparison between Lotus and the experiment results for C_D and C_L for $Re = 5300$. The relative error for Lotus $\overline{C_L}$ from Alam et al. (2009) uncorrected result are 2.2% and 10.7% for AoA 10° and 40° consecutively, whereas for $\overline{C_D}$ are 13.3% and 6.5%. Apart from mean forces, the wake streamwise velocity contours in Figure 2.4 of Lotus at $Re = 5300$ correspond well with the experiment from Alam et al. (2009) despite a slight deviation in separation region and at the highest velocity gradient area near the leading edge and trailing edge.

Discrepancies between Lotus and the experiment might come from several things. The experiment most probably uses an imperfect NACA12 with a blunt trailing-edge and non-smooth surface causing more attached flow on the foil's suction side. Other discrepancies come from non-uniform inflow, turbulent intensity and blockage-effect calculation. From the numerical side, the relative errors of mean forces look bigger when the values are closer to zero, and averaging force calculation in highly turbulent flow like in AoA 40° unavoidably contains higher noise. The main difficulty of IB lies on the closest grid to the boundary without a wall model. Lotus especially struggles more inside the boundary layer and the separation area without refining grids. The more the iLES grids are refined, the closer the results to DNS. An effort is done to refine grids lateralwise to $\Delta y/\Delta x = 1/5$ at 40° AoA resulting a vortex shedding frequency of 21.2% discrepancy from the experiment which is originally 34.2% in Table 2.1. This small improvement costs excessive computational resource, viz. simulation time to 16 times longer with core numbers to 5 times more. Thus, similarly refined grids are unnecessary to be used further. In flapping cases for the same Reynolds number, the unsteady flow is dominated more by the inertia effect of the kinematics and less by the viscous effect. Thus, Lotus' weakness in the viscous boundary layer can be ignored. Validating Lotus against the experimental results for stationary foils is more conservative than for flapping foil. The errors for flapping foils are expected to be lower than the stationary foil cases.

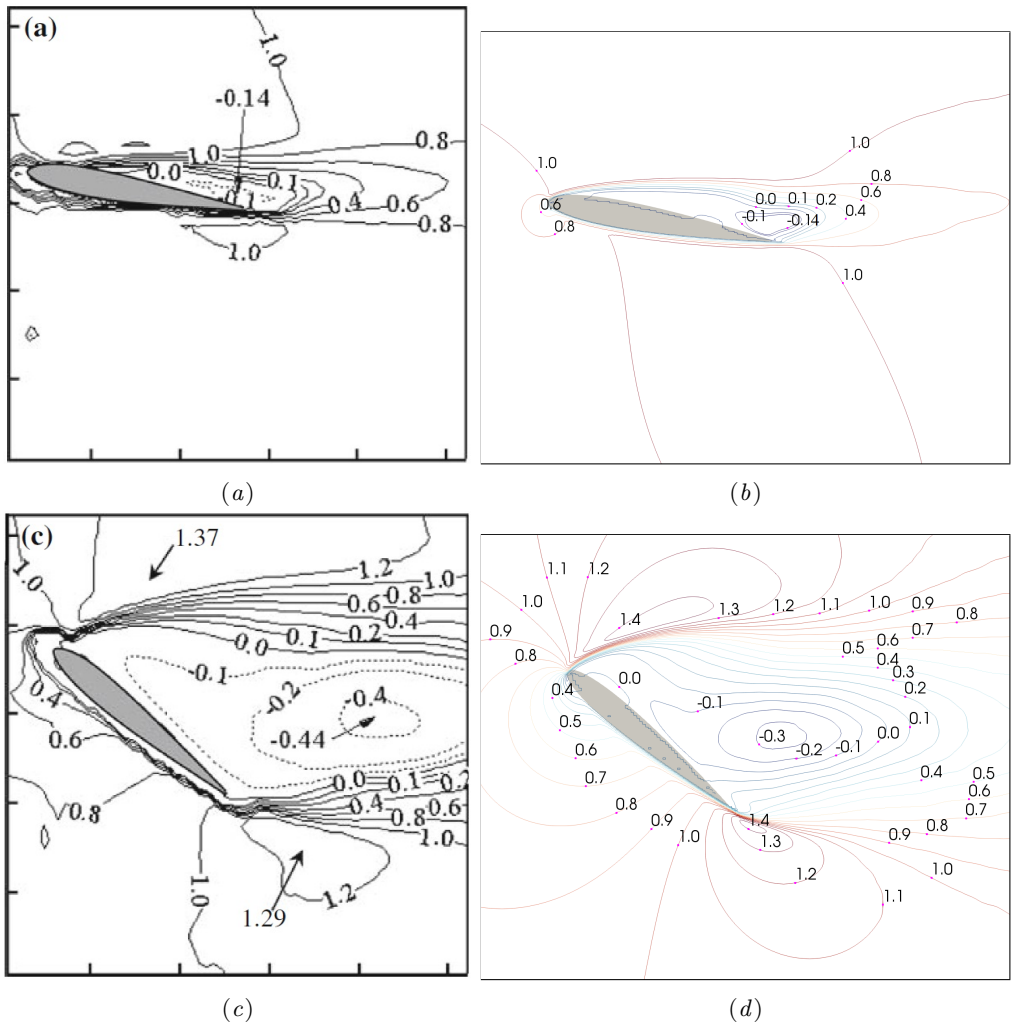

FIGURE 2.4: Mean streamwise velocity contour of experimental results of steady foil (Alam et al. 2009) for (a) $Re = 5300$, at 10°, (c) $Re = 5300$, at 40°, with corresponding Lotus results (b,d)

2.3.2 Finite flapping foil

The flapping finite foil case is validated against the experiment of King et al. (2018) in Figure 2.5 for Chapter 5. This is a validation of the unsteady-wake amplitude and frequency generated by the kinematics. Experiment uses rigid trapezoidal plate with mid chord $C = 101mm$, span length $b = 254mm$ and $\mathcal{AR} = 4.17$ in an inflow of $Re = 5800$ or $U_\infty = 57$m/s. The motion is pure pitching with pitching amplitude $\theta = 7.5°$ and $St_A = 0.46$ which is constructed from reduced frequency $k = fC/U_\infty = 1.772$ and specific amplitude $2A/C = 0.261$. The same motion parameters are applied to Lotus using NACA16 finite foil with elliptic tip experiencing sinusoidal pitching and fixed sweep angle 45°. There are small insignificant differences in simulation such as $Re = 5300$, $\mathcal{AR} = 4$, and NACA16 cross-section and concave trailing-edge for the coherence with simulations in Chapter 5. In the simulation, the chord length starts at the root $z = 0$ and ends when the tip vortex starts to be equivalent to the experiment chord-length. Both simulation and experiment show general similarity in the wakes especially for the wake shape, spanwise vorticity, phase, frequency and amplitude of

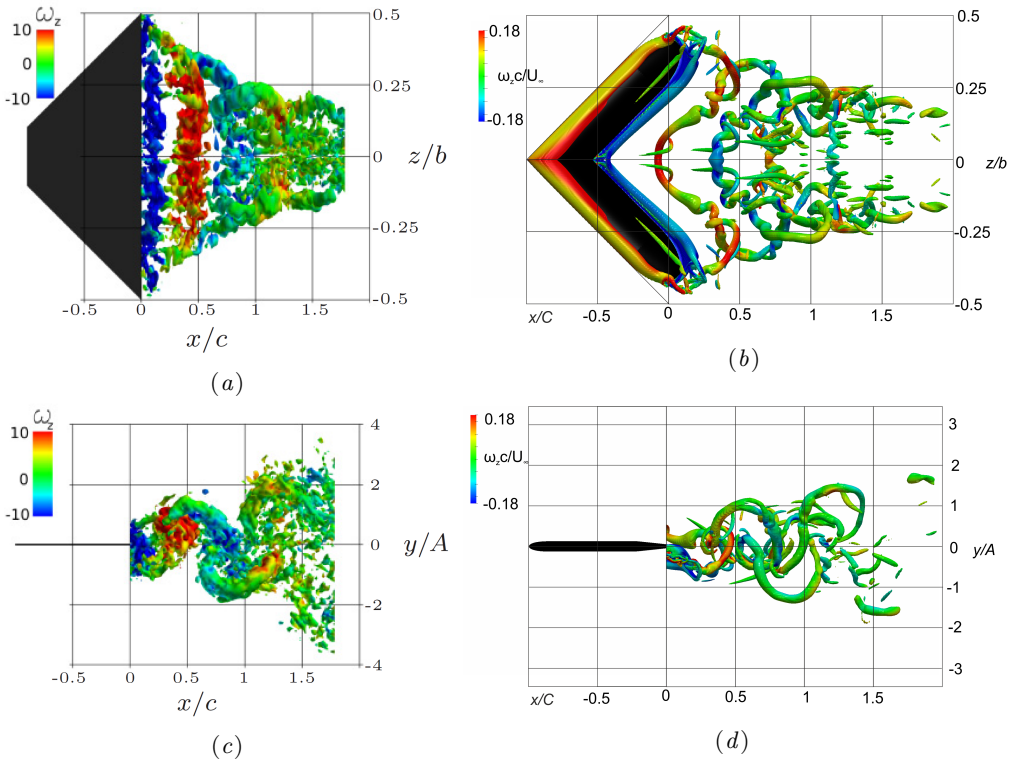

FIGURE 2.5: Lotus 3D pitching foil using NACA16 in (b) and (d) is validated using trapezoidal plate (a) and (c) from experiment of King et al. (2018). Isocontours are presented in phase average of 1% of max Q-criterion, while the colors represent the same values of spanwise vorticity. Axial direction x is normalised with chord C while lateral y with oscillation amplitude A. Parameters are the same both simulation and experiment except the planform and thickness. Lotus simulation are mirrored with $z = 0$ for visualization purpose.

vortex shedding. The simulation shows smaller Q isocontours which can be caused by smaller area (lower $\mathcal{AR}$) and concave trailing-edge promoting wake suction. According to Van Buren et al. (2017), the 45° will decrease the thrust by $\Delta C_T \approx 0.1$ and efficiency by $\Delta\eta \approx 0.03$, which explain the smaller Q contours. There is no force data from provided in the experiment of King et al. (2018) for comparison, but both the experiment and Lotus simulation show inverse BvK wakes indicating the thrust-producing wakes. The latest version of Lotus (second-order BDIM) has been validated with an experiment for a pithing and heaving foil in Maertens & Weymouth (2015). The mean drag coefficients converges within 5% for $Re = 1e5$ using grid resolution $C/\Delta x = 67$.

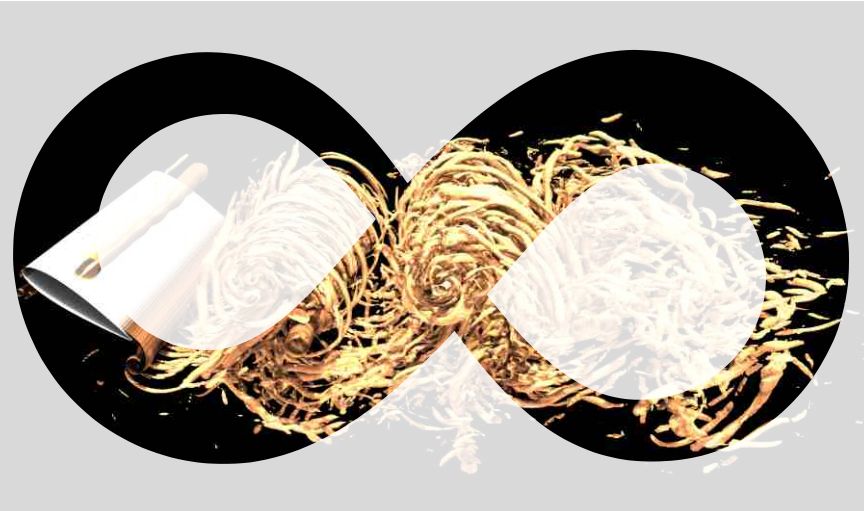

Chapter 3 Influence of three dimensionality on infinite flapping foil

Abstract

Propulsive flapping foils are widely studied in the development of swimming and flying animal-like autonomous systems. Numerical studies in this topic are mainly two-dimensional (2D) studies as they are quicker and cheaper, but, this inhibits the three-dimensional (3D) evolution of the shed vortices from leading- and trailing-edges. In this work, we examine the similarities and differences between 2D and 3D simulations through a case study in order to evaluate the efficacy and limitations of using 2D simulations to describe a 3D system. We simulate an infinite-span NACA0016 foil both in 2D and 3D at a Reynolds number of 5300 and an angle-of-attack of 10°. The foil is subject to prescribed heaving and pitching kinematics with varying trailing-edge deflection amplitude A. Our primary finding is that the flow and forces are effectively 2D at *intermediate* amplitude-based Strouhal numbers ($St_A = 2Af/U$ where U is the freestream velocity and f is the flapping frequency); $St_A \approx 0.3$ for heaving, $St_A \approx 0.3$–0.6 for pitching and $St_A \approx 0.15$–0.45 for coupled motion, while 3D effects dominate outside of these ranges. These 2D regions begin when the fluid energy induced by the flapping motion overcomes the 3D vortex shedding found on a stationary foil, and the flow reverts back to 3D when the strength of the shed vortices overwhelms the stabilizing influence of viscous dissipation. These results indicate that 3D-to-2D transitions or vice-versa are a balance between the strength and stability of leading-/trailing-edge vortices and the flapping energy. 2D simulations can still be used for flapping flight/swimming studies provided the flapping amplitude/frequency is within a given range.

3.1 Introduction

Engineering applications such as MAVs (micro air vehicles) and energy harvesting are designed to mimic the propulsive flapping mechanism of swimming and flying animals although these applications are less efficient. The early research on propulsive flapping of swimming animals by Triantafyllou et al. (1991, 1993) set a range for effective Strouhal numbers ($St_A = 2Af/U$, where A is the trailing-edge amplitude, f is the flapping frequency and U is the freestream velocity) as 0.25–0.35, but it was argued only for large aspect-ratio (AR) tails (Eloy 2012, Rohr & Fish 2004). Nevertheless, flapping foil research primarily focus on St_A = 0.2–0.4 as proven by experiments where interesting transitions exist, i.e drag–thrust transition and wake transition from Bénard-von-Kármán (drag-producing) to reverse Bénard-von-Kármán (thrust-producing) vortex street (Andersen et al. 2016, Godoy-Diana et al. 2008).

The majority of numerical studies for flapping foil are mostly in 2D—due to its simplicity and cost savings—and have shown consistency with experiments. Koochesfahani (1989) indicated that the flow at certain range of St_A over a high $\mathcal{AR}$ foil, which experiences periodical 2D motions such as pure heaving and pure pitching, is mostly assumed to be 2D. Researchers found that soap film experiments agreed with 2D simulations (Andersen et al. 2016, Schnipper et al. 2009, Zhang 2017), and high $\mathcal{AR}$ foil experiments agreed with 2D simulations (Moriche et al. 2016, Muscutt et al. 2017). These studies, however, did not explain why the flapping foil being subjected to periodic high angles of attack remains two-dimensional while a stationary foil at the same (or similar) angles of attack experiences strong separation (Uddin et al. 2017) where 3D effects are not negligible.

Despite experiments using high $\mathcal{AR}$ foils to ensure 2D flow, three-dimensional effects should not be ruled out. Apart from tip vortices, the effect of leading-edge vortices (LEVs) has been shown to be important for high $\mathcal{AR}$ rotating wings (Fu et al. 2015, Lu et al. 2006, Carr et al. 2013). These vortices are the major contributors for force evolutions in flapping foil especially along the span because LEVs stabilise the spanwise force-variations (Triantafyllou et al. 2004) but only at low Rossby ($Ro = R/C$, where R is wingtip radius and C is mean chord length) as stated by Lentink & Dickinson (2009). At higher Ro, the LEVs are unstable due to Coriolis acceleration creating spanwise instability which is also predicted by Williamson (2006) for flow over a circular cylinder. These 3D effects have consequences on the 2D assumption for predictions, especially in spanwise force-fluctuations and would lead to inaccuracies in global parameters and local flow fields (Lei et al. 2001, Garcia et al. 2017), delayed and shortened recirculation area causing very low base pressures and over-predicted mean drag and lift-coefficient fluctuations (Mittal & Balachandar 1995).

In very recent work, the appearance of 2D to 3D transition in flow structures was observed by Deng et al. (2016). This was based on linear Floquet stability without any comprehensive 3D simulations thereby making the source/regime of this transition uncertain. In this work, this 2D to 3D transition is investigated using comprehensive 2D and 3D simulations across

the range of flapping kinematics, including the analysis of average and fluctuating force-coefficients, vorticity metrics and energy distribution. The results demonstrate the limitations of strip theory and the parameter space where there is a need for full 3D simulations to examine propulsive flapping mechanisms of animals and animal-like like autonomous systems.

3.2 Methodology

3.2.1 Kinematics

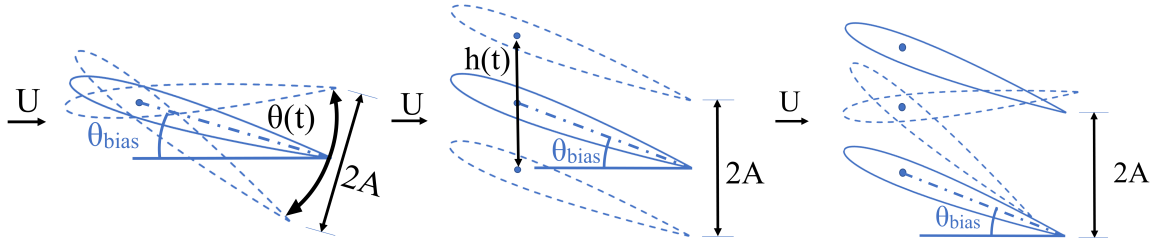

FIGURE 3.1: Kinematics with bias angle-of-attack, (a) pitching, (b) heaving and (c) coupled motions.

The foil used in this research is NACA0016 with thickness $D = 0.16C$, where C is the chord length. The foil is placed in uniform flow with constant inflow speed U and fluid density ρ. The Reynolds number of $Re = UC/\nu = 5300$ was chosen in order to be in the middle of Reynolds number regime of flapping flyers and swimmers ($1000 < Re < 10000$). Moreover, this Reynolds number also corresponds to the shear-layer transition regime of Williamson (1996). Finally, the simulations at higher Reynolds numbers ($Re \approx 10600$) for a limited number of cases did not change the conclusions reached in the following sections.

The governing kinematic parameter is the amplitude-based Strouhal number $St_A = St_D \cdot A_D$. In order to isolate the amplitude and frequency, we use

$$St_D = \frac{Df}{U} \qquad A_D = \frac{2A}{D} \tag{3.1}$$

where St_D is the thickness-based Strouhal number, A_D is the thickness-based amplitude, f is the frequency of flapping (in Hz) and the double amplitude $2A$ is measured at the trailing edge.

The foils are prescribed to undergo pure heave h, pure pitch θ and coupled pitch and heave. The motions are harmonic, with functional form

$$h(t) = A\sin(2\pi ft) \tag{3.2}$$

$$\theta(t) = \theta_0 \sin(2\pi ft + \psi) + \theta_{\text{bias}} \tag{3.3}$$

$$\theta_0 = \sin^{-1}\left(A/(0.75C)\right) \tag{3.4}$$

The pivot point for pitching motion is $0.25C$ from the leading edge. The coupled motion has a phase angle $\psi = 90°$, which was found as the most effective for propulsive flapping (Isogai et al. 1999). Due to this phase angle, pitching lags behind heaving for a quarter of a cycle causing it to be at minimum $\theta(t)$ when heaving has reached maximum $h(t)$. A bias angle-of-attack is employed to focus on lift-producing propulsive motion used mainly by bio-flyers, although some swimming animals were also reported to benefit from lift e.g. shark's pectoral fins. The bias angle-of-attack is fixed at $\theta_{\text{bias}} = 10° = \pi/18$ rad. This 10° angle is chosen because it sufficiently induces unsteadiness to the flow for stationary foil case.

In this work, we vary St_A by discretely increasing the amplitude from $A_D = 0.0625$–3.75 but keeping the frequency fixed at $St_D = 0.3$ following one vertical line in St_D-versus-A_D map of Andersen et al. (2016). This frequency is slightly above the stationary-foil vortex shedding frequency.

3.2.2 Measurement metrics

Results are presented based on thrust- (C_T) and lift- (C_L) force coefficients as follows:

$$C_T = -\frac{F_x}{0.5\rho S_p U_\infty^2} \qquad C_L = \frac{F_y}{0.5\rho S_p U_\infty^2} \tag{3.5}$$

where measured thrust force ($-F_x$) and lift force (F_y) are calculated from the integration of pressure and viscous forces over the foil and S_p is the foil planform area. The mean, variance and power-spectral-density analysis of force-coefficient time-histories are used to highlight the differences across different kinematics.

3.2.3 Computational method

For computational consistency between 2D and 3D simulations, the 3D grids are the spanwise extrusion of 2D grids and both simulations use Lotus as computational tool. Periodic boundary conditions are enforced along the spanwise direction of the foil and a span length of $6C$ is used for 3D simulation. The verification of grid convergence for 2D and 3D were carried out at $Re = 5300$ to identify the appropriate grid required and presented in Section 2.2. As a balance between the grid resolution and the number of simulations, a resolution of $C/\Delta x = 128$ is deemed sufficient to captures the dynamics of the flow and the parametric study in the following sections were carried out at this resolution but at a higher Reynolds number. A 3D simulation for a stationary NACA0012 is compared with the experiment result of Wang et al. (2014) in figure 3.2 showing an accurate instability location, and the drag coefficient is within 5%. The errors associated with mesh are also provided in Table 2.1.

FIGURE 3.2: Accuracy comparison for instability starting-location of stationary NACA0012 at $Re = 5300$ and angle of attack 10°, (a) LIF flow visualisation of Wang et al. (2014), mean drag-coefficient $C_D = 0.14$, and (b) spanwise-vorticity of 3D simulation, $C_D = 0.133$. The instability starts at the first vortex roll-up.

3.3 Comparison between 2D and 3D simulations

The two- and three-dimensional simulations are further compared based on the vortex-structure evolution, mean force-coefficients ($\overline{C_T}$ and $\overline{C_L}$), phase-averaged spanwise component of vorticity and fluctuations of force-coefficient signals.

3.3.1 Overview and flow structures

Figure 3.3 shows the variation of $\overline{C_T}$ with St_A for 2D and 3D simulations across three different kinematics (heave, pitch and coupled motions). The inset in the figures also show iso-surfaces of spanwise vorticity (ω_z) for a few selected cases (the cases as indicated with arrows in the figure). Starting at the lowest A_D (the lowest St_A), the flow structures appear to be three-dimensional with strong separation on the foil suction-side similar to a stationary foil. The values of $\overline{C_T}$ for both 2D and 3D simulations appear to be very similar to the $\overline{C_T}$ of a stationary-foil with the small discrepancy between 2D and 3D simulations.

With a slight increase in amplitude, the flow structures appear to be more coherent and become more two-dimensional. The $\overline{C_T}$ of 2D and 3D simulations now collapse to the same value(s). These 2D structures are found to persist at around $A_D = 1$ or $St_A = 0.3$ in all three types of motion. The beginning of 2D flow structures is accompanied by propulsive wakes evolving to reverse Bénard-von-Kármán in coupled motion or to asymmetric/deflected in heave and pitch. When A_D increases even higher, the 3D flow structures reappear eliminating the uniform 2D structures. They are followed by a substantial discrepancy in $\overline{C_T}$ between 2D and 3D simulations. The vortices appear to breakdown along the spanwise direction in the wake and this breakdown starts to creep up to the trailing-edge with increasing amplitude, which is consistent with the observations of Moriche et al. (2016). The flow structures at the trailing-edge are more "chaotic" along the spanwise direction, while the leading-edge vortices are relatively coherent along the span even at higher A_D.

The appearance of uniform 2D structures in all three types of motion shows that 2D simulations would indeed be sufficient over a certain range of Strouhal numbers, but the ranges are not the same for the three types of motion. The range is very limited for heaving motion, while the range is very similar for both pitching and coupled motions but the transition to

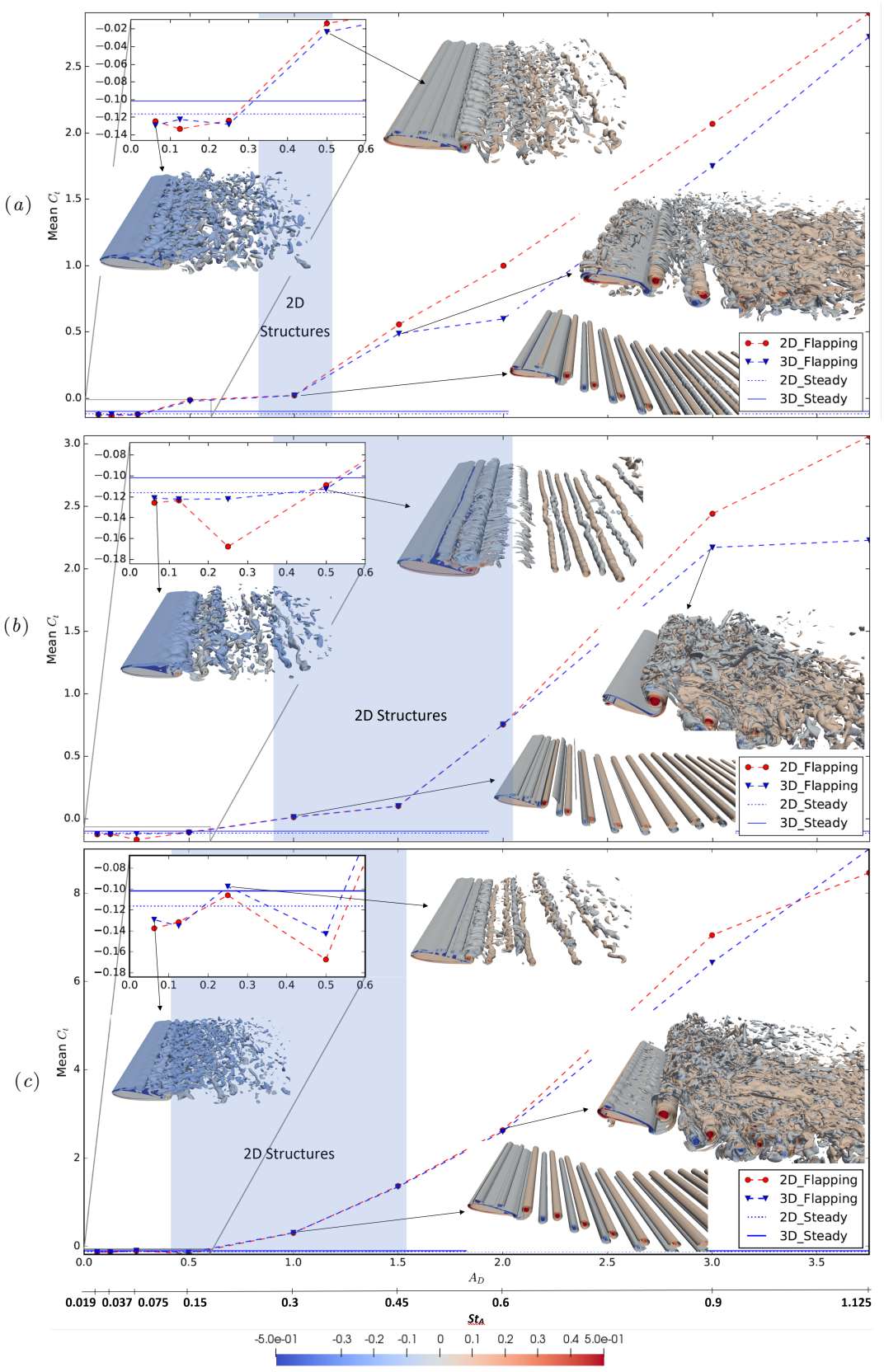

FIGURE 3.3: 3D iso-surfaces of ω_z on mean thrust-coefficient $\overline{C_T}$ versus trailing-edge amplitude A_D graph showing structure transitions at (a) heaving, (b) and pitching (c) coupled motions. Shaded areas locate 2D structures and non-shaded for 3D structures. Complete wakes can be viewed in Appendix B

3D is earlier for the coupled motion. The similarity between pitching and coupled motion is understandable as the coupled motion is dominated by pitch motion in these current simulations. A heave dominant coupled motion would lead to the breakdown of 2D structures earlier and the range would be more similar to heaving-only motions.

3.3.2 Effect of spanwise domain size

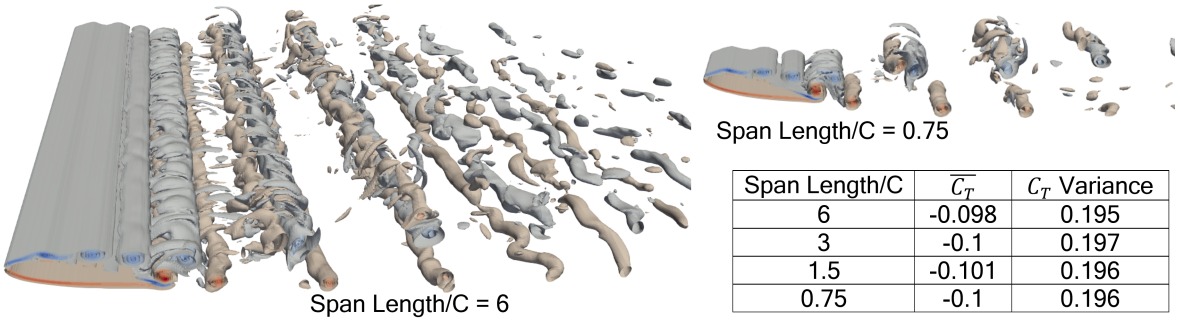

Span Length/C	$\overline{C_T}$	C_T Variance
6	-0.098	0.195
3	-0.1	0.197
1.5	-0.101	0.196
0.75	-0.1	0.196

FIGURE 3.4: Convergence of $\overline{C_T}$ and C_T variance with reduction in spanwise domain.

In order to isolate the effect of spanwise domain size of the 3D simulations on the above observed results, a series of simulations with different spanwise lengths were carried out. All the simulations were confined at one kinematics: coupled motion at $A_D = 0.25$ where 3D structures begin to re-organise into 2D structures. Figure 3.4 shows that even when the span is reduced at $0.75C$, the $\overline{C_T}$ and C_T variance are almost constant and the 3D structures remain significant. This signifies the importance of the three-dimensionality of the spanwise vortices. This also suggests that a small spanwise domain length might be sufficient to capture the 3D effects provided the kinematics are in a certain range of amplitudes and frequencies.

3.3.3 Statistics of thrust coefficient

Along with the appearance of uniform 2D structures, the statistics of force coefficients (C_T and C_L) i.e. average, maximum, minimum and variance are similar for both 2D and 3D simulations. At lower and higher A_D when 3D structures appear, the force coefficients in 2D simulation exhibit very high levels of fluctuations. Similar force-coefficient fluctuations are shown for 2D simulation by Taira & Colonius (2009) for stationary flat-plates at a higher angle of attack.

Figure 3.5 presents the comparison of C_T evolution for both 2D and 3D simulation for pitching motion. The tendency of C_T evolution for heaving and coupled motion are similar (not presented here for brevity). It can be seen that the 2D simulations exhibit cycle-to-cycle variations at lower and higher A_D while these variations are minimal for the intermediate amplitude. The cycle-to-cycle variations for the 3D simulations are weaker and only apparent for the low amplitude case. It was also found that both 2D and 3D simulations converged faster for the intermediate amplitude since the variations in the flow and the forces are minimal.

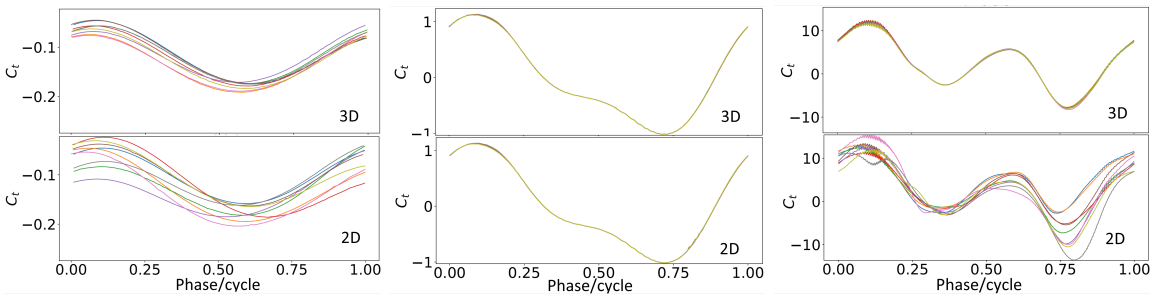

FIGURE 3.5: C_T comparison between 2D and 3D simulations of pitching motion for ten-cycles at (a) $A_D = 0.0625$, (b) $A_D = 1$ and (c) $A_D = 3.75$.

3.3.4 Spanwise vorticity

The instantaneous ω_z and the phase-averaged ω_z for 2D and 3D simulations are compared in Figure 3.6. For the 3D simulations, the vorticity is first spanwise-averaged prior to comparing it with 2D simulations. The presented figures are the cases where 3D structures appear at the lowest and the highest A_D in coupled motion. These are representative and similar features are observed in other kinematics as well.

As seen in figure 3.6(a) for a flapping amplitude of $A_D = 3.75$, the instantaneous cases for 2D and 3D simulations differ mainly in the wakes. The wakes in 2D simulation appear to be aperiodic and perhaps more chaotic. Meanwhile, the span-averaged vorticity in 3D simulations appears "cleaner" and more converged, making phase-averaging easier. This is because, in 3D simulations, the effect of spanwise averaging eliminates small perturbations in ω_z structure. However, in 2D simulations, this is not possible. Any small variation is exacerbated since there is no smoothing process and leads to the appearance of a chaotic wake.

In phase-averaged coupled motion (similar to other kinematics), the LEVs appear to be slightly smaller for 2D simulations compared to 3D simulations due to "jitter" in the position of these vortices over different cycles. On the other hand, both types of simulations preserve one vortex pair behind the trailing edge. In the "far" wake, 2D simulations are chaotic since the vortices are strong and their self-induced motions alter the trajectories of the wake. Moreover, there are no mechanisms that can reduce the strength of these vortices (other than viscosity) and therefore they remain strong for an extended length/time. For the 3D simulations, the spanwise length provides a route for the transport of vorticity from the vortex core, thereby weakening the wakes downstream.

At the lowest A_D in figure 3.6(b), the difference between 2D and 3D simulations are not only in the wakes but also in the separation and recirculation areas. Similar to high A_D, the wakes for instantaneous 3D simulation have the spanwise direction to transport/diffuse vorticity compared to 2D simulations. Nonetheless, the wake widths of phase-averaged 2D and 3D simulations are similar. This perhaps explains why the difference in values of $\overline{C_T}$ in 2D and 3D simulations at lower A_D is relatively small. At lower A_D, the LEVs in both

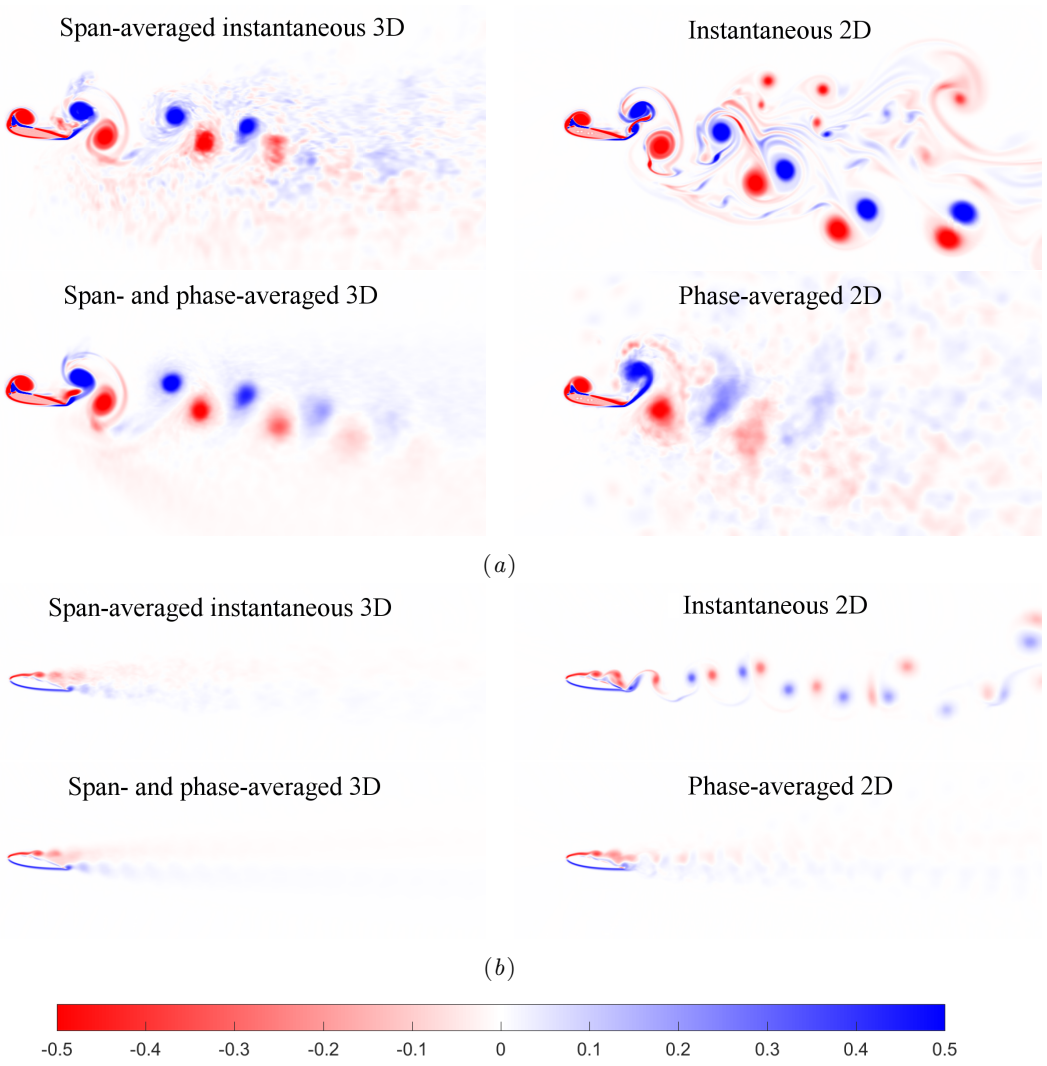

FIGURE 3.6: Instantaneous and phase averaged ω_z for coupled motion at (a) $A_D = 3.75$ and (b) $A_D = 0.0625$. The 3D simulations have been span-averaged prior to phase-average.

2D and 3D simulations look similar but the trailing-edge vortices (TEVs) are different due to recirculation and flow inside the separation region. The vortices in 2D simulations at the separation region oscillate back and forth, while in 3D simulations they are more stable. This oscillation appears at a lower frequency than the shedding frequency, which explains the appearance of additional low-frequency energy content in 2D simulation (see next section).

3.3.5 Fourier analysis of force time-histories

The power spectral density for the thrust coefficient time history is computed and plotted against frequencies normalised by the flapping frequency in figure 3.7(a). The peak frequency at $\tilde{f} = 1$ shows the flapping frequency. The ordinate is pre-multiplied by the frequency and presented in linear scale to ensure that equal areas under the curve represent equal "energy". The term energy here is used to represent the strength of the fluctuations in the signal. In fact, it should be noted that the total area under the curve is equal to the variance of C_T

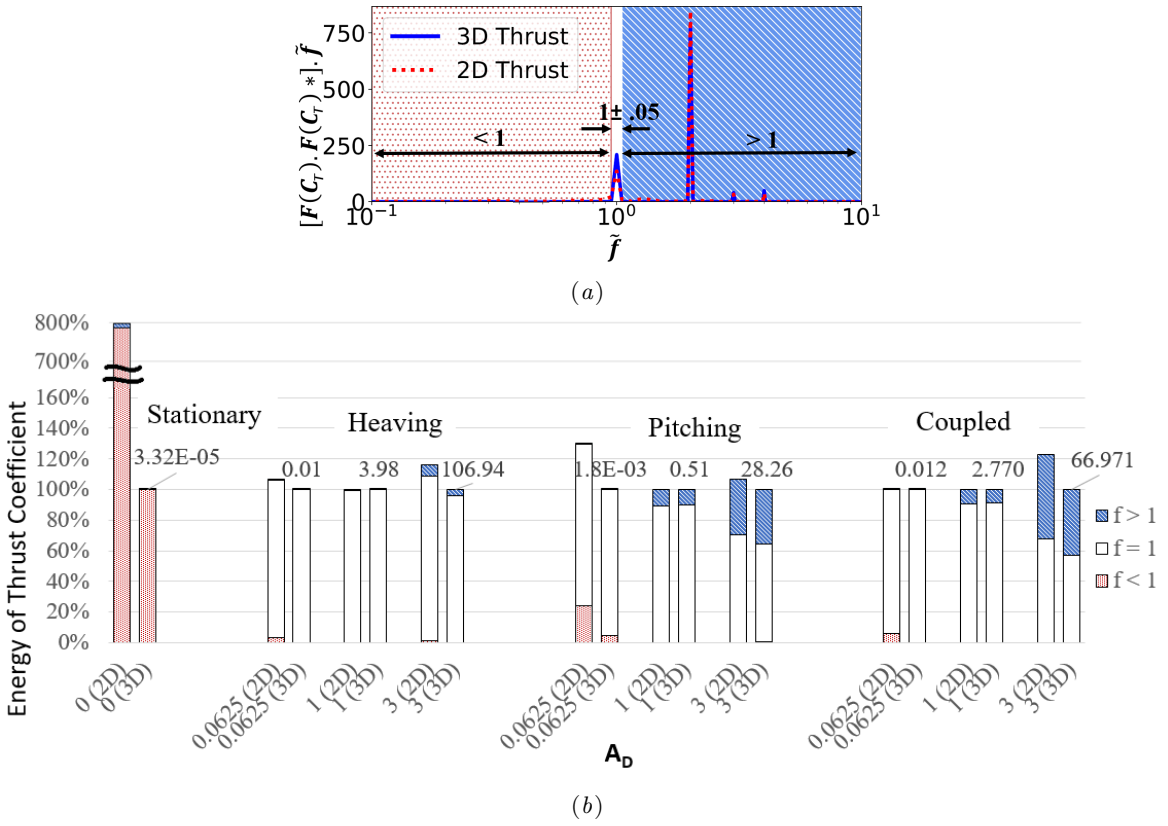

FIGURE 3.7: (*a*) Category division for C_T power spectra versus frequency (normalised to flapping frequency), and (*b*) C_T power-spectra integral or variance in percentage for 3 different $A_D s$. Each 3D-bar is scaled as 100% with its total variance on top, provided with the category divisions and accompanied by 2D on its left scaled as a percentage corresponding to the 3D.

signal. Furthermore, the fluctuations can be categorised into three main regimes: $\tilde{f} < 1$ (low frequency), $\tilde{f} = 1$ (exactly at the flapping frequency) and $\tilde{f} > 1$ (high frequency). The integral of the area under the curve within these regimes provide the contributions from each of these regimes to the overall fluctuations.

Figure 3.7(b) shows a bar chart that compares the energy in force fluctuations from 2D simulations to their 3D counterparts. The total variance from the 3D simulations is taken as the reference to calculate percentages and this numerical value is indicated at the top of the bars. Consequently, the bars for the 2D simulations are sometimes higher than 100% since the variance in 2D is higher than 3D simulations. The contributions of three regimes to these fluctuations are shown in three colours as marked in figure 3.7(a). Different bars are shown for different kinematics and flapping amplitudes. Two bars on the left are also shown for the stationary foil where the total energy of 2D simulation is 8 times higher than the 3D value. However, the absolute values of these fluctuations are orders of magnitude smaller than the flapping motions as seen from the numerical value on the top of the bars.

It is clear from figure 3.7 that the appearance of coherent 2D structures is accompanied by a very similar distribution of fluctuations in the three different regimes in 2D and 3D simulations. Meanwhile, the appearance of 3D structures (spanwise variations) is accompanied

by the discrepancy of force-fluctuation variance between 2D and 3D simulations where 2D simulation tends to exaggerate the levels of force fluctuations. Pitching has the lowest total energy among the three types of motion due to the nature of its kinematics, while pure heaving motion produces the largest levels of fluctuations. Meanwhile, coupled motion energy is slightly lower than heaving because of 90° phase-lag between pitching and heaving parts of the motion.

The vortex shedding frequency of a stationary foil also appears in the flapping foil (as a low frequency) and can be seen to contribute to force fluctuations for low values of A_D. However, 2D simulations exhibit other additional low frequencies, which is stems from cycle-to-cycle variations as discussed in the previous section. As A_D increases, the energy from kinematics far exceeds the energy from vortex shedding. This explains the transition from 3D to 2D uniform structures. The energy from kinematics arranges the flow structures into uniform, reattaching separation zone so that the vortices move consistently from the leading-edge until detachment at the trailing-edge, leading to more organised downstream wakes. At higher values of A_D, higher harmonic frequencies start to appear and these make a contribution to the force fluctuations. The contributions from these higher frequencies are significantly higher in 2D simulations compared to 3D simulations since there are additional higher frequencies due to the appearance/movement of chaotic vortices as seen in figure 3.6 and figure 3.5.

It is seen that coupled and pitching motions have large contributions (over 20%) from $\tilde{f} > 1$ at high values of A_D. The relative contributions are small for heave motions, however, since the absolute value of fluctuations in heave motions are much higher than other kinematics (as seen by the numerical value at the top), the absolute value from $\tilde{f} > 1$ is very comparable across different kinematics. This suggests that there could be a universal mechanism that leads to higher frequency force fluctuations regardless of kinematics. This mechanism could be related to the breakdown of the leading-edge vortices along the spanwise direction. This is further explored below.

3.3.6 Breakdown of LEVs

The transition from 2D back to 3D with increasing A_D is expected to be due to spanwise instability that leads to the breakdown of the vortices. As they grow in strength, vortices burst and form non-uniform small structures along the span. This breakdown appears to be at different values of A_D for different kinematics. This can be examined by calculating the circulation of the leading-edge vortex for different values of A_D and different kinematics. Figure 3.8 shows the variation in the circulation of LEVs, now represented as a Reynolds number (with $Re = \Gamma/\nu$). This circulation is calculated as the integral of vorticity over a box as shown in the inset in figure 3.8. This box was chosen at a given phase where a vortex is just shed from the leading-edge separation bubble. Since the frequency of flapping is the same for all simulations, the location and size of this box did not have to change across the different kinematics. The sensitivities for box sizes and locations are provided in figure 3.9 showing that Γ is robustly estimated as long as the integration region encloses the LEV pinch-off

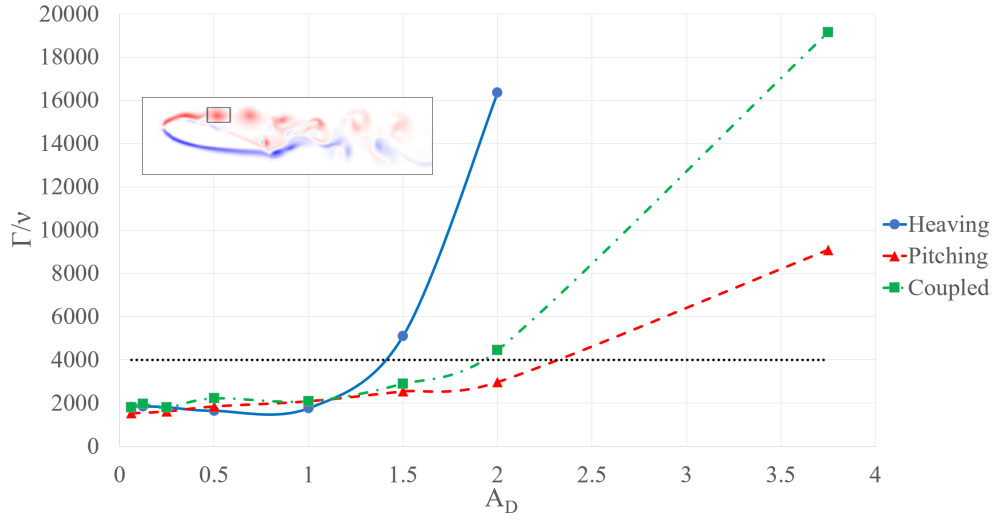

FIGURE 3.8: Evolution of leading-edge vortex circulation over kinematic viscosity along the increase of A_D. The flow above dotted black line show 3D structures.

location. Finally, a comparison of the circulation between 2D and 3D simulations did not reveal any noticeable difference before the vortices start to breakdown. This is because we are examining the "first" vortex that is shed, which are very similar regardless of the case.

The figure indicates that Reynolds numbers (or the circulation) of the LEVs appear to grow exponentially with increasing A_D. The rate of increase is different for different kinematics. The growth in heaving is the fastest among the three types of motion indicated why it has the shortest range of Strouhal numbers with 2D structures. In comparison, pitching and coupled motions have a more gradual growth leading to wider ranges for the presence of 2D structures. It should be noted that the coupled motion is dominated by pitching and therefore resembles the pitching kinematics.

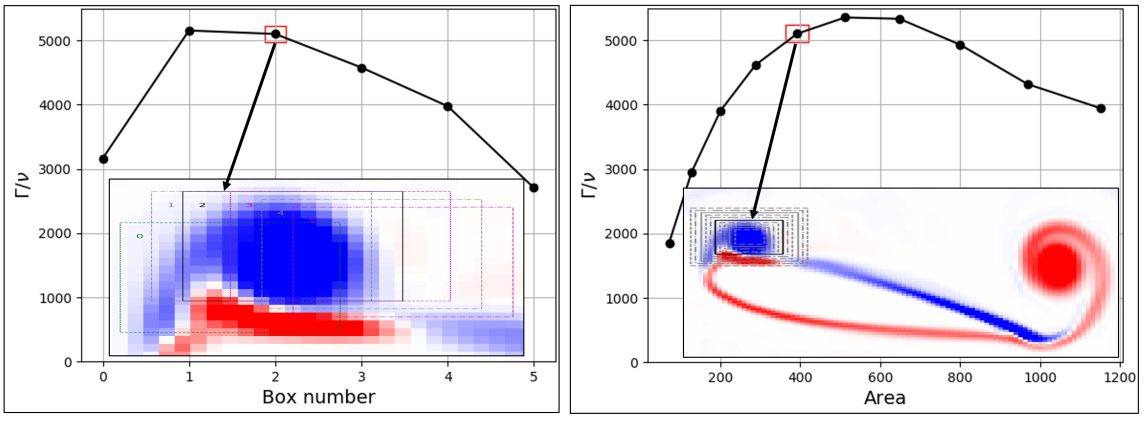

(a) (b)

FIGURE 3.9: Sensitivity analysis for heaving at $A_D = 1.5$ (*a*) box locations and (*b*) box sizes. The highlighted box size and location were chosen for the study and the results are shown in figure 3.8.

The horizontal dotted black line in figure 3.8 indicates the circulation of the LEVs where uniforms 2D structures transition to 3D structures. The cases where the circulation of LEVs

are higher than this value show vortex breakdown and smaller-scale structures accompanied by force fluctuations in higher frequencies. This is universally true regardless of the kinematics. This circulation or Reynolds number of LEVs, $\Gamma/\nu \approx 4000$ is the critical Reynolds number where the balance between vortex strength (induced by the kinematics) and viscous diffusion is lost leading to vortex breakdown. This critical Reynolds number is akin to the Reynolds number of a cylinder where there is a spanwise breakdown of vortices. However, for that case, the Reynolds number based on the cylinder diameter is much smaller than 4000. Regardless, the mechanism for the transition from 2D to 3D type flow structures appears to be similar. In conclusion, this critical LEV Reynolds number is valid for any kinematics and freestream Reynolds number but not for different geometry due to the bluff-body drag effect.

3.4 Conclusion

This work demonstrates that spanwise-uniform 2D structures are discovered at intermediate St_A of flapping foil, while strong 3D structures are found at higher and lower St_A. These 3D structures are produced over the span without being initiated by tip effect. In the intermediate St_A region with spanwise-uniform (2D) structures, all statistics of force coefficients (lift and drag) such as mean, maximum and variance are similar between 2D and 3D simulations. These 2D structures are found at $St_A \approx 0.3$ in heaving motion, $St_A \approx 0.3$–0.6 in pitching and $St_A \approx 0.15$–0.45 in coupled motion. Critically, the coupled motion gives a sufficient range for 2D structures to cover the optimal-efficiency St_A region for swimming animals mentioned by Triantafyllou et al. (1993), proving that 2D simulations are valid in this region.

In the regions where 3D vortex structures appear at higher and lower St_A, we discover discrepancy of mean force-coefficients between 2D and 3D simulations and over-prediction in 2D-simulation variances. The appearance of 3D structures at lower St_A is accompanied by more stable LEVs and discrepancies in the separation and recirculation areas. Meanwhile, the flow field of 2D simulation at higher St_A indicates non-dissipative vortices causing high force fluctuations and disturbance in the wake trajectories, LEVs and TEVs.

By analysing the variance of thrust-coefficient signals, we conclude that the transition from 3D to 2D vortex wake at intermediate St_A is due to the kinematics overwhelming the stationary foil's 3D drag wake. This is supported by the fact that the transition occurs at the same amplitude as the occurrence of reverse Bénard-von-Kármán propulsive wakes. Meanwhile, the 2D-to-3D transition from intermediate to higher St_A is due to high-energy LEVs overpowering the damping effect of viscosity causing the LEVs breakdown at $\Gamma/\nu \approx 4000$.

The application of strip theory may still be valid but only at the range of St_A where the flow structures are uniformly 2D. Outside of this, the validity is questionable signifying that the strip theory should not be applied at high St_A or low St_A. The 2D-structure window is found relatively wider in pitch-dominating motion. For manoeuvring and taking off flying, where heaving motion is significant and normally at higher St_A, 3D simulations are necessary regardless of the effect of tip vortices. In the future, this research will be continued using 3D

shape (including tip effect) and 3D motion (rolling and twisting motions) to comprehensively study the application of strip theory to finite flapping foils.

Chapter 4 Effects of aspect ratio on rolling and twisting foils

Abstract

Flapping flight and swimming are increasingly studied both due to their intrinsic scientific richness and their applicability to novel robotic systems. Strip theory is often applied to flapping wings, but such modeling is only rigorously applicable in the limit of infinite aspect ratio ($\mathcal{AR}$) where the geometry and kinematics are effectively uniform. This work compares the flow features and forces of strip theory and three dimensional flapping foils, maintaining similitude in the rolling and twisting kinematics while varying the foil $\mathcal{AR}$. We find the key influence of finite $\mathcal{AR}$ and spanwise varying kinematics is the generation of a time-periodic spanwise flow which stabilizes the vortex structures and enhances the dynamics at the foil root. An aspect-ratio correction for flapping foils is developed analogous to Prandtl finite wing theory, enabling future use of strip theory in analysis and design of finite aspect ratio flapping foils.

4.1 Introduction

Biologically inspired robotic systems offer benefits in their flexibility, maneuverability, energy savings, and speed. However, development of bio-inspired micro air vehicles (MAVs) and autonomous underwater vehicles (AUVs) requires a detailed understanding of unsteady three-dimensional fluid mechanics of propulsive flapping at intermediate Reynolds-number ($Re \approx 1000 - 10000$). Because of the cost and complexity of three-dimensional (3D) simulations, most propulsive flapping studies are conducted using a strip theory approach which assumes a simplified two-dimensional (2D) flow across the wing sections. However, this approach can lead to poor engineering predictions for the forces and efficiency due to the inherently 3D nature of the geometry, motion, and flow structures (Mittal & Balachandar 1995).

The key 3D fluid dynamic effects on a finite flapping foil undergoing 3D motion are spanwise flow, tip vortices, and 3D instabilities of the vortex wake. Spanwise flow promotes the fluid

dynamic interaction between sections of the wing which can result in high lift generation (Hong & Altman 2008, Ellington et al. 1996, Maxworthy 2007). The exact mechanism of this high lift on bird or insect wings is still highly debated between the spanwise flow (Ellington et al. 1996, Wong et al. 2017, Eldredge & Jones 2019) and downwash-induced flow caused by the tip (Lentink & Dickinson 2009, Birch & Dickinson 2001, Lu & Shen 2008). In addition, the tip of a finite foil definitely produces non-planar wakes which have been shown to influence stall on an impulsively translated flat plates (Taira & Colonius 2009), pitching flat plates (Hartloper & Rival 2013), revolving wings (Harbig et al. 2013, Jardin 2017, Kim & Gharib 2010, Garmann & Visbal 2014) and a finite foil undergoing 2D kinematics (Dong et al. 2005). Finally, even on an infinite wing with no tip effect or mean spanwise flow, 3D evolution of the vortex wake limits strip theory applications. Zurman-Nasution et al. (2020) showed there is only exist a narrow band of kinematics, for instance at Strouhal number $\approx 0.15 - 0.45$ for heaving-pitching motion, where the wake remains two-dimensional and 2D force predictions are accurate. In this 2D range, the motion of the foil stabilize the spanwise-perturbed 3D structures found in the separated wake of a stationary foil, but 3D structures reappear when the amplitude of motion increases the shed vortex circulation above a 2D viscous stability limit. This secondary instability along spanwise-aligned vortex tubes also causes the transition from 2D to 3D flow in circular cylinder wakes (Karniadakis & Triantafyllou 2006, Williamson 2006). Despite the importance of these effects, wake analysis for finite foils undergoing 3D kinematics is still rare because of the greatly reduced simulation cost when using 2D strip theory.

The key geometric parameter in the flow and forces on 3D flapping foil is the aspect ratio, $\mathcal{AR}$, defined as the square of total wing span length over the planform area. Chopra (2006) provided potential flow calculations indicating that decreasing $\mathcal{AR}$ would reduce thrust coefficient and efficiency. On the contrary, move recent experiments by Fu et al. (2015) show that the circulation over the tip velocity increases with $\mathcal{AR}$ but drops at $\mathcal{AR} = 4$, potentially explaining why many insects have low $\mathcal{AR}$ wings. These contradicting results show the need for simulations detailing the $\mathcal{AR}$ influence on the flow and forces of wings undergoing 3D kinematics. For a finite wing undergoing simple 2D pitching motion, pressure and thrust coefficient data are found to scale well with $1/(1+c'\mathcal{AR})$ where c' is a constant (Green & Smits 2008, Ayancik et al. 2019). This is similar to Prandtl finite wing theory although Smits (2019) emphasizes that this added mass scaling is somehow misleading because it neglects the circulatory forces. In addition, these studies and others such as (Calderon et al. 2013, Yilmaz & Rockwell 2011) which use purely 2D kinematics cannot study the contributions of 3D kinematics on the flow features and force scaling.

The ability to make 3D predictions from 2D simulations using analogous concepts to Prandtl's finite wing theory is an intriguing approach for speeding up computations, but it must be based on a strong understanding of the influence of $\mathcal{AR}$ on the unsteady 3D flow. In this work, we provide a detailed analysis using 3D simulations of rolling and twisting foils; a combination of 3D kinematics that imitates the natural flapping motion of animal's flippers (Clark & Bemis 1979, Davenport et al. 1997) but can also be directly mapped to simple

pitch and heave motion of each section. The addition of 3D twist to the foil kinematics also relates the current work to previous studies which indicate improved lift (Van Buren et al. 2018, Cleaver et al. 2014) and thrust coefficients (Cleaver et al. 2016, Barnes et al. 2013) for flexible foils. The instantaneous and phase-averaged vortex structures in the tip flow and wake, the spanwise flow along the foil, and the unsteady sectional forces on the foil are studied while aspect ratio is varied. Finally, we relate the sectional forces on the 3D foils to Prandtl finite-wing theory in order to scale the 2D strip theory force predictions onto 3D flapping wings.

4.2 Methodology

4.2.1 Geometry and kinematics

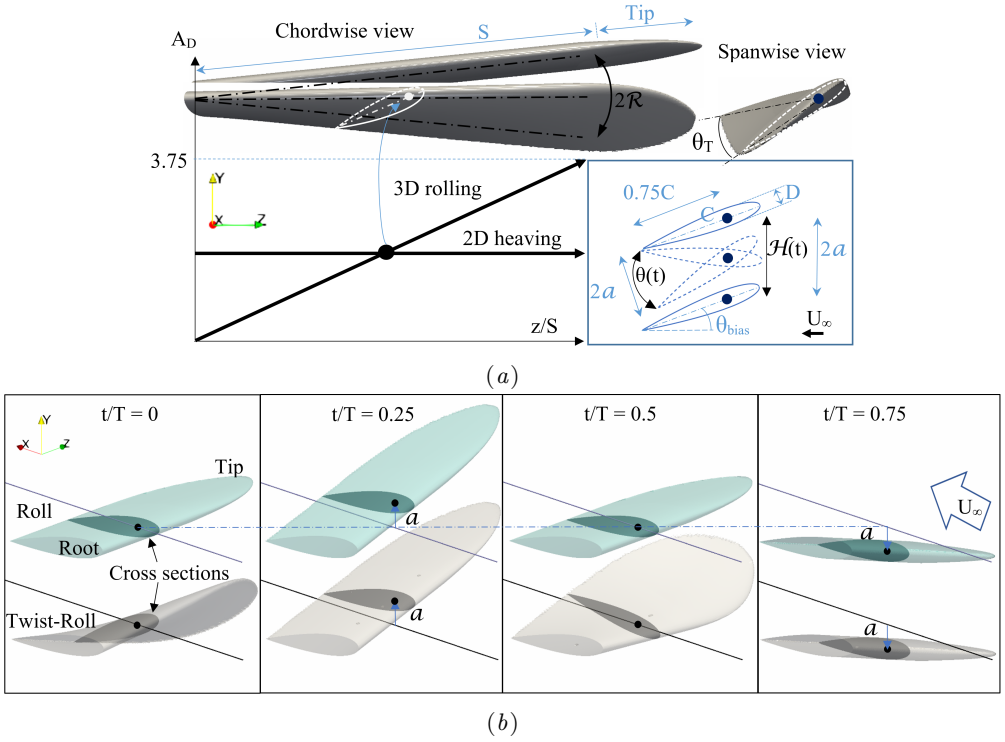

FIGURE 4.1: (a) Kinematic illustration for a 3D foil undergoing rolling and twisting motions whose cross sections are comparable to 2D foil experiencing linearly increased heave and pitch amplitude along the span. (b) Illustration of 4 phases in one cycle period (T) for pure rolling kinematic and twisting-rolling combination.

This study uses a NACA0016 foil with chord length C, thickness $D = 0.16C$, pivot point at $0.25C$ from the leading edge, a rectangular planform section with span length S, and a tapered elliptic tip with a length of $1C$ as shown in Figure 4.1. We will characterize the aspect ratio by S/C which is varied from $1 \ldots 6$. The foil is placed in a uniform flow with constant inflow speed U_∞ and a fluid density ρ and the chord-based Reynolds number $Re = U_\infty C/\nu = 5300$.

The 3D foil is prescribed to move in either pure roll or a combination of roll and twist, where roll is defined as rigid rotation around the streamwise axis x and twist is rotation around the spanwise axis z with linearly increasing amplitude towards the tip, Figure 4.1.

In a strip theory approach, these 3D kinematics are converted into 2D kinematics for each section along the span. The 2D sectional kinematics can be linearized for small amplitude roll to simple heave $\mathcal{H}(t)$ and pitch $\theta(t)$ motion in each spanwise plane, with functional form

$$\mathcal{H}(t) = a\sin(2\pi ft) \tag{4.1}$$

$$\theta(t) = \theta_0 \sin(2\pi ft + \psi) + \theta_{\text{bias}} \tag{4.2}$$

$$\theta_0 = \sin^{-1}\left(a/(0.75C)\right) \tag{4.3}$$

where f is the cycle frequency of flapping and a and θ_0 are the amplitudes of heave and pitch at each section. The term $\theta_{\text{bias}} = 10^\circ$ is a pitch bias angle used to ensure non-zero average mean lift as in Zurman-Nasution et al. (2020) and the phase difference is set to $\psi = 90^\circ$ to maximize performance (Isogai et al. 1999). In order to isolate the amplitude (which varies section by section) from the frequency, these motions are characterized as

$$St_D = \frac{Df}{U_\infty} \qquad A_D = \frac{2a}{D} \tag{4.4}$$

where St_D is the thickness-based Strouhal number, A_D is the thickness-based amplitude and in this work we fix $St_D = 0.3$. Combining these two gives the commonly used amplitude-based Strouhal number $St_A = St_D \cdot A_D$ (Triantafyllou et al. 1991) which is proportional to the maximum heave velocity on a section $\dot{\mathcal{H}}_{max} = 2\pi fa$ scaled by the incoming flow velocity.

Strip theory assumes that both the geometry and the motions change slowly along the span. The geometric constraint is unavoidably violated at the tip, but the kinematic condition is still a concern over the rectangular region of the planform. Slowly varying kinematics are contingent on large aspect ratio; a relationship that can be made explicit by noting that the pitch amplitude at each section is $\theta_0 = \theta_T z/S$ where θ_T is the twist amplitude at the foil tip, Figure 4.1. Therefore the scaled spanwise derivative of the 2D strip theory kinematics is $C\partial_z\theta_0 = \theta_T C/S$. The larger the aspect ratio, the smaller this derivative, and the better strip-theory should apply. Similarly, for small roll amplitude arc-length $\mathcal{R}$, the sectional heave amplitude is $a = \mathcal{R}z/S$ and therefore $\partial_z a = \mathcal{R}/S$. To focus on the aspect ratio effect, we prescribe a constant roll amplitude $\mathcal{R} = 0.3C$ from which all other amplitudes are determined.

Another way to measure the spanwise change in 2D kinematics along the foil, used recently by Wong et al. (2017), is the sectional angle-of-attack α

$$\alpha(t) = \tan^{-1}\left(\dot{\mathcal{H}}(t)/U_\infty\right) - \theta(t) \tag{4.5}$$

Because $\dot{\mathcal{H}}(t)$ increases towards the tip, so do the sectional angle-of-attack α and it's time derivative $\dot{\alpha}$. Figure 4.2 shows $\dot{\alpha}_{max}$ increases linearly along the span, while trigonometry causes the change in α_{max} to taper off near the tip. In either case, the spanwise derivative

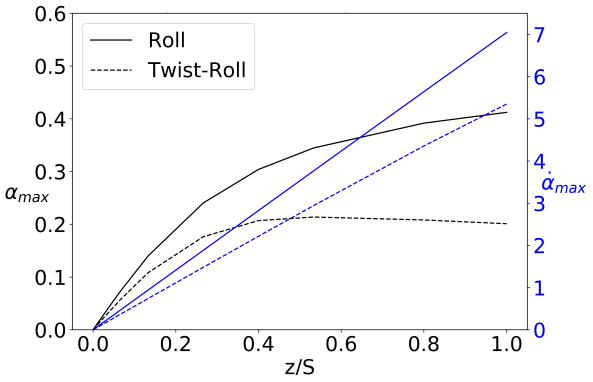

FIGURE 4.2: The gradient of maximum angle of attack α_{max} (π rad) towards the tip is positive with linear rate $\dot{\alpha}_{max}$ (π rad/t).

of these parameters depend inversely on S/C and we show they strongly impact the flow three-dimensionality.

4.2.2 Numerical methods

For computational consistency, the 2D and 3D simulations use the same solver. Symmetric conditions are enforced on both spanwise boundaries for the finite foil simulation. The domains extend from the pivot point to $4C$ at the front, $11C$ at the rear, $5.5C$ at the top and bottom. Meanwhile, the tip distance to maximum spanwise domain is $3.5C$. A grid convergence study with an infinite foil with span length of $3C$ and periodic spanwise boundary conditions and a 2D foil are used to verify the grid convergence for the lift and drag coefficients

$$C_L = \frac{F_y}{0.5\rho S_p U_\infty^2} \qquad C_D = \frac{F_x}{0.5\rho S_p U_\infty^2} \tag{4.6}$$

where F_x, F_y are the integrated fluid force in the global coordinate directions and $S_p = CS + \frac{\pi}{4}C^2$ is the foil planform area. Figure 2.2 in Section 2.2 shows the standard deviation of the forces predicted using $C/\Delta x = 128$ are within 3.3% of simulations with double the resolution in both 2D and 3D and this resolution is used for all results presented in this work. The error number presented is associated with mesh.

4.3 Results

In this section, we compare the flow-structure evolutions and forces of foil undergoing rolling and twisting-rolling motions over one cycle, across four aspect ratios.

4.3.1 Vortex structures

This section presents the qualitative features of the flow structures induced by the 3D kinematics on the finite foil. As a representative result, Figure 4.3 visualizes an instantaneous

snapshot of the turbulent vortex wake using λ_2 iso-contours colored by the spanwise vorticity $\omega_z C/U_\infty$ for an intermediate aspect ratio $S = 3C$ and for both 3D kinematics. The small turbulent structures indicating vortex breakdown are present for both kinematics. In order to focus on the most important aspects of the wake, the flow was phase-averaged at phases $t/T = 0, 1/4, 1/2, 3/4$. Figure 4.4 shows this simplifies the visualization, revealing the dominant structures which occur every cycle and removing higher frequency turbulent structures related to vortex breakdown. The pure roll and twist-roll cases have distinct vortex structures due to their different kinematics, but the periodic formation of the vortices such as the leading-edge (LEVs), trailing-edge (TEVs) and tip vortices are much more clear in the phase-averaged representation.

Both the instantaneous flow (Figure 4.3) and the phase-averaged flow (Figure 4.4) show strong three-dimensionality in their vortex structures along the span. Because the amplitude of motion increases linearly along the span, the sectional Strouhal St_A increases linearly as well. Starting from the root, we see the vortices are initially coherent and skewed obliquely, tilted further downstream as you progress towards the tip. This is especially clear in the near phase-averaged wake, where coherent structures persist all the way to the tip. Both the coherence and skew are in direct contrast to the complete 3D vortex breakdown found in the wake of infinite foils heaving and pitching with the same amplitudes (Zurman-Nasution et al. 2020), and therefore this must be due to the spanwise derivative of the kinematics not present in the infinite foil case. Indeed, the oblique near-wakes resembles the vortices of delta or swept wing and hints that the spanwise derivative of the kinematics induces a stabilizing spanwise flow —as found in swept wings and rotating foils at low revolution angles (Jardin 2017). For this finite foil, the far wake vortex structures break down into 3D non-periodic turbulence above section $z/S = 0.27$. This corresponds to a sectional $St_A = 0.3$ where 2D uniform structures were observed for both pure heaving and heaving-pitching combination for the infinite foil cases in Zurman-Nasution et al. (2020).

Contrasting the pure roll to the twist-roll case, we see that the tip vortex flow is much cleaner in the twist-roll case. The correspondence between the instantaneous and phase-averaged plots shows that the LEV vortex is essentially periodic near the foil, and does not breakdown until further downstream in the wake. This is due to the twist motion being out of phase with roll, reducing the angle of attack on the tip, Figure 4.2, and thereby reducing the strength of the tip vortices. This is further quantified in the next section. In contrast, the pure rolling TEV begins to breakdown as soon as it separates, see Figure 4.3. This also implies that the foil tip is more lightly loaded in the roll-twist case, reducing the lift forces that can be achieved at compared to rolling kinematics, as will be discussed further in the following sections.

4.3.2 Aspect-ratio effects

This section presents results on the influence of $\mathcal{AR}$ on the flow and forces. Figure 4.5 compares the instantaneous wake structures for $S = 3C$ and $S = 6C$ for a foil undergoing pure roll.

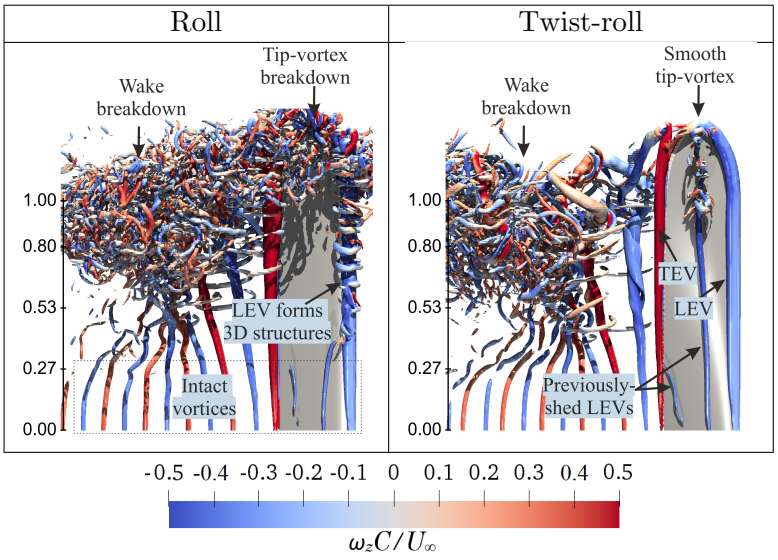

FIGURE 4.3: Instantaneous vortex wake visualization at $t/T = 0.5$ for both kinematics and $S = 3C$. Vortices are visualized with isocontours of λ_2 colored by dimensionless spanwise vorticity $\omega_z C/U_\infty$. Free-stream flow U_∞ is flowing right to left and spanwise scale given in z/S.

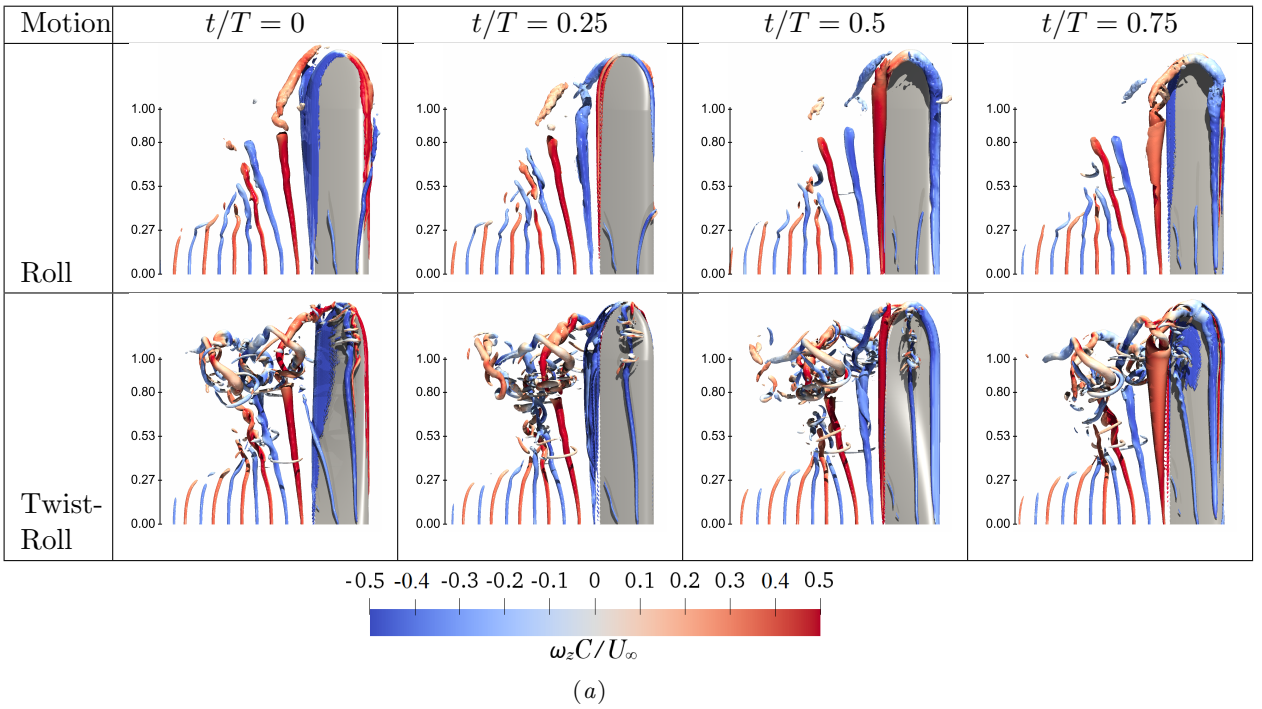

FIGURE 4.4: Phase-averaged velocities for pure rolling and twisting-rolling motions for $S = 3C$. Visualization as in Figure 4.3.

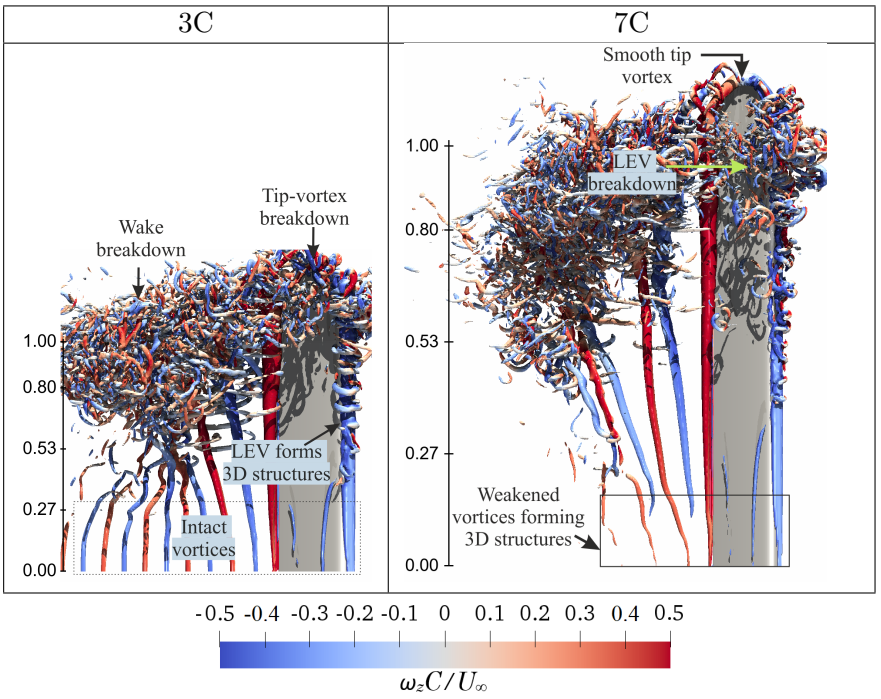

FIGURE 4.5: Instantaneous flow at $t/T = 0.5$ for finite foils undergoing the same pure roll kinematics. Labels contrast the relatively weaker wake vortices on the centerline ($z = 0$) and less turbulent tip flow on the $S = 6C$ foil compared to $S = 3C$. Visualization as in Figure 4.3.

Note that the 2D kinematics on each z/S slice match between these cases, e.g. $St_A = 0.3$ on $z/S = 0.27$ for both foils. Therefore the strip theory solution is identical for the two cases, while the 3D simulations show obvious important differences. Because the span is twice as long, the spanwise derivatives of the kinematic parameters $St_A, \alpha, \dot{\alpha}$ are half as strong, weakening the three-dimensionality of the flow. First, the turbulent tip flow and wake breakdown is less uniform in the $S = 6C$ case, with a few clean vortex structures identifiable over a longer span length. In addition, the center-line ($z = 0$) reversed Kármán vortex street is completely different between the $3C$ and $6C$ cases. As the foil is motionless at the centerline, these vortices would not even appear in a strip theory approach, and as they are far from the tip, they isolate the influence of the spanwise derivative of the kinematics on the 3D flow. Figure 4.5 shows that the $S = 6C$ foil allows characteristics of the infinite foil to appear, including very weak and 3D vortex structures in regions with very low amplitude (Zurman-Nasution et al. 2020). This area is dominated by the stationary foil vortex-shedding induced only by the bias angle of attack $\theta_{bias} = 10°$.

These effects are reiterated and quantified in Figure 4.6 which shows the phase-averaged flow across the full range of tested S/C. As before, the kinematics for each z/S slice match across the foil sizes. The plot also quantifies the viscosity scaled circulation of the tip vortices (Γ_x) and centerline vortices (Γ_z). The circulation is computed by integrating the phase-averaged vorticity over a rectangular slice through the vortex cores (see Fig.4.6 insets) and are kept the same size as span is varied, but not between Γ_z and Γ_x. The tip vortices are seen to dominate a larger portion of the flow as $\mathcal{R}$ is reduced, as expected. However, the relative

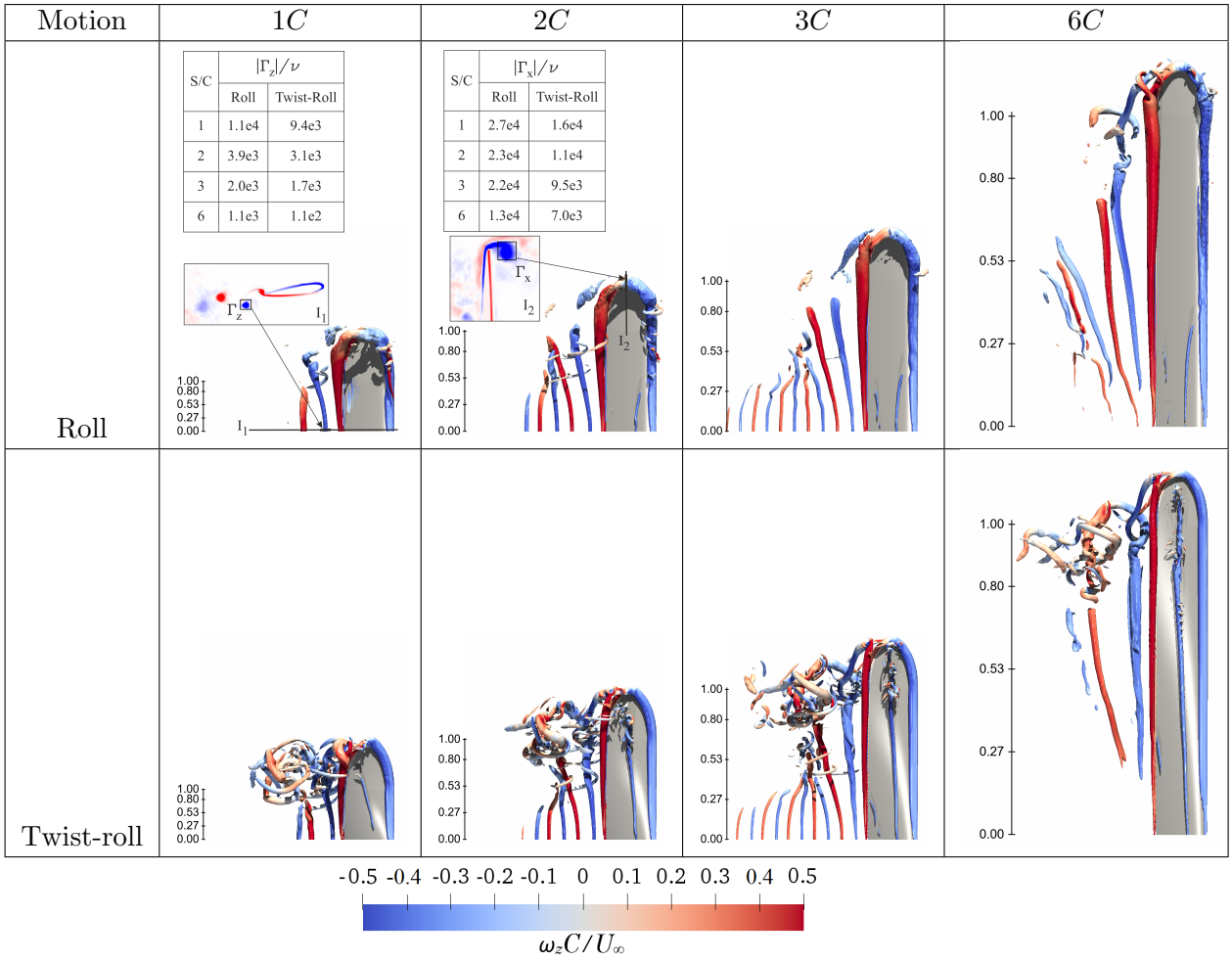

FIGURE 4.6: Phase-averaged flow for pure roll and twist-roll motions for different aspect ratios at $t/T = 0.5$. Flow visualization as inFigure 4.3. Inset figure I_1 shows the spanwise vorticity on a center-line slice and I_2 shows the streamwise vorticity on a slice through the tip. The inset tables give the viscosity-scaled circulation of the shed vortices.

strength of the tip vortices only grows by a factor of 2 as the span is reduced from $S = 6C$ to $S = C$ for either motion type. A much stronger effect is observed in the center-line ($z = 0$) circulation of the vortices in the reversed Kármán street. Fig.4.6 quantifies that these vortices strengthen by an order of magnitude when the span is reduced from $S = 6C$ to $S = C$ for the pure roll case, and nearly two orders of magnitude for the twist-roll case.

To further quantify the impact of $\mathcal{AR}$ on the flow, Figure 4.7 shows the phase-averaged pressure coefficient $C_p = P/(0.5\rho U_\infty^2)$ at three slices along the span for the twist-roll case. The roll case is similar and so not shown. We find that all $\mathcal{AR}$ produce a similar C_p distribution near the tip ($z/S = 1$), whereas the near-root pressure coefficient is substantially higher for lower aspect ratios. This is in agreement with the wake circulation findings and supports that the near-root sections are dominated by the spanwise derivative in the kinematics.

Finally, Figure 4.8 shows the phase-averaged lift coefficient C_L for all span lengths and both pure roll and twist-roll kinematics over a motion cycle. First, we note that the relative magnitude of the lift is substantially reduced when adding twist to the kinematics. This is

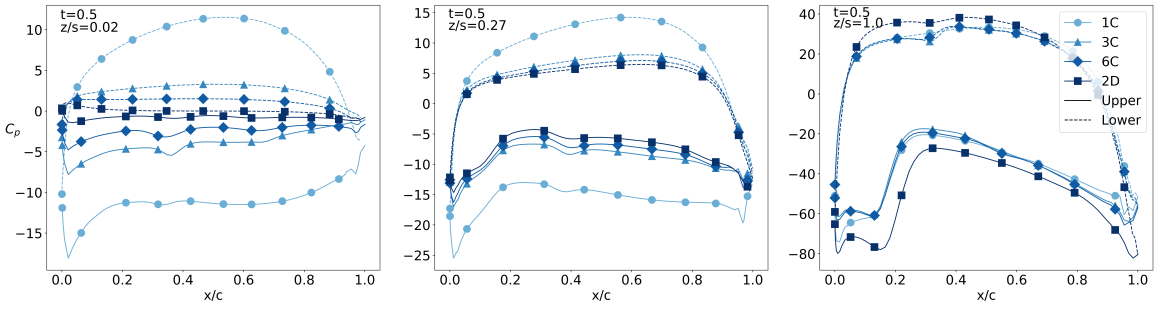

(a) (b) (c)

FIGURE 4.7: Phase-averaged pressure coefficient of twisting-rolling foil for cross sections $z/S =$ (a) 0.02, (b) 0.27 and (c) 1.0, at $t/T = 0.5$ for upper and lower side of the foil. Section close to tip is kinematic dominated, whereas the one close to root is gradient dominated.

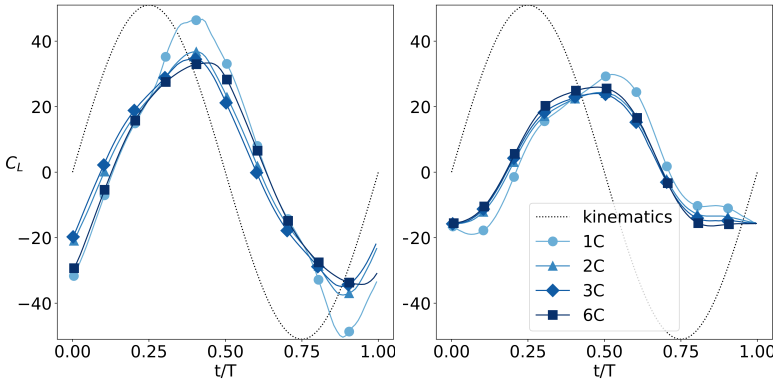

(a) (b)

FIGURE 4.8: Phase-averaged lift coefficient C_L evolution for various S/C of foil undergoing (a) roll and (b) twist-roll motions over one cycle.

because twist is out of phase with roll, reducing the angle of attack (Figure 4.2) and therefore unloading the foil. Comparing the results within each kinematic case, we can see that despite the large differences in the flow and the C_p distribution, the lift coefficients are quite similar.

A clear difference in the force response shown in Figure 4.8 is the large bumps in C_L on the shortest foil at around $t/T = 0.4, 0.9$ during roll and $t = 0.6, 0.1$ during twist-roll. These large lift forces are due to the LEV remaining near the foil longer, and thereby reducing the local pressure substantially.

4.3.3 Spanwise flow

The previous section shows that foils with the strongest spanwise derivatives in their kinematics have stronger three dimensionality which increases the strength of their wake vorticities and increases the stability of their LEV, both of which increase pressure forces. Previous work in revolving wings suggests that spanwise flow helps stabilize and keep LEVs attached by draining their vorticity outboard (Wong & Rival 2015, Jardin 2017) and we next investigate if spanwise flow is induced by the kinematic derivatives on 3D flapping wings.

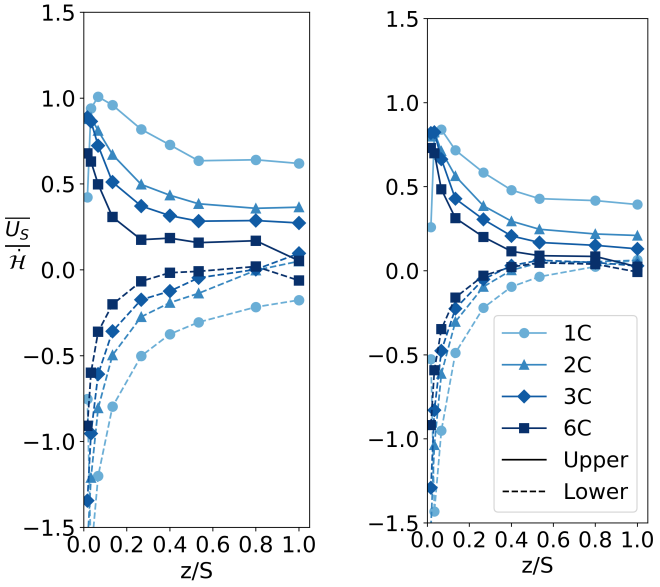

(*a*) (*b*)

FIGURE 4.9: Sectional spanwise velocity normalized by the heave velocity at each z/S section for (a) roll, and (b) twist-roll at $t/T = 0.5$. Solid/dashed lines indicate flow on the upper/lower side of the foil. Positive values indicate flow towards the tip and vice versa.

We define the sectional spanwise flow velocity over the foil surface as $\overline{U_S}^{\pm} = \frac{1}{C}\int_0^C U_S(x^{\pm})dx$ where U_S is the flow velocity tangent to the foil surface and perpendicular to the free stream direction, x is the position on C, and $\pm$ represents either the velocity on the upper or lower surface of the section. Figure 4.9 plots this quantity scaled by the maximum sectional heave velocity $\dot{\mathcal{H}}_{max} \propto z/S$ at each section along the span.

The figure shows $\overline{U_S}$ is roughly proportional to $\dot{\mathcal{H}}_{max} \propto z/S$ from the mid span to the tip for both pure roll and twist-roll. As the span length increases (i.e. for higher $\mathcal{AR}$) this relatively flat region occurs earlier and the strength of the spanwise velocity decreases, both of which indicate a more 2D flow. Close to the root, both the heave velocity and spanwise velocity go to zero by symmetry, but their ratio is finite and ~ 1 . Also note the strength of the spanwise velocity for twist-roll is smaller than for pure roll due to relative decrease in the kinematic derivative in that case. The drop in spanwise velocity for $S = 6C$ at $z = S$ shown in Figure 4.9 marks the location of strong vortex breakdown in Figure 4.5 and indicates that the small spanwise derivative of the kinematics for this large aspect ratio case is not sufficient to overcome the spanwise vortex instabilities found on an infinite foil (Zurman-Nasution et al. 2020).

4.4 Discussion

The spanwise derivative in the 3D flapping foil kinematics has been shown to induce a spanwise flow of proportional strength and this has a strong impact on the flow field. This

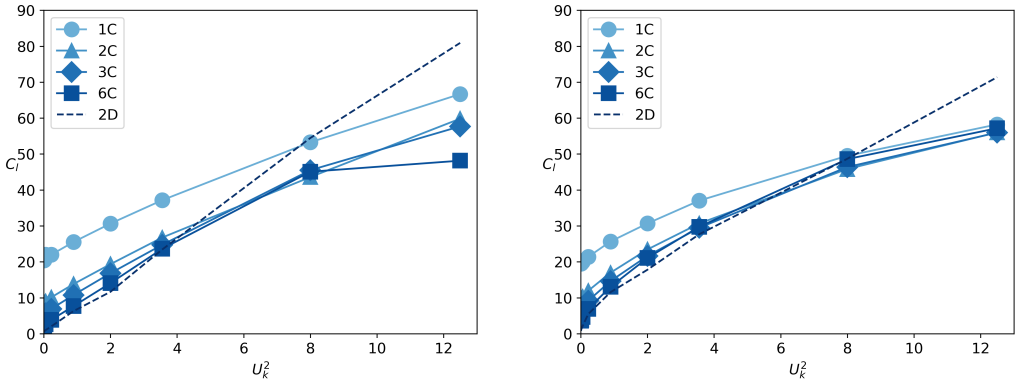

FIGURE 4.10: Peak sectional lift coefficients against $U_k^2 = \dot{\mathcal{H}}_{max}^2/U_\infty^2$ for (a) roll and (b) twist-roll kinematics for 3D foils of different spans. Strip theory results from 2D foils with the same kinematics are also shown.

TABLE 4.1: 3D slope (a_{3D}) change based on aspect-ratio compared to a_{2D} for $t/T = 0.5$. The slopes are measured using best-fit linear trend lines to the peak sectional lift from the root up to $z/S = 0.8$. Data from $t/T = 0$ produce the same trend (not presented here).

		Roll at $t/T = 0.5$, $a_{2D} = 6.52$			Twist-roll at $t/T = 0.5$, $a_{2D} = 5.55$		
s/c	AR_{eff}	$a_{3D}(pred)$	$a_{3D}(sim)$	$\lvert\epsilon\rvert$ (%)	$a_{3D}(pred)$	$a_{3D}(sim)$	$\lvert\epsilon\rvert$ (%)
6	7.2	5.07	4.06	24.8	4.46	4.47	0.2
3	4.2	4.37	4.37	0.2	3.92	4.10	4.4
2	3.2	3.97	4.13	3.9	3.59	3.81	5.9
1	2.2	3.38	3.74	9.5	3.10	3.18	2.5

spanwise flow overwhelms the documented behaviour of flapping infinite foils where the vortex strength is proportional to the scaled kinematic velocity St_A, and vortex instabilities leading to 3D structures are found at both very low and high St_A (Zurman-Nasution et al. 2020). On a finite wing undergoing 3D kinematics, the spanwise flow helps distribute vorticity along the span, greatly increasing the strength of the vortices at the root and increasing the LEV stability for foils with short spans. Only the longest span length $S = 6C$ shows similar behavior to infinite foils since the spanwise derivatives and spanwise flow are small. Nominally these values will falls to zero as the span length grows infinitely. Even for $S = 6C$ the vortex structures are generally 3D and it is only safe to apply 2D strip theory to cross sections experiencing medium Strouhal number $St_A \sim 0.3$.

However, the forces on the foil are much less sensitive to $\mathcal{AR}$ than the wake, implying that it could possible for a simple model to modify 2D strip-theory sectional forces to approximately predict 3D finite foil loading. Consider the sectional lift coefficient $C_l(z/S) = \oint C_p n_y ds/C$, where s is the 1D path around the z/S foil section, such that $C_L \propto \int_0^S C_l dz/S$. Figure 4.10 shows the peak C_l at each section along the span of the finite wings as well as from 2D simulations with the same sectional kinematics. Again, the kinematics at each value of z/S match for all 3D and 2D simulations, and so the strip theory predictions must be modified to represent finite wing sectional forces.

The unsteady Bernoulli equation suggests that the peak sectional lift should scale with the peak kinetic energy of the foil section, i.e. $\frac{1}{2}\rho\dot{\mathcal{H}}^2_{max}$. Figure 4.10 tests this scaling by plotting peak C_l against a normalized sectional kinetic energy $U_k^2 = (\dot{\mathcal{H}}_{max}/U_\infty)^2 \propto St_A^2$. We see that this scaling hold linearly for the 2D strip theory, and monotonically for the 3D sectional lift. Indeed, the slope of the peak sectional lift $a_{3D} = dC_L/d(U_k^2)$ changes with the aspect ratio, tending towards the strip theory slope as S/C increases. This lift-curve slope, a_{3D} can be determined using Prandtl's lifting line theory (Anderson 2017) as,

$$a_{3D} = \frac{a_{2D}}{1 + a_{2D}/\pi\mathcal{AR}} \tag{4.7}$$

where a_{2D} is the lift-curve slope of the 2D case. This finite-length correction developed for steady flow works surprisingly well to correct the peak sectional lift on flapping foils, Table 4.1. The only deviation greater than 10% is the $S = 6C$ roll case, where the lack of significant spanwise flow to stabilize the extremely strong tip vortices has greatly reduced the sectional lift on the end of the foil. In contrast, the corrected strip theory prediction have less than 6% error for all the 3D foils undergoing twist-roll case because of its more moderate loading.

In addition to the slope, the peak sectional C_l at the root ($z = 0$) also depends on S/C, as isolated in Figure 4.11. The forces for finite S/C fit a simple power law extremely well, tending to zero as S/C becomes large in agreement with the strip theory result. The constant multiplier of the power law depends on the foil shape and tip kinematics.

The scaling from 2D strip simulation with Equation 4.7 begins by providing peak sectional C_ls at the root for a relatively long S/C (infinite foil). The infinite flapping foil at very low St_A or at $A_D = 0.0625$ gives a peak $C_l = 1.4$ which coincides with the peak C_l value at $S/C = 10$ for a finite foil in Figure 4.11. The root peak C_l values in Figure 4.11 are extrapolated from $A_D = 0.0625$ for each of finite-foil cases but relatively close. Using infinite foil simulation at a very low A_D is more appropriate than the stationary infinite foil ($A_D = 0$). This is because the energy of a very small kinematic is far greater than the vortex-shedding energy of a stationary foil as shown in Figure 3.7. The difference in power-law equations for roll and twist-roll at higher S/C is relatively minor. Likewise, the total energy difference between the heave and coupled motions in Figure 3.7 (b) is very small which will not significantly contribute to the errors.

4.5 Conclusion

In this work, we analyze the vortex structures and force characteristics of foils with prescribed rolling and twisting kinematics. Using three-dimensional Navier-Stokes simulations and matched kinematics per cross-section, we study the influence of increasing $\mathcal{AR}$s up to an idealized infinite span and compare it with the strip theory (2D analysis). If the $\mathcal{AR}$ is

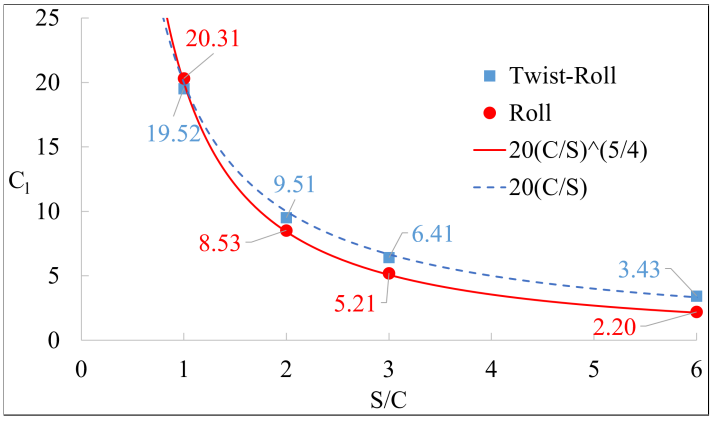

FIGURE 4.11: Peak sectional C_l at the root $z/S = 0$.

sufficiently long, the flow induced by a finite foil undergoing 3D kinematics shows characteristics of the infinite foil flow. However, this flow is still generally 3D and strip theory is only applicable to the sections experiencing Strouhal numbers with 2D characteristics $St_A \approx 0.3$ (Zurman-Nasution et al. 2020). By decreasing the $\mathcal{AR}$, the spanwise derivative in the applied kinematics increases, inducing a strong spanwise flow on both upper and lower sides of the foil (in opposite directions) which promotes flow interaction between the sections. The shortest aspect ratio ($S/C = 1$) therefore produces much stronger vortices, particularly at the root where they are 10-90 times stronger than the longest finite foil ($S/C = 6$) depending on the kinematics applied.

Overall, we find that adding a 90°-lag twist can reduce the vortex breakdown produced by pure rolling motion near the tip. Twist also delays the LEV detachment. It indicates that small chordwise flexibility towards the tip, as seen in the animal's flipper or bird's wing, likely promotes more stable vortex structures and possibly improved force production.

The forces on the finite wings are also sensitive to $\mathcal{AR}$, but the impact is less extreme than on the flow structures. We find the peak sectional C_l scales with local St_A^2, recognized as the added mass scaling (Garrick 1936, Van Buren et al. 2019), and this scaling becomes linear in the limit of infinite $\mathcal{AR}$. The slope $dC_l/d(St_A^2)$ surprisingly follows the Prandtl finite-wing trend, i.e. lower slope for low $\mathcal{AR}$ and vice versa. This aspect ratio scaling has been reported to fit the circulatory force by varying aspect ratios (Ayancik et al. 2019, Moored & Quinn 2019, Green & Smits 2008), but this scaling has not been previously used to scale 3D forces from 2D strips. We find strip theory predictions with an $\mathcal{AR}$ correction have error below 6% for a finite wing undergoing twist-roll motion, indicating it is possible to scale the sectional forces experienced by 3D foils based on results from 2D strips using a version of Prandtl finite-wing theory.

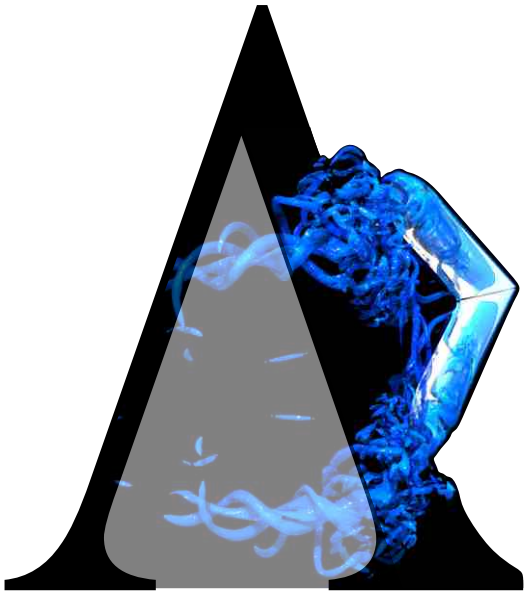

Chapter 5 Fin sweep angle does not determine flapping propulsive performance

Abstract

The importance of the leading-edge sweep angle of propulsive surfaces used by unsteady swimming and flying animals has been an issue of debate for many years, spurring studies in biology, engineering, and robotics with mixed conclusions. In this work we provide results from an extensive set of three-dimensional simulations of a finite foil undergoing tail-like (pitch-heave) and flipper-like (twist-roll) kinematics for a range of sweep angles while carefully controlling all other parameters. No significant change in force and power is observed for tail-like motions as the sweep angle increases, with a corresponding efficiency drop of only $\approx 2\%$. The same findings are seen in flipper-like motion although the efficiency decrease is slightly higher $\approx 13\%$ due to thrust reduction. This leads to a conclusion that fish tails or mammal flukes can have a large range of potential sweep angles without negative propulsive impact. A similar conclusion applies to flippers; although there is a slight benefit to avoid large sweep angles for flippers, this could be easily compensated by adjusting other hydrodynamics parameters such as flapping frequency, amplitude and maximum angle of attack to gain higher thrust and efficiency.

5.1 Introduction

A large fraction of swimming and flying animals use propulsive flapping to move, and there are significant potential applications for this biologically inspired locomotion in engineering and robotics. As such, significant research effort has been devoted towards understanding and optimizing both the kinematics and morphology of the propulsion surface itself, with a particular emphasis on explaining propulsive efficiency.

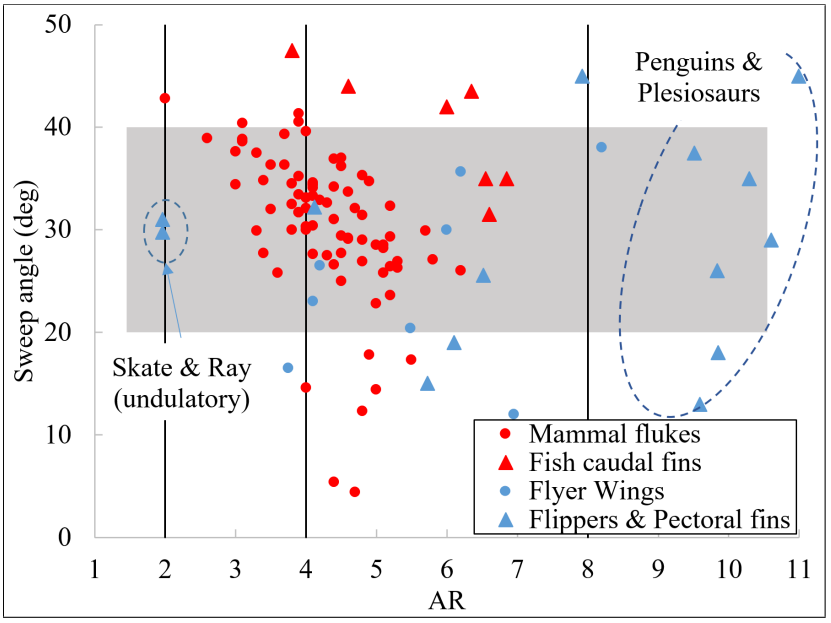

FIGURE 5.1: Collection of biologist data for sweep angles and aspect ratio $\mathcal{AR}$ for fish caudal fins and mammal flukes (in red) and flippers, pectoral fins, and wings (in blue) shows the extremely wide scatter across this evolutionary parameter space for different successful animals. The current computational study takes place over sweep angles from $20° - 40°$ (grey rectangle) and $\mathcal{AR} = 2, 4, 8$ to maximize the relevance to biological propulsive surfaces.

The leading edge sweptback angle is a key geometric feature observed in fish tails, mammal flukes, aquatic-animal flippers, bird and insect wings. There have been extensive studies collecting sweep back angle data from a variety of animal propulsion surfaces. The data in Figure 5.1 are collected from marine mammals (Fish & J. 1999), fish caudal fins (Magnuson 1978), flyer wings (Hubel et al. 2016, Von Busse et al. 2012, Klaassen van Oorschot et al. 2016, Willmott & Ellington 1997, Pennycuick 1968), and aquatic animal flippers and pectoral fins (Gurdek Bas et al. 2015, Fish & Battle 1995, Carpenter et al. 2010, Rivera et al. 2013, Sato et al. 2010, Russo et al. 2015, Astarloa et al. 2008, Rambahiniarison et al. 2016) (see Appendix C for detail). There is a strong correlation between fin aspect ratio, $\mathcal{AR}$, and kinematics. Undulatory motion (such as pectoral fins of skates and rays) are limited to the low $\mathcal{AR} \approx 2$ fins, while the highest $\mathcal{AR} \geq 8$ region is populated only by flippers and wings which performing rolling and twisting motions, such as penguins and most plesiosaurs. Most fish caudal fins, mammal flukes and many flippers and wing are found in the intermediate $\mathcal{AR}$ region. In contrast, the sweep angle Λ dependence is much less clear, with flippers and propulsive pectoral fins spanning a wide range of angles. While some individual studies indicate that increased sweep angles are correlated with animals with lower aspect ratios $\mathcal{AR}$ fins, there is extensive variation between animals within the groups and no strong trend is found when including all the groups using propulsive flapping. Additionally, there are hundreds of differences in the specific geometry and kinematics of each of these animals and just as many biological pressures other than propulsive efficiency at play, making it difficult to conclusively determine the influence of sweep angle from biological data directly.

Focused engineering studies have also been applied to determine the impact of sweep angle

on the performance of flapping propulsion surfaces. While these would hopefully clarify the issues at play, the findings are somewhat contradictory, especially between analytical and experimental analysis. Most analytical studies using lifting-line theory indicate sweep is advantageous, increasing the thrust and propulsive efficiency (Liu & Bose 1993, van Dam 1987, Chopra & Kambe 2006). While such methodologies are effective at determining lift characteristics on steady wings, they cannot model unsteady rotational three-dimensional flow, including the evolution of vortices that form at the fin's leading edge and tip which lead to the high forces observed in flapping foil propulsion (Liu et al. 2015, Zurman-Nasution et al. 2020).

While some experimental studies have measured a small flapping propulsive benefit to sweep, the effect is smaller than the analytic studies and other experiments have found no impact at all. A study on the spanwise flow caused by sweep angle found that it did not stabilize the LEV on an impulsively heaved foil (Beem et al. 2011), in contrast to the known stabilizing effect on a stationary wing. Another study reported affected forces and vortex strength on a 45°-sweptback flapping plate for relatively big LEV produced by an impulsively heaved plate Wong et al. (2013). Insignificant force change is also seen in the experiment of manta robot with rolling flexible flippers (Arastehfar et al. 2019). Varying sweep angle from zero to 60° in rotating wings were reported with no stabilized LEV (Lentink & Dickinson 2009). For pure pitching flat plate, the data of circulation time-histories show varying reduced frequencies can change the LEV circulation slightly more on the lower frequency cases (Onoue & Breuer 2017). This indicates that it is important to test a variety of kinematics relevant to the problem, as well as controlling for as many other parameters as possible, something which is very difficult to accomplish in physical experiments.

5.2 Methodology

In this work, we carefully isolate the effect of varied sweep angles from all other geometric parameters to help address the conflicting and scattered results of previous biological, analytical and experimental studies. Using 3D unsteady numerical simulations, we add sweep to a simple base geometry and test its flapping propulsive performance for two types of biologically inspired kinematics, i.e. tail-like and flipper-like motions, Figure 5.2(a). We also test the combined impact of $\mathcal{AR}$ and sweep as well as other kinematic parameters to determine the relative influence of sweep angle on propulsive flapping.

The prescribed form of the heaving $\mathcal{H}(t)$ and pitching $\theta(t)$ functions are given by

$$\mathcal{H}(t) = A\sin(2\pi ft) \tag{5.1}$$

$$\theta(t) = \theta_0 \sin(2\pi ft + \psi) \tag{5.2}$$

$$\theta_0 = \sin^{-1}(A/l^*) \tag{5.3}$$

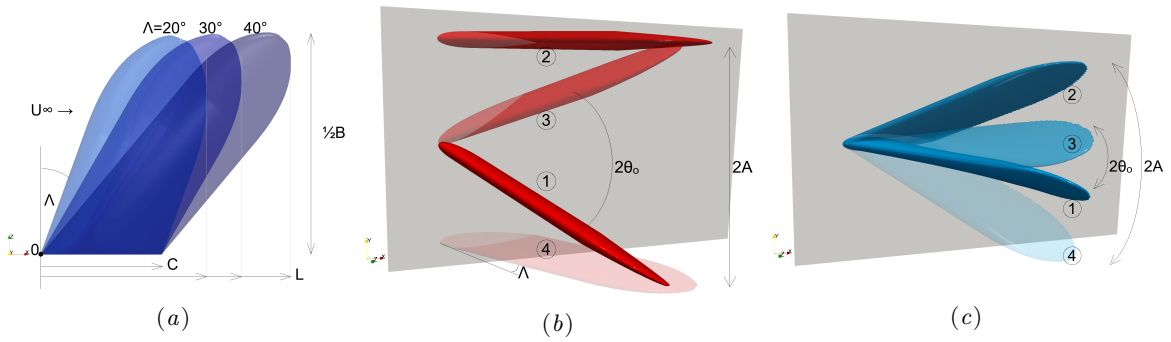

(a) (b) (c)

FIGURE 5.2: Diagram of the propulsive fin geometry and kinematics. (a) Foil planform with various sweep angle Λ for two different kinematic i.e. (b) fishtail-like kinematics i.e. pitch-heave combined with $\mathcal{AR} = 4$, and (c) flipper-like kinematics i.e. twist-roll combined with $\mathcal{AR} = 8$. Phase steps per cycle are denoted from ① to ④.

where θ_0 the trailing-edge tip rotation amplitude, and the phase difference $\psi = 90°$ are set based on the maximum performance for 2D motions (Isogai et al. 1999). The twist is defined equivalently to pitch, with the amplitude increasing with distance from the root section. The pivot point of pitch and twist is at the leading edge of the root section. The roll motion is simply rotation about the inline axis, and the amplitude is set to achieve the same amplitude A.

The correlation methods in Figure 5.7 (b) use widely known Pearson coefficient of correlation between two continuous sets of data, and correlation ratio between a category set and a continuous data set. A correlation ratio is defined as

$$\sqrt{\frac{\sum_x n_x(\overline{y}_x - \overline{y})^2}{\sum_{x,i}(y_{xi} - \overline{y})^2}} \tag{5.4}$$

where

$$\overline{y}_x = \frac{\sum_i y_{x,i}}{n_x}, \quad \overline{y} = \frac{\sum_x n_x \overline{y}_x}{\sum_x n_x}, \tag{5.5}$$

x category in each observation y_{xi}, i index, n_x the number of observation in category x, and $\overline{y}_x$ is the mean of category x.

Symmetric conditions are enforced on both spanwise boundaries for the finite foil simulation. The domains extend from the pivot point to $4C$ at the front, $11C$ at the rear, $5.5C$ at the top and bottom. Meanwhile, the tip distance to the maximum spanwise domain is $3.2C$. The grid convergence study provided in Figure 2.2 using an infinite foil with a span length of $6C$ in $Re = 5300$ as a comparison of time-averaged thrust coefficient for different resolutions. The zero-mean standard deviation for force coefficients converge to within 3.3% error of the finer mesh simulations (for 2D and 3D simulation) using a resolution of $C/\Delta x = 128$. As a balance between the grid resolution and the number of simulations, this resolution is deemed sufficient to captures the dynamics of the flow.

Specifically, we define our geometry to use a NACA0016 foil cross-section with chord length C, defined parallel to the inflow the U_∞, and thickness $D = 0.16C$. A rectangular planform

is combined with a tapered elliptic tip with a length of $1C$. The sweep angle Λ, defined in Figure 5.2, is varied from $\Lambda = [20°, 30°, 40°]$ to cover the most populated biological range, Figure 5.1. As the sweep is adjusted, the tip-to-tip foil span B is adjusted to maintain the desired aspect ratio $\mathit{AR} = B^2/S_p$, where S_p is the planform area. As with sweep, we use a wide range of AR =[2, 4, 8] to cover most propulsive surfaces found in nature. The chord-wise Reynolds number $Re = U_\infty C/\nu = 5300$, where ν is the fluid kinematic viscosity, is kept fixed to isolate the influence of the geometry and kinematics.

This geometry is subjected to sinusoidal "tail-like" and "flipper-like" motions diagrammed in Figure 5.2. The tail-like kinematics are inspired by measurements of fish caudal fins and mammal flukes and made up coupled heave and pitch motions, Fig 5.2(b). The flipper-like kinematics are inspired by aquatic animal pectoral flippers and bird/insect wings, and is made up twist and roll motions, Fig 5.2(c). These motions are quantified by Strouhal number $St = 2Af/U_\infty$ and reduced frequency $k^* = fl^*/U_\infty$, where f is the motion frequency, $2A$ is the total perpendicular amplitude envelope for the motion, and l^* is a length-scale equal to the total inline extent L for tail-like motions and $B/2$ for flipper-like motions. The majority of the simulations use a fairly low frequency $k^* = 0.3$ and high amplitude $2A = l^*$ condition to imitate the average mammal-fluke kinematics as reported in biologist data (Fish & J. 1999), and the Strouhal number $St = 0.3$ is fixed in the middle of the optimal thrust production range (Triantafyllou et al. 1991). A few special cases outside these conditions were also simulated: A flipper-like motion using higher $k^* = 0.6$ and $St = 0.6$ to imitate penguin and turtle swimming data with high roll and twist angles to maintain high propulsion and efficiency due to high AR. Also, a tail-like motion at lower amplitude $A = 0.13l^*$ and much higher frequency at $St = 0.46$ inspired by recent robotics studies at similar operating conditions (Zhu et al. 2019, King et al. 2018).

5.3 Impact of sweep on wake structures and propulsive characteristics

A set of example simulation results for both tail-like and flipper-like motions are shown in Figure 5.3, with the flow's vortex structures visualized using the Q-criterion (King et al. 2018). These wake visualizations show that small scale features such as the generation of small turbulent vortices depends on both the geometry and the kinematics. However, the large-scale underlying flow structures illustrated in the bottom row sketches are the same for a given set of kinematics; changing the sweep angle from 20° to 40° simply shifts and scales those structures. Specifically, for the tail-like motions in the left column, the leading edge vortex (LEV) detaches from the top of the fin halfway along the inline length $l^* = L$ for tail-like motions. Similarly, while increasing the sweep angle pushes the LEV back for flipper-like motions, the separation for both cases occurs around 70% along the fin width $l^* = B/2$ for these cases. The period and wavelength of the trailing wake structures also scale with l^* because we have used l^* to define the reduced frequency $k*$ and the amplitude

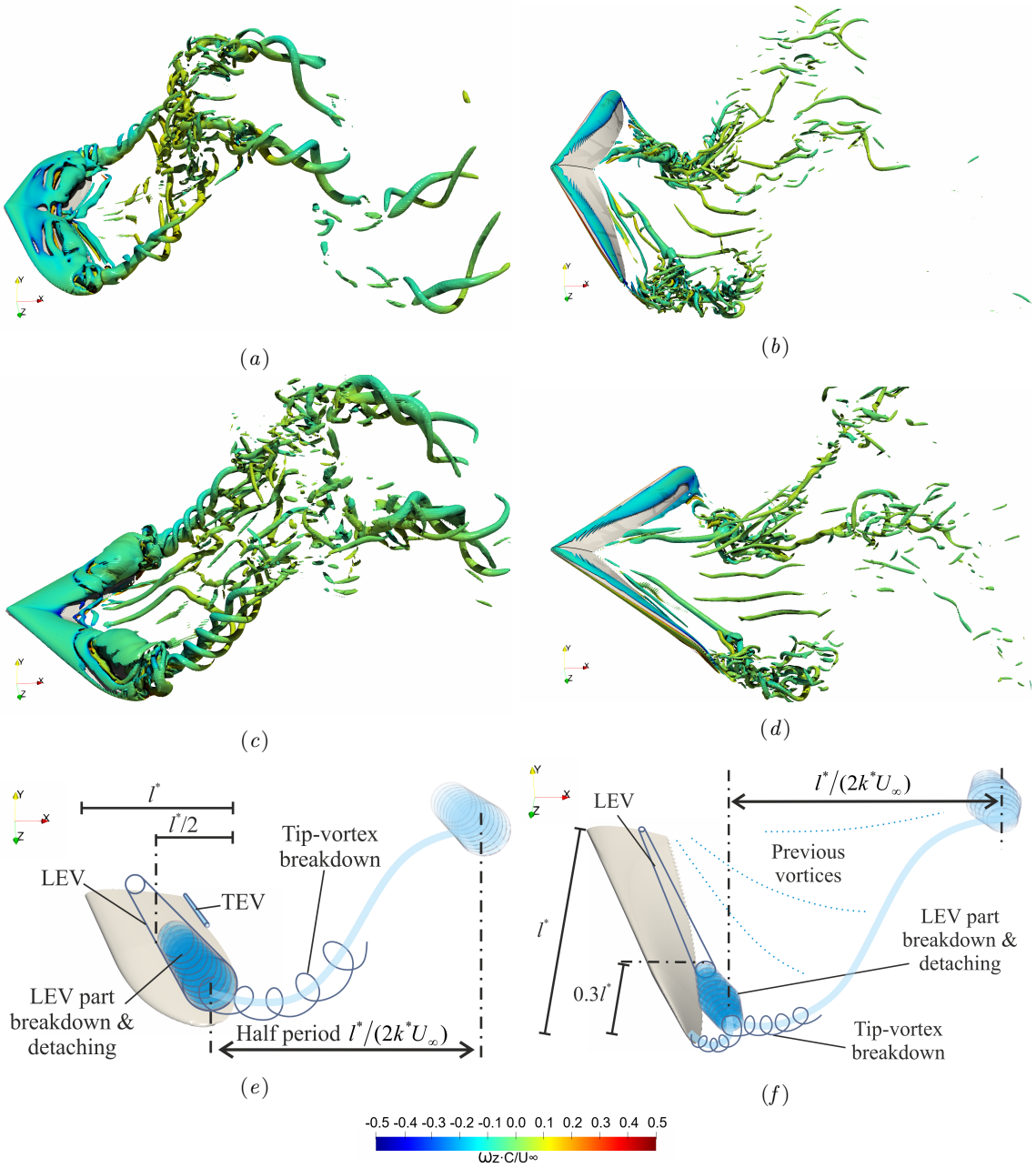

FIGURE 5.3: Flow structures generated by tail-like and flipper-like propulsive swimming at position ① shown in Figure 5.2. Tail-like motions are depicted in pitch-heave for (a) Λ20, (c) Λ40 for $\mathcal{AR}$= 4, and flipper-like motions as in twist-roll for (b) Λ20, (d) Λ40 for $\mathcal{AR}$= 8. Instantaneous vortex structures are visualized using iso-surfaces with 1% of Q_{max} colored by the spanwise vorticity $\omega_z C/U_\infty$. Illustration of vortex-shedding process every half period $(l^*/(2k^*U_\infty))$ of cycle for (e) tail-like motion and (f) flipper-like.

envelop $2A = l^*$. In other words, the sweep angle does not fundamentally change the resulting propulsive flow around the fins other than changing the characteristic length l^*.

We can quantify this invariance of the flow in terms of the integrated propulsive metrics; the coefficients of thrust C_T lift C_L and power C_{Pow} as defined in Equation 2.2 and Equation 2.3, and also the propulsive efficiency η defined as

$$\eta = \frac{\overline{F_x} U_\infty}{\overline{P}} = \frac{\overline{C_T}}{\overline{C_{Pow}}} \tag{5.6}$$

where measured thrust force (F_x), lift force (F_y), and power (P) are calculated from the integration of pressure and viscous forces over the foil. S_p is the foil planform area and overline signifies cycle averaging.

The tail-like kinematics exhibit insignificant changes in the statistics of the force-coefficients with the increase of sweep angle, Fig. 5.4(a). There is a small increase in the range of lift coefficient (maximum and minimum C_L) as well as and the mean and maximum power. However, the thrust coefficients (C_T) show minimal change. This causes the efficiency (η), i.e. the ratio of average thrust to power, to decrease from 31% to 29% as the sweep angle increases. The flipper-like kinematics as presented in Fig. 5.4(b) show the same tendency as the tail-like other than the mean C_T which drops with increasing Λ. This condition makes the flipper-like motions lose $\approx 13\%$ efficiency between $\Lambda 20°$ and $\Lambda 40°$, while the tail-like motions only drop $\approx 2.2\%$.

We next check the significance of the sweep angle and different $\mathcal{AR}$. For tail-like motion, we halve the $\mathcal{AR}$ while maintaining the same St and k^*, Figure 5.5 (a). As a result, the statistic trends are even more insignificant than $\mathcal{AR} = 4$ especially the decrease in power coefficients, with an efficiency loss of only $\approx 1.7\%$.

We use flipper kinematics to check the performance of long $\mathcal{AR} \approx 8$ foils since nearly flippers tend to have higher $\mathcal{AR}$, Figure 5.1. In addition, turtles and penguins are observed to use higher frequency and higher twist amplitude (Rivera et al. 2013, Bannasch et al. 1994). This combination of kinematics is important because the observed large roll amplitude and frequency induces a high local angle of attack α_{max} towards the end of the foil, which would increase drag and reduce efficiency if applied alone. The increase in twist angle compensates for this, limiting α_{max} toward the foil tip to maintain high efficiency (Hover et al. 2004, Zurman-Nasution et al. 2020). In our tests with $\mathcal{AR} = 8$ the large roll-angle amplitude $30° - 45°$ and high twist-angle amplitude $45° - 60°$ increase propulsive $\overline{C_T}$ while maintaining similar sectional maximum angle of attack α_{max}. As such, these optimized flipper-like kinematics improve the efficiency, which now only drops $\approx 6\%$ for various sweep angle because $\overline{C_T}$ are almost constant.

We also studied the other two proposed arguments for the benefit of increased sweep angle i.e. the LEV detachment delay and its effect in moment coefficients. Our simulations do not see any significant delay on the LEV detachment benefited from sweptback angle variation,

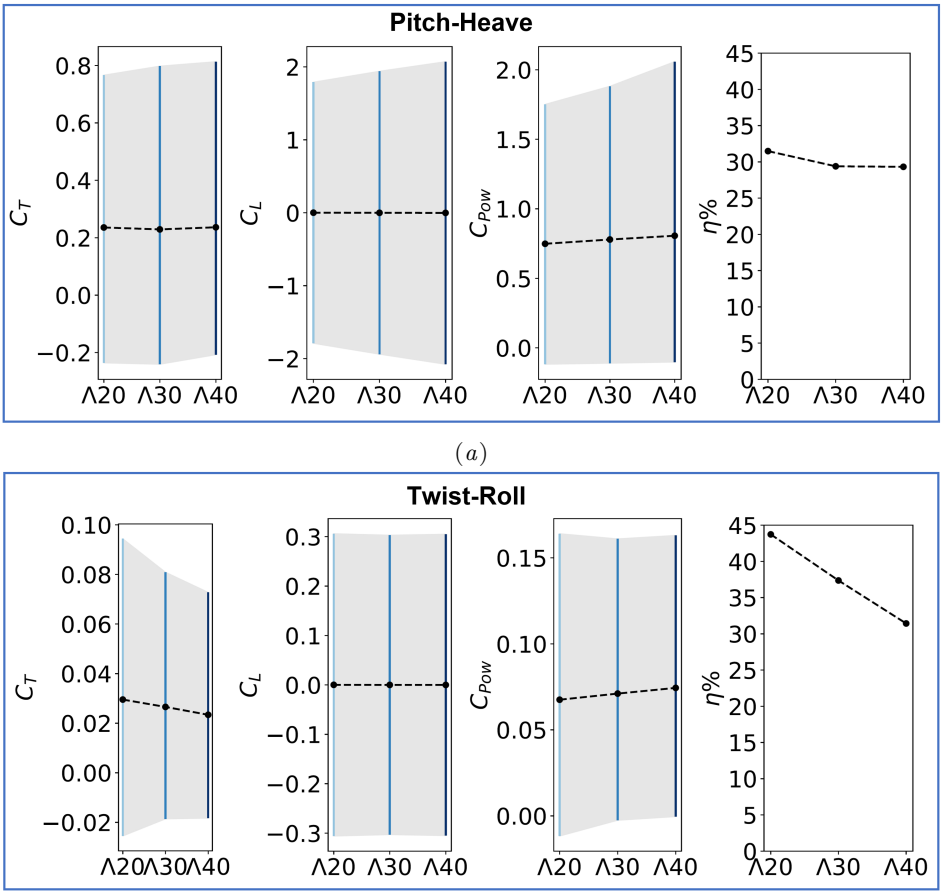

FIGURE 5.4: Statistics of (a) tail-like and (b) flipper-like kinematics with the variation of sweep angle Λ on $\mathit{AR} = 4$ foil, $St = 0.3$, and $k^* = 0.3$. The tail-like cases in (a) correspond to those shown in Figure 5.3(a,c). Statistics are presented as the mean of coefficients of lift force (C_L), thrust force (C_t) and power (C_{pow}), shown in dashed lines, while grey shade represents the range the maximum and minimum values over a cycle. Force statistics are generally constant while a slight increase in power reduces the average efficiency η when Λ increases.

Figure 5.6. Contrarily, Wong et al. (2013) reported a modulated C_L peak for rolling high-AR flat plate between $\Lambda 45°$ and $\Lambda 0°$, because their ratio of LEV width to chord length are relatively big (unlike flipper) affecting slightly the LEV detachment timing in between the two sweep angles. The similarity in the LEV appearance on $\Lambda 20°$ and $\Lambda 40°$ (Figure 5.3) can also indicate why there is no C_L peak delay meaning that the LEV stability does not change with Λ. Depending on the kinematics and AR, there are slight variations in the breakdown of the main vortex structures, but this is not observed to have a consistent or significant impact on the force statistics.

We have checked the coefficients of moment for AR 2, 4 and 8, but there is also no significant alteration on the coefficients of pitching and rolling moment caused by the sweep-angle variation (see Appendix E).

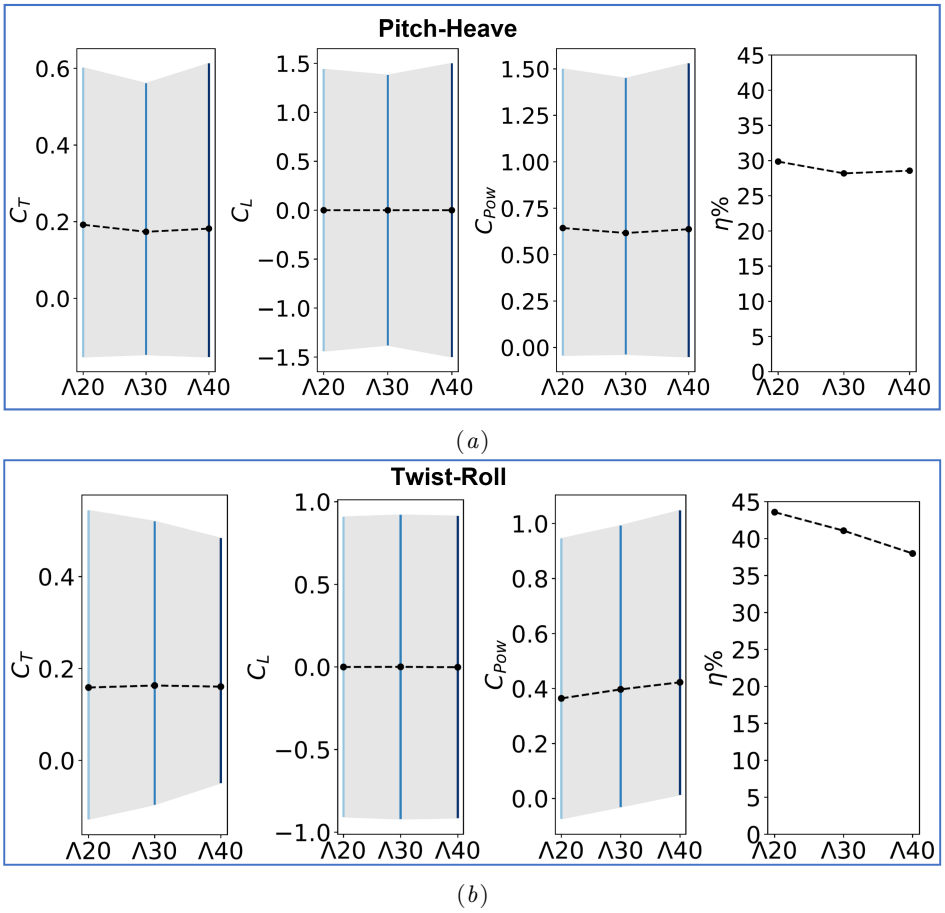

FIGURE 5.5: Sweep angle variation even become more insignificant in different $\mathcal{AR}$ such as (a) lower $\mathcal{AR} = 2$ of tail-like in $St = 0.3$ and $k^* = 0.3$, and (b) higher $\mathcal{AR} = 8$, $St = 0.6$, and $k^* = 0.6$ of the flipper-like motion for optimum thrust and efficiency shown in Figure 5.3 (b) and (d).

5.4 Discussion

Finally, the 12 simulation cases discussed above and 27 others are collected in Figure 5.7(a) using parallel coordinates to simultaneously present the geometric and kinematics inputs and the propulsive statistics outputs in one graph along with their correlations in Figure 5.7(b). The complete data are presented in Appendix D. Here, the main inputs are the motion types, sweep angles, $\mathcal{AR}$s, and flapping amplitude A/l^*. Different St and k^* are represented by two flapping amplitudes for biological-inspired (high amplitude, low frequency) and engineering-inspired (low amplitude, high frequency) motions, whereas different motion types represent the change in α_{max}. Only cases with negligible $\overline{C_L}$ are presented while C_L RMS data are presented as one of the outputs together with $\overline{C_T}$, $\overline{C_{Pow}}$ and η. Full data are presented in the Appendix D.

These plots summarize our primary finding that the sweep angle is not responsible for the large potential variation in propulsive statistics we have observed over this simulation set. The large variation in the sweep angle explains low correlation coefficients with the outputs. Similarly the $\mathcal{AR}$ lines, for instance $\mathcal{AR} = 4$, spread all over the output range. It shows that

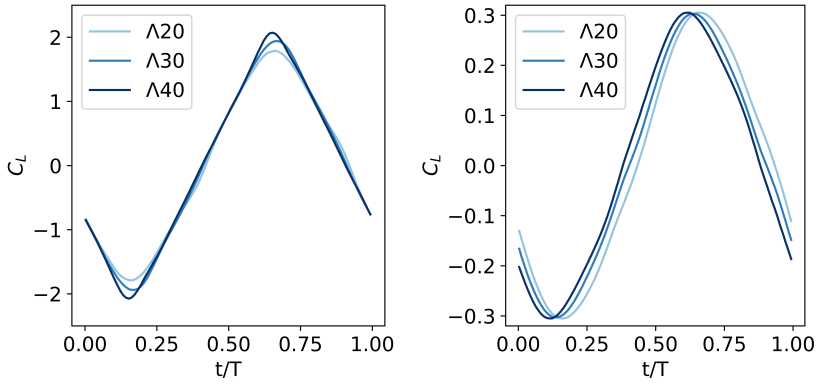

FIGURE 5.6: Lift coefficient of (a) tail-like and (b) flipper-like motion in Figure 5.4 in one cycle period (T). Both graphs show no LEV detachment delay as Λ increases.

the influence from the sweep angle, the $\mathcal{AR}$ and their combination on the flow are secondary compared to other parameters.

Unlike Λ and $\mathcal{AR}$, the kinematics inputs i.e. motion and A/l^* show higher correlations to the outputs especially motion to the efficiency. Combined motions are seen to be more beneficial than single motions as shown in Figure 5.7(a). The efficiencies above 25% belong to the cases with combined motions and higher amplitude (biological-inspired) conditions, with flipper-like motion giving the highest efficiency. All types of motion with lower amplitude (engineering-inspired) gives efficiencies between 4%-20% with combined motions and pure pitching giving higher efficiencies above 13%. The tail-like motions with high frequency (engineering-inspired) produce relatively higher $\overline{C_T}$ than the flipper-like, and single motions in animal operating condition give no benefit at all. High correlations of output with motion indicate a similar correlation with the α_{max} or spanwise derivative of maximum angle-of-attack as previously concluded in Chapter 4. Other strong correlations are seen in the forces and power to the amplitude A/l^* input indicating a similar correlation to the flapping frequency and St. The correlations prove that modification of kinematic parameters is more influential than the planform geometry for propulsive flapping.

5.5 Conclusion

In conclusion, we have fixed other parameters so that they do not interfere with the main parameters i.e. the sweep angle and $\mathcal{AR}$. This method produces a more extensive and more reliable analysis for the influence of sweep angle in propulsive flapping foil. Generally, we have seen no advantages for having sweptback leading-edge of flapping with tail-like motions. Despite no benefit, having swept planform also does not contribute to a significant disadvantage. This can explain why biologist data for fish caudal fins and mammal flukes have a greater range of sweep angle and look scattered on a wider range of aspect ratio. From a biology perspective, this signifies that the so-called fastest fishes from the Scombridae family

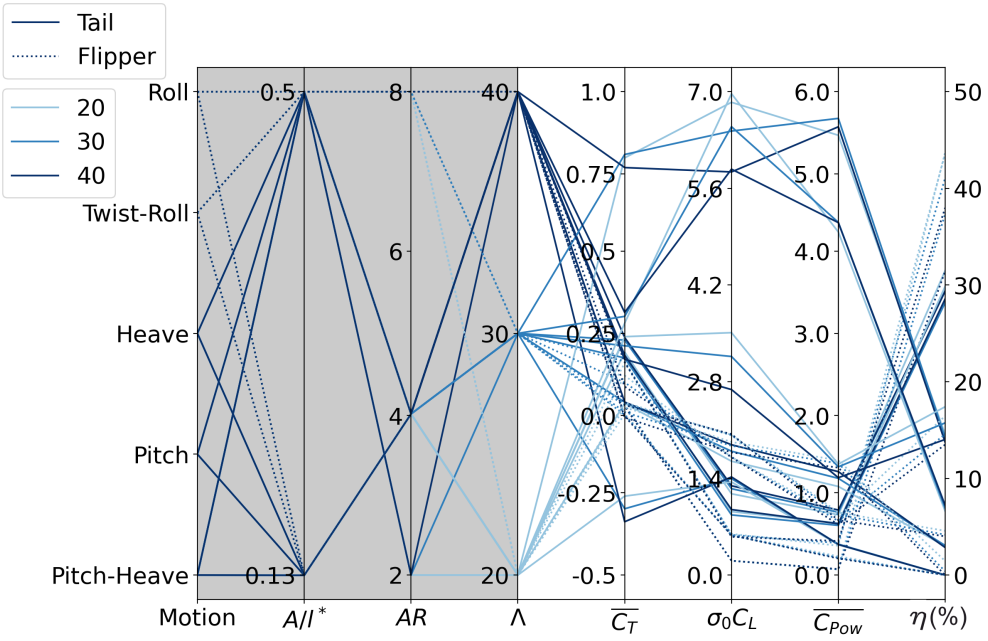

(*a*)

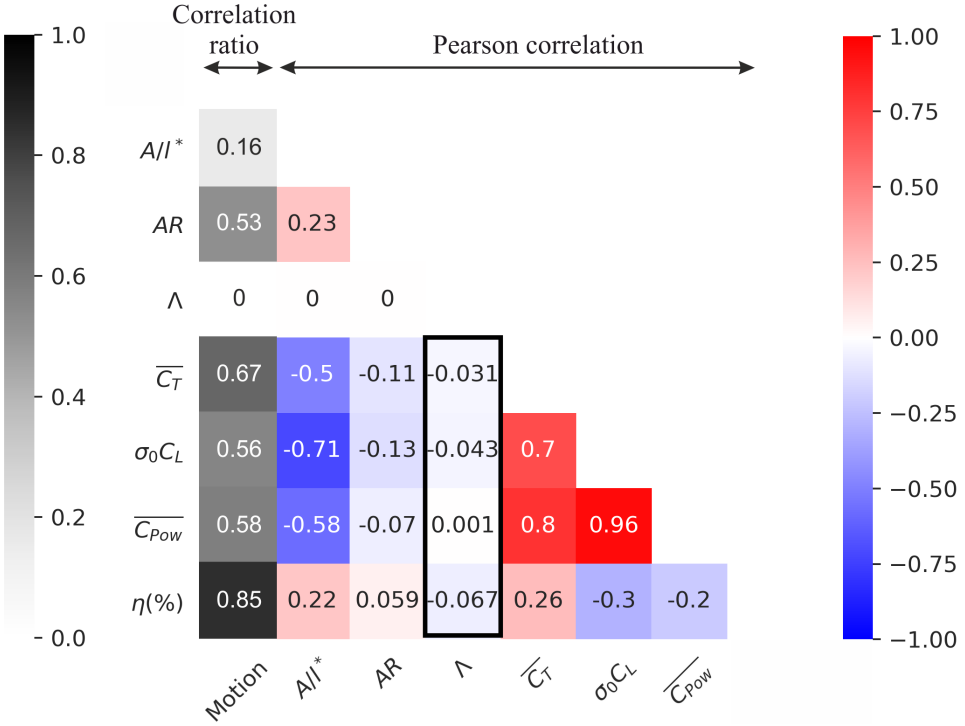

(*b*)

FIGURE 5.7: The relations from 39 simulations among the various inputs and output parameters i.e. the mean thrust coefficient $\overline{C_T}$, zero-mean standard deviation $\sigma_0 C_T$, mean power coefficients $\overline{C_{Pow}}$ and efficiency η, are presented in (a) a parallel-coordinate graph with grey shaded inputs, and (b) a heat-map graph of correlation coefficients using Pearson and correlation ratio with a box highlighting Λ correlation. Continuous lines in Fig.(a) are for the tail-like and dotted lines for the flipper-like motions. The lines on the output area of Fig.(a) regroup to their 3-color Λ showing that sweep angles have an insignificant impact on the output in spite of the large input variation convinced by the correlation values in the box of Fig (b).

or mammals from the Delphinidae family can have either high or low sweep angle given any $\mathcal{AR}$ range without losing thrust and hurting much of their propulsive efficiency.

Similarly, the sweep angle does not give advantage to flipper-like motions, but an increased sweep angle tends to lose efficiency due to increased power requirements and loss of thrust, although this loss can be mitigated by optimizing the kinematics. The sweep angle also does not affect the lift coefficient, which is beneficial as flippers are also used as a lift regulator in animal swimming (Cooper et al. 2008). Overall, flippers can be sweptback but need to compensate by increasing tip frequency and Strouhal number to recover the lost thrust force.

Chapter 6 Summary and outlook

This work studies the flow characteristic of flapping foil seen in animal propulsors mainly using 3D simulations, while at the same time presents the possibilities to relate the 3D simulation from the 2D or the strip theory, and characterizes the 3D, 2D flows and their transitions. As previously stated in Chapter 1, the flow over an infinite bluff body experiencing 2D kinematics is reported to not always produce 2D flow in experiments. There are transitions from 2D to 3D flow structures that have been reported for a non-oscillating cylinder in low-Reynolds experiments caused by 2 types of instabilities, i.e. the braid centrifugal and the shear layer instability. Some numerical studies also show this transition in oscillating foil just after the deflected wakes. The causes of these transitions are unclear, contributing to the confusion of whether strip theory is or is not valid for infinite flapping-foil studies.

Meanwhile, a finite foil experiencing heave, pitch, or rotation is bound to 3D flow mainly due to the 3D effects such as the tip vortex, aspect ratio, and spanwise flow affecting the foil's vortex dynamic, forces and efficiency. Tip vortex and aspect ratio are general finite foil's characteristics but the spanwise flow is mainly found in a rotating foil or a delta wing. Similar to infinite foil, using strip theory can produce incorrect flow fields but 3D effects add more complexities. Literatures show that using 2D simulation, when the flow is affected by 3D effects, produces irregularity and fluctuation of forces in stationary bodies, along with the low base-pressure reading and overprediction of mean drag and lift coefficients.

Flapping foils are extensively studied in this work using 3D simulations starting from their flow characteristics, 3D effects, comparison with 2D simulations and applications in biological swimming/flying. Firstly, an infinite foil is combined with 2D kinematics of heaving, pitching and their combination to explain where 2D simulation or strip theory can be applied and where it cannot. Secondly, the flow over a finite foil with 3D kinematics of rolling, twisting and their combination is studied along with the influence of the tip, $\mathcal{R}$, and the appearance of spanwise flow. A finite foil experiencing 3D kinematics similar to flipper-like motion is the least studied compared to the one experiencing 2D kinematics or tail-like motion, leaving a room to analyse their special flow characteristics. The flow is expected to have a combination of a finite foil with 2D kinematics and the beginning phase of revolving foil. The twist motion, i.e. increasing pitching amplitude along the span (twist), is introduced which imitates the flipper motion during pronation-supination. This is an approach of controlled flexibility which combines the benefits of having chordwise and spanwise flexibility. Lastly, the spanwise flow

effect is studied in the form of a sweptback angle as found in natural planforms such as fishtails, mammal flukes, flippers and wings. Biologist data of sweep angles for flapping foils are relatively scattered in a wider range of $\mathcal{AR}$, unlike the stationary swept/delta wings that have clear limits on stability effect. One literature describes the sweep angle benefit for birds during gliding for drag reduction, but the effect during constant flapping should not necessarily the same. Several analytical results show promising advantages while other experimental studies find the opposite. Brief summaries are further explained in each of the following sections, listing the important findings from three main projects in Chapter 3 to Chapter 5.

6.1 Influence of three dimensionality on infinite flapping foil

Flapping foil kinematics can regulate the flow into spanwise-uniform or 2D flow when the flow previously exhibits spanwise perturbation (3D flow) in stationary foil promoted solely by 10° bias angle in shear-layer transition flow $Re \approx 10^3$–10^4. These 2D ranges can be found at medium Strouhal number $St_A \approx 0.3$ in heaving, pitching and the coupled motions, with the ranges of pure pitching and coupled motions are slightly wider. The 2D range for coupled motion lies at $St_A \approx 0.15$–0.45 similar to the optimal Strouhal numbers for swimming animals found by Triantafyllou et al. (1993). In the 2D ranges, the flow characteristics are similar between 2D and 3D simulations creating a possibility to apply strip theory. Outside of these ranges, either below or above the medium St_A, running 2D simulation will incorrectly model the 3D characteristics of the flow. The flow in 2D simulations will produce non-dissipative vortices creating wake disturbance and high force fluctuations. It is conclusive that applying the strip theory outside of the 2D range will provide incorrect flow fields.

The transition from 3D flow in stationary foil into 2D flow in medium Strouhal number is mainly promoted by the kinematics. Meanwhile, the 2D-to-3D transition at higher Strouhal number is caused by increased energy in the vortices that overpower the viscous effect. While the shear layer transition for infinite stationary cylinder happens at $Re \approx 270$ (Williamson 2006), the transition for infinite flapping foil happens at higher Reynolds numbers $Re_{LEV} \approx 4000$. The 2D-to-3D transition is not related only after the wake deflection as previously stated by Deng & Caulfield (2015), Deng et al. (2016). The wakes in our case are naturally deflected due to the bias angle, yet the flow can still be regulated into 2D in medium St_A by the kinematics.

6.2 Effects of aspect ratio on rolling and twisting foils

A finite foil experiencing 3D kinematics like flipper motion produces more complicated vortex dynamics and wakes than an infinite foil due to aspect ratio and tip effects. The 2D characteristics from the infinite foil at medium $St_A = 0.3$ are similar, but the flow at the lowest St_A (root section) does not exhibit any spanwise perturbation if $\mathcal{AR}$ is not relatively long. This is

due to the strong flow interaction between sections indicated by the appearance of spanwise flow, similar to rotating and delta wing cases, whose strength evolves with the variation of aspect ratio.

The cross-sections of the foil experience a spanwise kinematic-derivative or a change of angle of attack along the span towards the tip due to roll. The shorter the aspect ratio, the stronger the spanwise derivative affects the flow. As the $\mathcal{AR}$ is reduced, augmentations are seen in the peak of spanwise flow, near-wake circulation at the root, tip circulation and root C_L . As the aspect ratio is progressively increased to reach idealised infinite span, the case of $S/C = 6$, the characteristics of infinite foil re-appear reducing all those values to the minimum. The root section is now dominated by spanwise perturbation and vortex dissipation seen in the infinite stationary-foil case.

Adding a quarter-cycle twist, or progressive pitch towards the tip, decreases the maximum angle of attack attained by a pure rolling motion, and so does the spanwise derivative. The combination of twist and roll causes lower peak values of the spanwise flow, circulations and forces such as C_L. However, these conditions are apparently advantageous to reduce vortex breakdown at the tip and near wakes, and also to prolong the attachment of the vortices.

Despite all the 3D flow characteristics in finite foil with 3D kinematics, the average values of peak C_L show that it is still possible to use scaled 2D-simulation. The evolution of C_L derivative over the St_A^2 —the added mass or body acceleration component—surprisingly follows the Prandtl finite wing theory. Each of the finite foil's slope can be scaled from 2D (strip) C_L and aspect ratio. It opens the possibility to scale even at the sectional level of C_L from 2D simulation while the aspect ratio is varied.

6.3 Fin sweep angle does not determine flapping propulsive performance

Several biologists hypothesize the importance of having a sweep angle for swimming or flying animals supported by some analytical results. However, experimental results for any single motion, both impulsive and periodic motions in heaving, pitching and rolling, do not see significant improvement on the forces, moments and efficiency. (Fish & J. 1999) provide an extensive data collection of marine mammals for sweep angle with $\mathcal{AR}$ limitation trend similar to delta wings described in (Shortal & Maggin 1946). However, adding more data from other literatures enlarge this collection and make the trend in Figure 5.1 are far scattered covering the real influence of the sweep angle.

Keeping kinematic and dimension parameters constant helps to isolate the influence of sweep angle and $\mathcal{AR}$, yet they surprisingly do not show significant contribution to the propulsion and performance. The correlation of sweep angle and $\mathcal{AR}$ show far less significant compared to the parameters that build the kinematics such as Strouhal number, reduced frequency, flapping amplitude and maximum angle of attack. With the adjustment of kinematic parameters,

coupled motion can also reach maximum propulsion and optimum efficiency which cannot be achieved by single motions. It proves that animals can actually have a wider range of sweep angles and $\mathcal{A}$s, as shown in the collection of biologist data, with proper adjustment on the kinematics to support optimum propulsive performance.

6.4 General conclusion and outlook

The following important remarks conclude all the studies we have done for flapping foils.

1. The strip theory application is possible for flapping foils as long as their kinematics are in the ranges of medium Strouhal numbers, close to the optimum performance of swimming animals, where the flow is generally two dimensional. Applying strip theory outside of these ranges produces incorrect flow fields.
2. Even though general finite-foil flows are three dimensional, the sectional average of peak force coefficients can be scaled using Prandtl finite wing theory from 2D simulations, thus facilitate the use of scaled strip theory for various $\mathcal{A}$ finite foils.
3. For flipper-like motion, the spanwise derivative of kinematics drives the sectional flow distribution, and its effect is stronger as $\mathcal{A}$ decreases.
4. Combination of two motions both in two-dimensional (tail-like) and three-dimensional motions (flipper-like) are more advantageous for propulsion and efficiency. It explains why animals have more variety of motions for lift-based locomotion.
5. Once a flapping kinematic is added, the parameters that generally affect stationary-foil such as sweep angle and $\mathcal{A}$ are far less significant compared to the kinematic parameters.
6. The flow characteristics of each of single kinematics are distinct, and so are the combination motions which are not the product nor addition of the singles.

In the future, several items below are worthwhile to consider for the next flapping foil research.

1. Animals are able to control the flow over their propulsors through bone movement accomodating a flexible morphing in addition to the propulsor's structural flexibility. It is interesting to study in detail the 3D controlled flexibility in a wider range instead of some single-axis flexibility.
2. We have understood that coupled motions are different than the combination of two single motions. Thus, a combination of three kinematics might also produce a unique flow. Two single motions, i.e. surge (2D) and yaw (3D), have not been studied in this work as either single of a part of combined motions.

3. We also have not studied the combination between any 2D and 3D motions. Shark tails are seen to have a combination of pitch, heave and twist.

4. Despite the extensive research and publications for animal locomotion, animals behave differently in captivity than in nature where they are more unpredictable due to the adjustment of environmental conditions. For future experimental fluid dynamics, an in-situ measurement tool —such as underwater PTV (Particle Tracking velocimetry) —is favorable to record the flow fields of swimming animals in their natural habitats.

Appendix A Wake shape

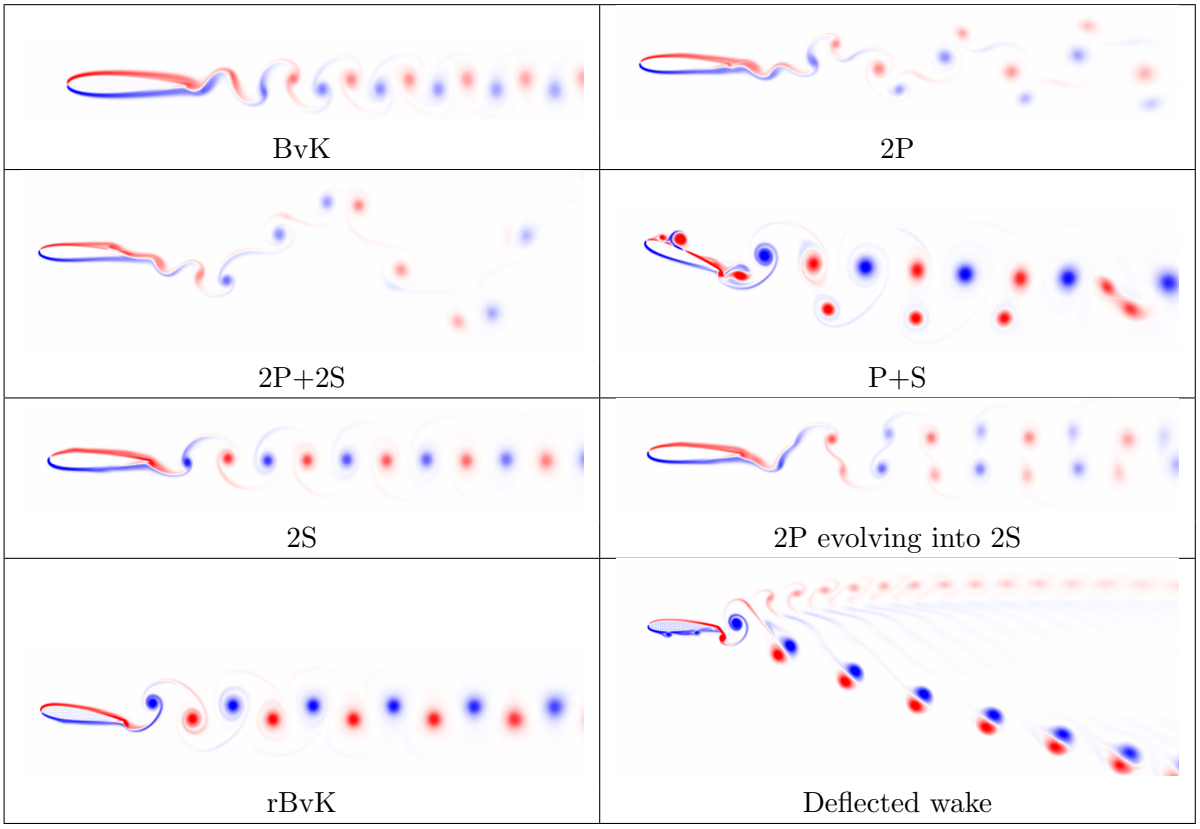

FIGURE A.1: Wake shed types based on Williamson & Roshko (1988), Andersen et al. (2016) produced with BDIM 2D simulations. Type P means vortex pair and S means single. Type 2S is an indicator of drag-to-thrust transition, whereas BvK is a drag-producing and rBvK is a thrust-producing. Deflected wakes here is a thrust producing while the remaining of other types are mostly drag producing.

Appendix B Infinite foil wake evolution

TABLE B.1: 3D spanwise-vorticity contour at $St_D = 0.3$ for infinite foil experiencing heave, pitch and coupled motions

A_D ($\boldsymbol{St_A}$)	Heave	Pitch	Coupled
0.0625 (**0.019**)			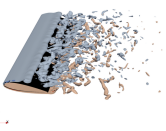
0.125 (**0.037**)		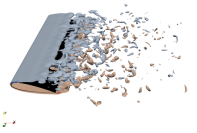	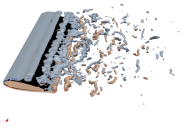
0.25 (**0.075**)	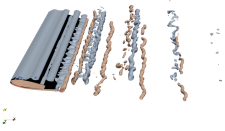		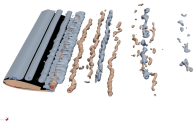
0.5 (**0.15**)	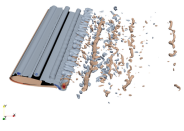	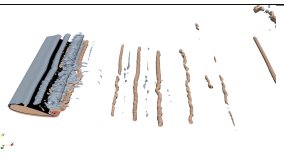	
1.0 (**0.3**)	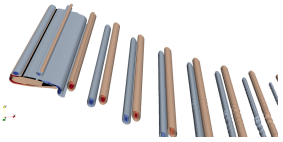	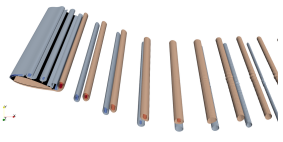	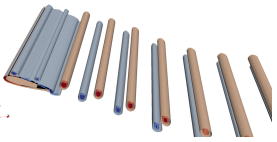
1.5 (**0.45**)	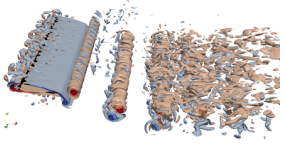	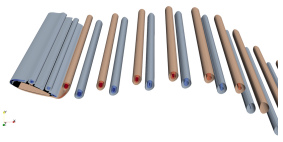	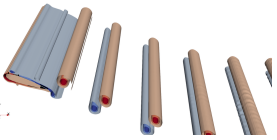
2.0 (**0.6**)	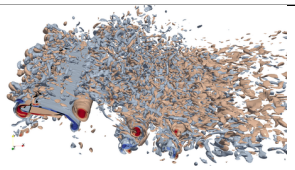	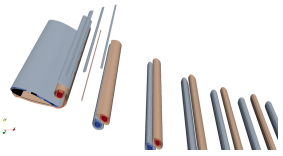	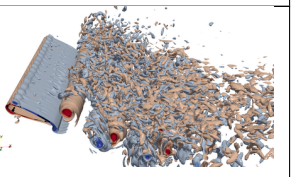
3.0 (**0.9**)	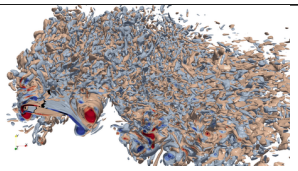	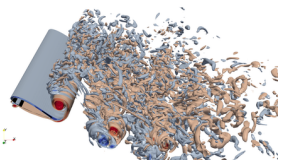	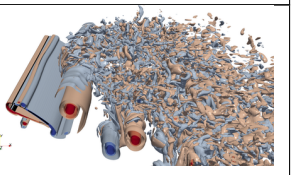
3.75 (**1.125**)	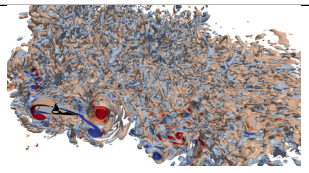	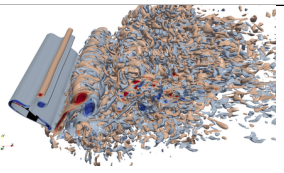	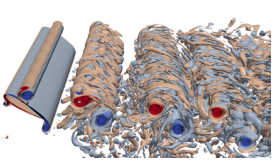

Appendix C Biologist data

TABLE C.1: Sweep angle and $\mathcal{R}$ data from various literature

Species name	Common name	Body part	$\mathcal{R}$	$\Lambda(^\circ)$	Source
Delphinapterus leucas	Beluga	Fluke	3.3	29.9	
Delphinapterus leucas	Beluga	Fluke	4	14.6	Fish & J. (1999)
Delphinapterus leucas	Beluga	Fluke	3.4	27.7	
Cephalorhynchus commersonii	Commerson Dolphin	Fluke	3.3	37.5	
Delphinus delphis	Dolphin	Fluke	4	33.1	
Delphinus delphis	Dolphin	Fluke	3.5	36.3	
Delphinus delphis	Dolphin	Fluke	3.9	31.7	
Delphinus delphis	Dolphin	Fluke	3.8	32.5	
Delphinus delphis	Dolphin	Fluke	4.1	34.1	
Delphinus delphis	Dolphin	Fluke	4.5	36.2	
Delphinus delphis	Dolphin	Fluke	4.9	34.7	
Delphinus delphis	Dolphin	Fluke	4.4	31	
Delphinus delphis	Dolphin	Fluke	4.2	32.9	
Delphinus delphis	Dolphin	Fluke	4.5	37	
Delphinus delphis	Dolphin	Fluke	4.1	34.6	
Delphinus delphis	Dolphin	Fluke	4.3	32.6	
Delphinus delphis	Dolphin	Fluke	4.1	34.4	
Grampus griseus	Risso Dolphin	Fluke	5.7	29.9	
lnia geoffrensis	Amazon river dolphin	Fluke	2	42.8	
lnia geoffrensis	Amazon river dolphin	Fluke	2.6	38.9	
Lagenorhynchus acutus	Atlantic white-sided dolphin	Fluke	3.9	41.3	
Lagenorhynchus acutus	Atlantic white-sided dolphin	Fluke	4	39.6	
Lagenorhynchus acutus	Atlantic white-sided dolphin	Fluke	3.9	40.5	
Lagenorhynchus acutus	Atlantic white-sided dolphin	Fluke	4.8	35.3	
Lagenorhynehus obliquidens	Pacific white-sided dolphin	Fluke	4.4	36.9	
Lagenorhynehus obliquidens	Pacific white-sided dolphin	Fluke	4.8	29	
Lagenorhynehus obliquidens	Pacific white-sided dolphin	Fluke	4.5	29.4	
Lagenorhynehus obliquidens	Pacific white-sided dolphin	Fluke	4.7	32.1	

Lipotes vexillifer	Baiji fresh-water dolphin	Fluke	3.1	40.4
Lissodelphis borealis	Northern right whale dolphin	Fluke	3.1	38.6
Pseudorca crassidens	false killer-whale dolphin	Fluke	5	28.5
Pseudorca crassidens	false killer-whale dolphin	Fluke	4.6	29.1
Pseudorca crassidens	false killer-whale dolphin	Fluke	6.2	26
Steno bredanensi	Rough-toothed dolphin	Fluke	4	30
Stenella clymene	Clymene dolphin	Fluke	5.2	23.6
Stenella coeruleoalba	Striped dolphin	Fluke	5.2	26.4
Stenella eoeruleoalba	Striped dolphin	Fluke	5.2	32.3
Stenella eoeruleoalba	Striped dolphin	Fluke	4.4	26.6
Stenella plagiodon	Atlantic spotted dolphin	Fluke	4.6	29.2
Stenella plagiodon	Atlantic spotted dolphin	Fluke	4.3	27.5
Stenella plagiodon	Atlantic spotted dolphin	Fluke	4	32.1
Stenella plagiodon	Atlantic spotted dolphin	Fluke	5.3	26.3
Stenella plagiodon	Atlantic spotted dolphin	Fluke	4	30.3
Stenella plagiodon	Atlantic spotted dolphin	Fluke	4.1	30.4
Stenella plagiodon	Atlantic spotted dolphin	Fluke	4.5	25
Tursiops truncatus	Bottlenose dolphin	Fluke	3.8	34.5
Tursiops truncatus	Bottlenose dolphin	Fluke	3.6	25.8
Tursiops truncatus	Bottlenose dolphin	Fluke	3	34.4
Tursiops truncatus	Bottlenose dolphin	Fluke	3.1	38.8
Tursiops truncatus	Bottlenose dolphin	Fluke	3.4	34.8
Tursiops truncatus	Bottlenose dolphin	Fluke	4.1	27.6
Tursiops truncatus	Bottlenose dolphin	Fluke	3	37.6
Tursiops truncatus	Bottlenose dolphin	Fluke	4.1	34.4
Orcinus orca	Orca	Fluke	4.5	27.7
Orcinus orca	Orca	Fluke	4.9	17.8
Orcinus orca	Orca	Fluke	5	22.8
Orcinus orca	Orca	Fluke	5.5	17.3
Orcinus orca	Orca	Fluke	4.7	4.4
Phoeoenoides dalli	Dall's porpoise	Fluke	4.4	5.4
Phoeoenoides dalli	Dall's porpoise	Fluke	4.8	12.3
Phocoena phocoena	Harbour porpoise	Fluke	3.5	32
Phocoena phocoena	Harbour porpoise	Fluke	3.9	35.2
Globicephala macrorhynchus	Pilot Whale	Fluke	5.8	27.1
Globicephala macrorhynchus	Pilot Whale	Fluke	5.2	29.3
Globicephala macrorhynchus	Pilot Whale	Fluke	5	14.4
Globicephala melaena	long finned pilot whale	Fluke	4.6	33.7
Kogia breviceps	Pygmy sperm whale	Fluke	3.7	36.3
Kogia breviceps	Pygmy sperm whale	Fluke	5.1	25.8
Kogia breviceps	Pygmy sperm whale	Fluke	3.9	33.4
Mesoplodon densirostris	Blainville's beaked whale	Fluke	5.1	28.2
Mesoplodon europaeus	Gervais' beaked whale	Fluke	4.8	26.9
Mesoplodon europaeus	Gervais' beaked whale	Fluke	4.1	33.3
Mesoplodon europaeus	Gervais' beaked whale	Fluke	5.3	26.9
Mesoplodon europaeus	Gervais' beaked whale	Fluke	5.1	28.5
Mesoplodon mirus	True's beaked whale	Fluke	4.8	31.4
Peponocephala electra	Melon-headed whale	Fluke	4.4	34.2

Ziphius cavirostris	Cuvier's beaked whale	Fluke	3.8	30	
Ziphius cavirostris	Cuvier's beaked whale	Fluke	3.9	31.7	
Ziphius cavirostris	Cuvier's beaked whale	Fluke	3.7	39.3	
Scomber japonicus	Pacific mackarel	Caudal fin	3.8	47.5	Magnuson (1978)
Sarda chiliensis	Pacific bonito	Caudal fin	4.6	44	
Auxis rochei	Bullet mackarel	Caudal fin	6.6	31.5	
Euthynnus affinis	Kawakawa	Caudal fin	6.55	35	
Euthynnus pelamis	Skipjack tuna	Caudal fin	6.85	35	
Thunnus albacores	Yellowfin tuna	Caudal fin	6.35	43.5	
Thunnus obesus	Bigeye tuna	Caudal fin	6	42	
T. Brasiliensis	Bat	Wing	8.2	38	Hubel et al. (2016)
M. Velifer	Bat	Wing	6.2	35.65	
Leptonycteris yerbabuenae	Bat	Wing	6.95	12	Von Busse et al. (2012)
Falconidae	Falcon	Wing	4.2	26.5	Klaassen van Oorschot et al. (2016)
Accipitridae	Hawk	Wing	4.1	23	
Strigidae	Owl	Wing	3.75	16.5	
Hawkmoth Manducs Sexta	Hawkmoth	Wing	5.48	20.37	Willmott & Ellington (1997)
Columba Livia	Pigeon	Wing	6	30	Pennycuick (1968)
Megaptera novaeangliae	Humpback Whale	Pectoral fin	6.1	19	Fish & Battle (1995)
Plesiosaurus dolichodeirus	Plesiosaurus	Fore limb	9.85	18	Carpenter et al. (2010)
Plesiosaurus dolichodeirus	Plesiosaurus	Hind limb	10.6	29	
Romaleosaurus victor	Plesiosaurus	Fore limb	9.51	37.5	
Romaleosaurus victor	Plesiosaurus	Hind limb	10.99	45	
Thalassiodracon hawkinsi	Plesiosaurus	Fore limb	9.59	13	
Thalassiodracon hawkinsi	Plesiosaurus	Hind limb	10.29	35	
Mola-Mola	Ocean sunfish	Clavus fin	5.725	15.04	Gurdek Bas et al. (2015)
Carettochelys insculpta	Pig-nosed turtle	Fore limb	3.46	77.5	Rivera et al. (2013)
Caretta caretta	Loggerhead sea turtle	Fore limb	7.92	45	
Aptenodytes forsteri	Emperor Penguin	Pectoral fin	9.84	26	Sato et al. (2010)
Rhinoptera bonasus	cownose ray	Pectoral fin	4.12	32.2	Russo et al. (2015)
Dasyatis sabina	Antlantic ray	Pectoral fin	1.96	29.78	
Dipturus argentinensis	longnose skate	Pectoral fin	1.96	31	Astarloa et al. (2008)
Manta alfredi	Manta ray	Pectoral fin	6.52	25.58	Rambahiniarison et al. (2016)

Appendix D Sweep angle and $\mathcal{AR}$ simulation results

TABLE D.1: Simulation results for sweep angle and $\mathcal{AR}$ variation

Motion	St	k^*	A/l^*	$\mathcal{AR}$	$\Lambda(^\circ)$	$\overline{C_T}$	$\sigma_0 C_T$	$\overline{C_{Pow}}$	η (%)
Pitch-Heave	0.3	0.3	0.5	4	20	2.36E-01	2.36E-01	7.48E-01	31.5
Pitch-Heave	0.3	0.3	0.5	4	30	2.29E-01	2.29E-01	7.79E-01	29.4
Pitch-Heave	0.3	0.3	0.5	4	40	2.37E-01	2.37E-01	8.07E-01	29.4
Twist-Roll	0.3	0.3	0.5	4	20	2.95E-02	2.95E-02	6.75E-02	43.7
Twist-Roll	0.3	0.3	0.5	4	30	2.66E-02	2.66E-02	7.11E-02	37.4
Twist-Roll	0.3	0.3	0.5	4	40	2.34E-02	2.34E-02	7.44E-02	31.4
Pitch	0.3	0.3	0.5	4	20	-2.55E-01	-2.55E-01	3.77E-01	0.0
Pitch	0.3	0.3	0.5	4	30	-2.94E-01	-2.94E-01	3.83E-01	0.0
Pitch	0.3	0.3	0.5	4	40	-3.35E-01	-3.35E-01	3.79E-01	0.0
Heave	0.3	0.3	0.5	4	20	3.28E-02	3.28E-02	1.10E+00	3.0
Heave	0.3	0.3	0.5	4	30	3.67E-02	3.67E-02	1.20E+00	3.1
Heave	0.3	0.3	0.5	4	40	3.66E-02	3.66E-02	1.28E+00	2.9
Roll	0.3	0.3	0.5	4	20	-1.64E-04	-1.64E-04	2.32E-01	0.0
Roll	0.3	0.3	0.5	4	30	-3.13E-03	-3.13E-03	2.14E-01	0.0
Roll	0.3	0.3	0.5	4	40	-7.24E-03	-7.24E-03	2.05E-01	0.0
Pitch-Heave	0.3	0.3	0.5	2	20	1.92E-01	1.92E-01	6.43E-01	29.9
Pitch-Heave	0.3	0.3	0.5	2	30	1.74E-01	1.74E-01	6.16E-01	28.2
Pitch-Heave	0.3	0.3	0.5	2	40	1.82E-01	1.82E-01	6.37E-01	28.6
Twist-Roll	0.6	0.6	0.5	8	20	1.59E-01	1.59E-01	3.64E-01	43.6
Twist-Roll	0.6	0.6	0.5	8	30	1.63E-01	1.63E-01	3.97E-01	41.1
Twist-Roll	0.6	0.6	0.5	8	40	1.61E-01	1.61E-01	4.23E-01	38.0
Roll	0.6	0.6	0.5	8	20	2.06E-02	2.06E-02	1.42E+00	1.5
Roll	0.6	0.6	0.5	8	30	5.50E-03	5.50E-03	1.39E+00	0.4
Roll	0.6	0.6	0.5	8	40	-1.11E-02	-1.11E-02	1.33E+00	0.0
Pitch-Heave	0.46	1.77	0.13	4	20	7.95E-01	7.95E-01	5.46E+00	14.6
Pitch-Heave	0.46	1.77	0.13	4	30	8.05E-01	8.05E-01	5.67E+00	14.2
Pitch-Heave	0.46	1.77	0.13	4	40	7.65E-01	7.65E-01	5.56E+00	13.7
Twist-Roll	0.46	1.77	0.13	4	20	1.19E-01	1.19E-01	7.23E-01	16.5
Twist-Roll	0.46	1.77	0.13	4	30	9.76E-02	9.76E-02	6.70E-01	14.6
Twist-Roll	0.46	1.77	0.13	4	40	8.49E-02	8.49E-02	6.29E-01	13.5
Pitch	0.46	1.77	0.13	4	20	2.40E-01	2.40E-01	1.38E+00	17.4
Pitch	0.46	1.77	0.13	4	30	2.11E-01	2.11E-01	1.34E+00	15.7
Pitch	0.46	1.77	0.13	4	40	1.70E-01	1.70E-01	1.21E+00	14.0

Heave	0.46	1.77	0.13	4	20	2.82E-01	2.82E-01	4.26E+00	6.6
Heave	0.46	1.77	0.13	4	30	3.03E-01	3.03E-01	4.38E+00	6.9
Heave	0.46	1.77	0.13	4	40	3.15E-01	3.15E-01	4.37E+00	7.2
Roll	0.46	1.77	0.13	4	20	3.55E-02	3.55E-02	7.76E-01	4.6
Roll	0.46	1.77	0.13	4	30	3.12E-02	3.12E-02	7.49E-01	4.2
Roll	0.46	1.77	0.13	4	40	2.73E-02	2.73E-02	6.81E-01	4.0

Appendix E Pitching moment coefficients

Motion	*AR*	Λ (deg)	$C_{M\text{-}Z}$	$\sigma_0 C_{M\text{-}Z}$
*Pitch-Heave	4	20	1.9e-4	5.2e-1
		30	-3.7e-4	5.6e-1
		40	-5.5e-5	5.6e-1
Twist-Roll	4	20	6.4e-5	9.6e-2
		30	-6.6e-6	1.0e-1
		40	-3.5e-5	1.1e-1
Pitch-Heave	2	20	-1.3e-4	3.8e-1
		30	-2.1e-4	3.4e-1
		40	-1.5e-4	3.2e-1
**Twist-Roll	8	20	-3.1e-4	2.4e-1
		30	3.8e-4	2.7e-1
		40	-9.1e-4	2.7e-1

Note:
AR = Aspect ratio, Λ = sweep angle,
$C_{M\text{-}Z}$ = pitching moment coefficient, and
$\sigma_0 C_{M\text{-}Z}$ = RMS of pitching-moment coefficient.
* is associated with Figure 5.3 (a) & (c), and
** with Figure 5.3 (b) and (d).

FIGURE E.1: Pitching moment coefficients and pitching-moment RMS for swept cases.

Bibliography

Alam, M. M., Zhou, Y., Yang, H. X., Guo, H. & Mi, J. (2009), 'The ultra-low reynolds number airfoil wake', *Experiments in Fluids* **48**(1), 81–103.

Andersen, A., Bohr, T., Schnipper, T. & Walther, J. H. (2016), 'Wake structure and thrust generation of a flapping foil in two-dimensional flow', *Journal of Fluid Mechanics* **812**.

Anderson, J. D. (2017), *Fundamental of Aerodynamics*, McGraw-Hill series in aeronautical and aerospace engineering, 6th edn, McGraw-Hill, New York.

Arastehfar, S., Chew, C. M., Jalalian, A., Gunawan, G. & Yeo, K. S. (2019), 'A relationship between sweep angle of flapping pectoral fins and thrust generation', *Journal of Mechanisms and Robotics-Transactions of the Asme* **11**(1), 1–17.

Astarloa, J. M. D., Mabragana, E. & Hanner, R. (2008), 'Morphological and molecular evidence for a new species of longnose skate (rajiformes: Rajidae: Dipturus) from argentinean waters based on dna barcoding', *Zootaxa* **1921**, 35–46.

Ayancik, F., Zhong, Q., Quinn, D. B., Brandes, A., Bart-Smith, H. & Moored, K. W. (2019), 'Scaling laws for the propulsive performance of three-dimensional pitching propulsors', *Journal of Fluid Mechanics* **871**, 1117–1138.

Bannasch, R., Wilson, R. P. & Culik, B. (1994), 'Hydrodynamic aspects of design and attachment of a back-mounted device in penguins', *Journal of Experimental Biology* **194**(1), 83–96.

Bansmer, S. E. & Radespiel, R. (2012), 'Validation of unsteady reynolds-averaged navier-stokes simulations on three-dimensional flapping wings', *Aiaa Journal* **50**(1), 190–202.

Bao, Y., Kaye, J. & Peskin, C. S. (2016), 'A gaussian-like immersed-boundary kernel with three continuous derivatives and improved translational invariance', *Journal of Computational Physics* **316**(1505.07529v2), 139–144.

Barnes, C. J., Visbal, M. R. & Gordnier, R. E. (2013), 'High-fidelity simulations of a flexible heaving finite-aspect-ratio wing'.

Beem, H. R., Rival, D. E. & Triantafyllou, M. S. (2011), 'On the stabilization of leading-edge vortices with spanwise flow', *Experiments in Fluids* **52**(2), 511–517.

Birch, J. M. & Dickinson, M. H. (2001), 'Spanwise flow and the attachment of the leading-edge vortex on insect wings', *Nature* **412**(6848), 729–33.

Buchholz, J. H. & Smits, A. J. (2008), 'The wake structure and thrust performance of a rigid low-aspect-ratio pitching panel', *J Fluid Mech* **603**, 331–365.

Calderon, D. E., Wang, Z., Gursul, I. & Visbal, M. R. (2013), 'Volumetric measurements and simulations of the vortex structures generated by low aspect ratio plunging wings', *Physics of Fluids* **25**(6), 067102.

Carpenter, K., Sanders, F., Reed, B., Reed, J. & Larson, P. (2010), 'Plesiosaur swimming as interpreted from skeletal analysis and experimental results', *Transactions of the Kansas Academy of Science* **113**(1/2), 1–34.

Carr, Z. R., Chen, C. & Ringuette, M. J. (2013), 'Finite-span rotating wings: three-dimensional vortex formation and variations with aspect ratio', *Experiments in Fluids* **54**(2).

Chopra, M. G. (2006), 'Hydromechanics of lunate-tail swimming propulsion', *Journal of Fluid Mechanics* **64**(2), 375–392.

Chopra, M. G. & Kambe, T. (2006), 'Hydromechanics of lunate-tail swimming propulsion. part 2', *Journal of Fluid Mechanics* **79**(1), 49–69.

Clark, B. D. & Bemis, W. (1979), 'Kinematics of swimming of penguins at the detroit zoo', *Journal of Zoology* **188**(3), 411–428.

Cleaver, D. J., Calderon, D. E., Wang, Z. & Gursul, I. (2016), 'Lift enhancement through flexibility of plunging wings at low reynolds numbers', *Journal of Fluids and Structures* **64**, 27–45.

Cleaver, D. J., Gursul, I., Calderon, D. E. & Wang, Z. (2014), 'Thrust enhancement due to flexible trailing-edge of plunging foils', *Journal of Fluids and Structures* **51**, 401–412.

Cooper, L. N., Sedano, N., Johansson, S., May, B., Brown, J. D., Holliday, C. M., Kot, B. W. & Fish, F. E. (2008), 'Hydrodynamic performance of the minke whale (balaenoptera acutorostrata) flipper', *J Exp Biol* **211**(Pt 12), 1859–67.

Davenport, J., Munks, S. A. & Oxford, P. (1997), 'A comparison of the swimming of marine and freshwater turtles', *Proceedings of the Royal Society of London. Series B. Biological Sciences* **220**(1221), 447–475.

Deng, J. & Caulfield, C. P. (2015), 'Three-dimensional transition after wake deflection behind a flapping foil', *Phys Rev E Stat Nonlin Soft Matter Phys* **91**(4), 043017.

Deng, J., Sun, L. P., Teng, L. B., Pan, D. Y. & Shao, X. M. (2016), 'The correlation between wake transition and propulsive efficiency of a flapping foil: A numerical study', *Physics of Fluids* **28**(9), 094101.

Deng, J., Sun, L. & Shao, X. (2015), 'Dynamical features of the wake behind a pitching foil', *Phys Rev E Stat Nonlin Soft Matter Phys* **92**(6), 063013.

Dong, H., Mittal, R. & Bozkurttas, M. (2005), Wake structure and performance of finite aspect-ratio flapping foils, *in* AIAA, ed., '43rd AIAA Aerospace Science Meeting and Exhibit', Nevada.

Drofelnik, J. & Campobasso, M. S. (2015), 'Three-dimensional turbulent navier-stokes hydrodynamic analysis and performance assessment of oscillating wings for power generation'.

Eldredge, J. D. & Jones, A. R. (2019), 'Leading-edge vortices: Mechanics and modeling', *Annual Review of Fluid Mechanics, Vol 51* **51**(1), 75–104.

Ellington, C. P., vandenBerg, C., Willmott, A. P. & Thomas, A. L. R. (1996), 'Leading-edge vortices in insect flight', *Nature* **384**(6610), 626–630.

Eloy, C. (2012), 'Optimal strouhal number for swimming animals', *Journal of Fluids and Structures* **30**, 205–218.

Fadlun, E. A., Verzicco, R., Orlandi, P. & Mohd-Yusof, J. (2000), 'Combined immersed-boundary finite-difference methods for three-dimensional complex flow simulations', *Journal of Computational Physics* **161**(1), 35–60.

Fish, F. E. & Battle, J. M. (1995), 'Hydrodynamic design of the humpback whale flipper', *J Morphol* **225**(1), 51–60.

Fish, F. E. & J., R. J. (1999), Review of dolphin hydrodynamics and swimming performance, Technical report, SSC San Diego.

Floryan, D., Van Buren, T. & Smits, A. J. (2020), 'Swimmers' wake structures are not reliable indicators of swimming performance', *Bioinspir Biomim* **15**(2), 024001.

Fu, J. J., Hefler, C., Qiu, H. H. & Shyy, W. (2015), 'Effects of aspect ratio on flapping wing aerodynamics in animal flight', *Acta Mechanica Sinica* **30**(6), 776–786.

Garcia, B. F., Weymouth, G. D. & Tutty, O. R. (2017), Analysis of two-dimensional and three-dimensional wakes of long circular cylinders, *in* 'OCEANS 2017', Aberdeen, pp. 1–8.

Garmann, D. J. & Visbal, M. R. (2014), 'Dynamics of revolving wings for various aspect ratios', *Journal of Fluid Mechanics* **748**, 932–956.

Garrick, I. E. (1936), Propulsion of a flapping and oscillating airfoil, Technical report, Langley Memorial Aeronautical Laboratory.

Godoy-Diana, R., Aider, J. L. & Wesfreid, J. E. (2008), 'Transitions in the wake of a flapping foil', *Phys Rev E Stat Nonlin Soft Matter Phys* **77**(1 Pt 2), 016308.

Goza, A. & Colonius, T. (2016), 'A strongly-coupled immersed-boundary formulation for thin deforming surfaces, with application to elastic beams'.

Green, M. A. & Smits, A. J. (2008), 'Effects of three-dimensionality on thrust production by a pitching panel', *J Fluid Mech* **615**, 211–220.

Gurdek Bas, R., Serra, W., Trinchin, R., Leoni, V., Rubio, L., Sampognaro, L., Nagy, G., Cravino, A. & Acuña, A. (2015), 'Confirmation of mola mola (tetraodontiformes: Molidae) and historical records of ocean sunfishes (mola sp.) in the coastal area of uruguay', *Marine Biodiversity Records* **8**, 1–5.

Hackett, J. E. & Cooper, K. R. (2016), 'Extensions to maskell's theory for blockage effects on bluff bodies in a closed wind tunnel', *The Aeronautical Journal* **105**(1050), 409–418.

Harbig, R. R., Sheridan, J. & Thompson, M. C. (2013), 'Reynolds number and aspect ratio effects on the leading-edge vortex for rotating insect wing planforms', *Journal of Fluid Mechanics* **717**, 166–192.

Hartloper, C., Kinzel, M. & Rival, D. E. (2012), 'On the competition between leading-edge and tip-vortex growth for a pitching plate', *Experiments in Fluids* **54**(1).

Hartloper, C. & Rival, D. E. (2013), 'Vortex development on pitching plates with lunate and truncate planforms', *Journal of Fluid Mechanics* **732**, 332–344.

Hong, Y. & Altman, A. (2008), 'Lift from spanwise flow in simple flapping wings', *Journal of Aircraft* **45**(4), 1206–1216.

Hover, F. S., Haugsdal, O. & Triantafyllou, M. S. (2004), 'Effect of angle of attack profiles in flapping foil propulsion', *Journal of Fluids and Structures* **19**(1), 37–47.

Hubel, T. Y., Hristov, N. I., Swartz, S. M. & Breuer, K. S. (2016), 'Wake structure and kinematics in two insectivorous bats', *Philos Trans R Soc Lond B Biol Sci* **371**(1704), 1–12.

Isogai, K., Shinmoto, Y. & Watanabe, Y. (1999), 'Effects of dynamic stall on propulsive efficiency and thrust of flapping airfoil', *Aiaa Journal* **37**(10), 1145–1151.

Jardin, T. (2017), 'Coriolis effect and the attachment of the leading edge vortex', *Journal of Fluid Mechanics* **820**, 312–340.

Karniadakis, G. E. & Triantafyllou, G. S. (2006), 'Three-dimensional dynamics and transition to turbulence in the wake of bluff objects', *Journal of Fluid Mechanics* **238**, 1–30.

Kim, D. & Gharib, M. (2010), 'Experimental study of three-dimensional vortex structures in translating and rotating plates', *Experiments in Fluids* **49**(1), 329–339.

King, J. T., Kumar, R. & Green, M. A. (2018), 'Experimental observations of the three-dimensional wake structures and dynamics generated by a rigid, bioinspired pitching panel', *Physical Review Fluids* **3**(3), 1–20.

Klaassen van Oorschot, B., Mistick, E. A. & Tobalske, B. W. (2016), 'Aerodynamic consequences of wing morphing during emulated take-off and gliding in birds', *J Exp Biol* **219**(Pt 19), 3146–3154.

Koochesfahani, M. M. (1989), 'Vortical patterns in the wake of an oscillating airfoil', *AIAA Journal* **27**(9), 1200–1205.

Lei, C., Cheng, L. & Kavanagh, K. (2001), 'Spanwise length effects on three-dimensional modelling of flow over a circular cylinder', *Computer Methods in Applied Mechanics and Engineering* **190**(22-23), 2909–2923.

Lentink, D. & Dickinson, M. H. (2009), 'Rotational accelerations stabilize leading edge vortices on revolving fly wings', *J Exp Biol* **212**(Pt 16), 2705–19.

Liu, P. & Bose, N. (1993), 'Propulsive performance of three naturally occurring oscillating propeller planforms', *Ocean Engineering* **20**(1), 57–75.

Liu, T. S., Wang, S. Z., Zhang, X. & He, G. W. (2015), 'Unsteady thin-airfoil theory revisited: Application of a simple lift formula', *Aiaa Journal* **53**(6), 1492–1502.

Lu, Y. & Shen, G. X. (2008), 'Three-dimensional flow structures and evolution of the leading-edge vortices on a flapping wing', *J Exp Biol* **211**(Pt 8), 1221–30.

Lu, Y., Shen, G. X. & Lai, G. J. (2006), 'Dual leading-edge vortices on flapping wings', *J Exp Biol* **209**(Pt 24), 5005–16.

Maertens, A. P. & Weymouth, G. D. (2015), 'Accurate cartesian-grid simulations of near-body flows at intermediate reynolds numbers', *Computer Methods in Applied Mechanics and Engineering* **283**, 106 – 129.

Magnuson, J. J. (1978), Locomotion by scombrid fishes: Hydromechanics, morphology, and behavior, *in* W. H. Randall & D.J., eds, 'Locomotion', Vol. 7, Academic Press, pp. 239–313.

Maskell, E. C. (1965), A theory of the blockage effects on bluff bodies and stalled wings in a closed wind tunnel, Technical report, Ministry of Aviation Aeronautical Research Council.

Maxworthy, T. (2007), 'The formation and maintenance of a leading-edge vortex during the forward motion of an animal wing', *Journal of Fluid Mechanics* **587**, 471–475.

Mittal, R. & Balachandar, S. (1995), 'Effect of three-dimensionality on the lift and drag of nominally two-dimensional cylinders', *Physics of Fluids* **7**(8), 1841–1865.

Moored, K. W. & Quinn, D. B. (2019), 'Inviscid scaling laws of a self-propelled pitching airfoil', *AIAA Journal* **57**(9), 3686–3700.

Moriche, M., Flores, O. & Garcia-Villalba, M. (2016), 'Three-dimensional instabilities in the wake of a flapping wing at low reynolds number', *International Journal of Heat and Fluid Flow* **62**, 44–55.

Muscutt, L. E., Weymouth, G. D. & Ganapathisubramani, B. (2017), 'Performance augmentation mechanism of in-line tandem flapping foils', *Journal of Fluid Mechanics* **827**, 484–505.

Onoue, K. & Breuer, K. S. (2017), 'A scaling for vortex formation on swept and unswept pitching wings', *Journal of Fluid Mechanics* **832**, 697–720.

Pennycuick, C. J. (1968), 'A wind-tunnel study of gliding flight in the pigeon columba livia', *J Exp Biol* **49**(3), 509–526.

Peskin, C. S. (2003), 'The immersed boundary method', *Acta Numerica* **11**, 479–517.

Rambahiniarison, J. M., Araujo, G., Lamoste, M. J., Labaja, J., Snow, S. & Ponzo, A. (2016), 'First records of the reef manta ray manta alfredi in the bohol sea, philippines, and its implication for conservation', *Journal of Asia-Pacific Biodiversity* **9**(4), 489–493.

Ringuette, M. J., Milano, M. & Gharib, M. (2007), 'Role of the tip vortex in the force generation of low-aspect-ratio normal flat plates', *Journal of Fluid Mechanics* **581**, 453–468.

Rivera, A. R., Rivera, G. & Blob, R. W. (2013), 'Forelimb kinematics during swimming in the pig-nosed turtle, carettochelys insculpta, compared with other turtle taxa: rowing versus flapping, convergence versus intermediacy', *J Exp Biol* **216**(Pt 4), 668–80.

Rohr, J. J. & Fish, F. E. (2004), 'Strouhal numbers and optimization of swimming by odontocete cetaceans', *J Exp Biol* **207**(Pt 10), 1633–42.

Russo, R. S., Blemker, S. S., Fish, F. E. & Bart-Smith, H. (2015), 'Biomechanical model of batoid (skates and rays) pectoral fins predicts the influence of skeletal structure on fin kinematics: implications for bio-inspired design', *Bioinspir Biomim* **10**(4), 046002.

Sato, K., Shiomi, K., Watanabe, Y., Watanuki, Y., Takahashi, A. & Ponganis, P. J. (2010), 'Scaling of swim speed and stroke frequency in geometrically similar penguins: they swim optimally to minimize cost of transport', *Proc Biol Sci* **277**(1682), 707–14.

Schlichting, H. & Kestin, J. (1979), *Boundary-layer theory*, 7th ed. edn, McGraw-Hill, New York ; London.

Schnipper, T., Andersen, A. & Bohr, T. (2009), 'Vortex wakes of a flapping foil', *Journal of Fluid Mechanics* **633**, 411–423.

Senturk, U. & Smits, A. J. (2019), 'Reynolds number scaling of the propulsive performance of a pitching airfoil', *Aiaa Journal* **57**(7), 2663–2669.

Shortal, J. A. & Maggin, B. (1946), Effect of sweptback and aspect ratio on longitudinal stability characteristics of wings at low speeds, Technical report, National Advisory Committee for Aeronautics.

Smits, A. J. (2019), 'Undulatory and oscillatory swimming', *Journal of Fluid Mechanics* **874**, 1–70.

Taira, K. & Colonius, T. (2009), 'Three-dimensional flows around low-aspect-ratio flat-plate wings at low reynolds numbers', *Journal of Fluid Mechanics* **623**, 187–207.

Theodorsen, T. (1935), General theory of aerodynamic instability and the mechanism of flutter, Technical report, NASA.

Thomas, A. L. & Taylor, G. K. (2001), 'Animal flight dynamics i. stability in gliding flight', *J Theor Biol* **212**(3), 399–424.

Triantafyllou, G. S., Triantafyllou, M. S. & Grosenbaugh, M. A. (1993), 'Optimal thrust development in oscillating foils with application to fish propulsion', *Journal of Fluids and Structures* **7**(2), 205–224.

Triantafyllou, M. S., Techet, A. H. & Hover, F. S. (2004), 'Review of experimental work in biomimetic foils', *Ieee Journal of Oceanic Engineering* **29**(3), 585–594.

Triantafyllou, M. S., Triantafyllou, G. S. & Gopalkrishnan, R. (1991), 'Wake mechanics for thrust generation in oscillating foils', *Physics of Fluids a-Fluid Dynamics* **3**(12), 2835–2837.

Uddin, E., Naseem, M. A., Khalid, S. U., Mubashar, A. & Shah, S. R. (2017), 'Investigation of the flow around uncambered airfoils at 1000 reynolds number using computational fluid dynamics for micro air vehicles'.

Uhlmann, M. (2005), 'An immersed boundary method with direct forcing for the simulation of particulate flows', *Journal of Computational Physics* **209**(2), 448–476.

Van Buren, T., Floryan, D., Brunner, D., Senturk, U. & Smits, A. J. (2017), 'Impact of trailing edge shape on the wake and propulsive performance of pitching panels', *Physical Review Fluids* **2**(1).

Van Buren, T., Floryan, D. & Smits, A. J. (2018), 'Bio-inspired underwater propulsors'.

Van Buren, T., Floryan, D. & Smits, A. J. (2019), 'Scaling and performance of simultaneously heaving and pitching foils', *AIAA Journal* **57**(9), 3666–3677.

van Dam, C. P. (1987), 'Efficiency characteristics of crescent-shaped wings and caudal fins', *Nature* **325**(6103), 435–437.

Von Busse, R., Hedenstrom, A., Winter, Y. & Johansson, L. C. (2012), 'Kinematics and wing shape across flight speed in the bat, leptonycteris yerbabuenae', *Biol Open* **1**(12), 1226–38.

Wang, S., Zhou, Y., Alam, M. M. & Yang, H. (2014), 'Turbulent intensity and reynolds number effects on an airfoil at low reynolds numbers', *Physics of Fluids* **26**(11), 115107.

Weymouth, G. D. & Yue, D. K. P. (2011), 'Boundary data immersion method for cartesian-grid simulations of fluid-body interaction problems', *Journal of Computational Physics* **230**(16), 6233–6247.

Williamson, C. H. K. (1996), 'Vortex dynamics in the cylinder wake', *Annual Review of Fluid Mechanics* **28**, 477–539.

Williamson, C. H. K. (2006), 'Three-dimensional wake transition', *Journal of Fluid Mechanics* **328**(-1), 345–407.

Williamson, C. H. K. & Roshko, A. (1988), 'Vortex formation in the wake of an oscillating cylinder', *Journal of Fluids and Structures* **2**(4), 355–381.

Willmott, A. P. & Ellington, C. P. (1997), 'The mechanics of flight in the hawkmoth manduca sexta. ii. aerodynamic consequences of kinematic and morphological variation', *J Exp Biol* **200**(Pt 21), 2723–45.

Wong, J. G., Kriegseis, J. & Rival, D. E. (2013), 'An investigation into vortex growth and stabilization for two-dimensional plunging and flapping plates with varying sweep', *Journal of Fluids and Structures* **43**, 231–243.

Wong, J. G., laBastide, B. P. & Rival, D. E. (2017), 'Flow separation on flapping and rotating profiles with spanwise gradients', *Bioinspir Biomim* **12**(2), 026008.

Wong, J. G. & Rival, D. E. (2015), 'Determining the relative stability of leading-edge vortices on nominally two-dimensional flapping profiles', *Journal of Fluid Mechanics* **766**, 611–625.

Wu, T. Y. (2011), 'Fish swimming and bird/insect flight', *Annual Review of Fluid Mechanics, Vol 43* **43**(1), 25–58.

Yilmaz, T. O. & Rockwell, D. (2011), 'Flow structure on finite-span wings due to pitch-up motion', *Journal of Fluid Mechanics* **691**, 518–545.

Zhang, J. (2017), 'Footprints of a flapping wing', *Journal of Fluid Mechanics* **818**, 1–4.

Zhou, Y., Alam, M. M., Yang, H. X., Guo, H. & Wood, D. H. (2011), 'Fluid forces on a very low reynolds number airfoil and their prediction', *International Journal of Heat and Fluid Flow* **32**(1), 329–339.

Zhu, J., White, C., Wainwright, D. K., Di Santo, V., Lauder, G. V. & Bart-Smith, H. (2019), 'Tuna robotics: A high-frequency experimental platform exploring the performance space of swimming fishes', *Science Robotics* **4**(34), 1–12.

Zurman-Nasution, A. N., Ganapathisubramani, B. & Weymouth, G. D. (2020), 'Influence of three-dimensionality on propulsive flapping', *Journal of Fluid Mechanics* **886**, 1–14.